Università degli studi di Roma Tor Vergata

DOTTORATO DI RICERCA IN FISICA - XXVII CICLO

On the quantum contributions to phase transitions in Water probed by inelastic neutron scattering

Giovanni Romanelli

Tutores: Prof. C. Andreani and Prof. R. Senesi

Coordinatore: Prof. M. De Crescenzi

Anno Accademico 2013/2014

"Omnia in Philosophia,
omnes in philosopho continentur."
Pierre Gringoire

Abstract

This Thesis on the Physics of condensed matter collects some of my research activities performed during my Doctorate devoted to the measurement of nuclear quantum effects on the dynamics of hydrogen and oxygen in the water molecule. Indeed, the single-particle motion and in particular the kinetic energy are effective thermometers representing the probe to measure the deviations from classical or first-order quantum mechanics.

In the introduction, I present the scientific case and highlight the complexity of the mechanical and thermodynamic properties of water and their physical modelling. I also explain why neutron scattering has been chosen as the experimental technique to study this subject and how inelastic scattering at high energy and momentum transfers can access the single-particle motion in the case of the nuclear constituents of the molecule *i.e.*, oxygen and hydrogen, the latter as a proton or deuteron.

Then, a discussion on momentum distributions in statistical classical and quantum systems is presented, introducing models enabling a physical interpretation in the case of water or similar molecules. In particular, the use of multivariate distributions allows the measurement of the anisotropy of the effective potential which determines the nuclear motion. In particular, i) I optimized the data reduction and analysis routines reducing their running times and ii) I increased the reliability of the fitting parameters describing the shapes of the momentum distributions, reducing the number of free parameters through physical constraints. This leads to the determination of the components of the nuclear kinetic energy matrix.

A harmonic model is then proposed to relate these observables to the translational, rotational and vibrational frequencies of the molecule. This calculation is based on the model proposed by Moreh and co-workers for the interpretation of gamma nuclear resonance scattering from excited nuclear levels. I derived the analytical generalization to a molecule in any phase through knowledge of vibrational frequencies and molecular geometrical parameters. Moreover, I implemented the model in the data analysis routines in order to predict, guide or compare

with experimental results.

The results of inelastic neutron scattering experiments on the melting of light and heavy water are then presented. Changes in the components of the kinetic-energy matrix are discussed in the case of phase transitions and the relevance of nuclear quantum effects is highlighted. The experimental results are compared to the harmonic model and to computer simulations based on path-integral molecular dynamics. Another set of experiments is presented on the measurement of the dynamic structure factor of supercritical water in thermodynamic states across the pseudo-critical line, *i.e.*, the locus of points with a pressure greater than the critical pressure corresponding to a maximum of the specific heat for a temperature greater than the critical temperature. Moreover, the changes in the dynamic structure factor are studied in the amorphous-solid water phase across the transition from very-high-density to high-density amorphous ice, and then from the high-density to the low-density amorphous ice. I have been directly involved in the experiment preparation and set-up, measurements, analysis and interpretation of the experiments on heavy water, supercritical water and amorphous ice. I contributed to the data analysis and interpretation of inelastic neutron scattering experiments in super-cooled, stable liquid, supercritical water and poly-crystalline ice.

This work has been carried out at the ISIS Neutron and Muon Pulsed Source at the Rutherford Appleton Laboratory in the UK for about four months for the experiments and data analysis, at the SNS Spallation Neutron Source at Oak Ridge National Laboratory in the US for data reduction and analysis, and in Tor Vergata for the data analysis, interpretation and modelling.

During the three years of Doctorate I attended to the School of Neutron Scattering Francesco Paolo Ricci (XI Edition) on the neutron investigation of bio-systems in Taormina as a student; I participated in the International Neutron Scattering Instrumentation School at the Laboratori Nazionali di Frascati as a student and local organizer; I attended the International Conference on Neutron Scattering 2013 in Edinburgh contributing to the poster session with the results on the oxygen dynamics that was for the first time measured through neutron Compton scattering; I contributed to the VI Workshop in Electron-Volt Neutron Spectroscopy meeting in Abingdon (UK) with a talk on competing quantum effects on the melting of heavy water.

Since September 1^{st}, I steadily work at ISIS in Rutherford Appleton Laboratory to the computational and experimental development of eV neutron scattering techniques.

Contents

Chapter 1

Introduction

1.1 A long discussion

About 24 centuries ago, Plato identified water, one of the four Empedocles's classical elements, with the perfect solid that more resembles a slippery ball, the icosahedron. In modern science, the chemical composition of water molecule (H_2O) was defined at the beginning of XVII century as two hydrogen (H) and one oxygen (O) atoms, and some famous scientists such as Gay-Lussac, Lewis, Kelvin and Celsius spent their energies in the study of the compound that covers our planet as much as composes our body. We are probably so used to it that for us it is colourless, odourless and tasteless and is at the base of our daily comparisons and measure scales. Water is one of the simpler, lighter and safer molecules even if it is composed of the two most common reactive elements. Considering a molecular diameter of $a = 2.75$ Å, few other molecules can be found that are smaller.

The reason why in 2014 a Ph.D thesis has water as the main subject is 72-fold [1]. This is indeed the number of features regarding this molecule that we cannot explain and the measure of our ignorance of its deep and shadowy nature.

1.1.1 Intermolecular forces

Water structure is considered permanent and steady. The auto-dissociation mechanism converting $2H_2O \rightleftharpoons H_3O^+ + OH^-$ takes place for a very short time (ps) with respect to the mean time that the exchanged proton spends in the water molecule (ms). The finite size of the molecule and the corresponding spatial charge distribution are reflected into an inter-molecular potential [2] that is repulsive when the two molecules are approached and that is attractive when they are separated, given a vanishing interaction condition in the limit of increasing distance.

Water dipole moments are responsible for the attraction potential. The dipole moment for a water monomer has a value of 1.84 D, one of the highest values amongst molecules [3], and changes to values between 2.4 D and 2.6 D in the water condensed phases [4]. The resulting potential has been discussed by Lennard-Jones [5] and consists of a repulsive term depending on R^{-12} and an attractive one depending on R^{-6}, where R is here the inter-molecular distance.

Moreover, when a proton (H nucleus) lies between the O of its molecule and an O belonging to a nigh molecule, both with partial negative charges, a bond is created between the two O that is generally linear and maximized when the two opposite HO interactions are equal. When a H participates in such a bond it is said to form a Hydrogen Bond (HB) [6–9].

The HB occurs in its stronger form when a proton is shared between two negatively-charged fluorines and its strength decreases when fluorine is replaced by O or nitrogen. The extraordinary importance of HB effects on water can be easily appreciated considering the very high boiling point of liquid water (373 K) with respect to other similar molecules where HB does not happen, such has H_2S (211 K), H_2Se (231 K) or H_2Te (269 K).

The strength of HB in Water is far greater than the other inter-molecular interactions and leads to a 15% closer arrangement of the molecules than the case with a Lennard-Jones potential only [10]. Formation of HB between water molecules provokes a decrease of both enthalpy and entropy of the system, and can be seen as the cause for ordered structures found in condensed phases that are lost in the transition to water vapour.

As a consequence of the HB interaction, the structure of water is generally thought as a tetrahedron, with an O atom at the centre and 2 bonding electrons and two lone electrons in sp3 hybridized orbitals with angular separation between the OH directions of about 109 degrees. This structure is actually found in condensed phases such as hexagonal ice Ih, and is otherwise approximately similar.

1.1.2 Nuclear Quantum Effects

The H and O atoms do not keep still in the previously pictured tetrahedral positions. Being each position defined by a minimum in the inter-atomic potentials, quantum particles like atoms cannot stay still but possess a minimum amount of energy related to the depth of this potential and then to the importance of their localization. All the effects acting on a nucleus and resulting in a deviation from a Maxwell - Boltzmann statistics are defined as Nuclear Quantum Effects (NQEs) [11–17]. The resulting energy is called Zero Point Energy (ZPE) [18–20] since it is observed even when the temperature of the system is brought to absolute zero and all the

thermal energy has been removed from the system. Considering the atoms within a molecule, this phenomenon brings to the definition, based on the symmetry of the molecule, of several motions that the H must undergo and that are called stretch and bend modes [21,22]. The former are related to motions of the H in the direction of the covalent bond, increasing and decreasing the OH distance as by a stretching, the latter bends the molecule changing the angle between the two covalent bonds. These motions can be thought as (and often approximated by) harmonic vibrations. If enough energy is given to the molecule, it is possible that a vibration is promoted from the ground level to a higher level, where the discrete level sequence can be obtained resolving the Schroedinger equation describing the system. The presence of inter-molecular forces brings to a similar quantization of levels and energies that hinder the free rotations of the molecules. Changes in the molecular orientation can then be related to vibrations around an average positions, called librations, or through discrete jumps from a position to another, with the HB connecting two different external O before and after the jump. Since the Schroedinger equation depends upon the mass of the atom, differences in level energies are found under isotope substitution, that is after a replacement of a H by a Deuterium (D). Isotope effects are of great importance in order to define the action of NQEs on the water molecule. As an example, the classical (non quantum) value for the HB average distance is increased by ZPE in different ways if H_2O or heavy Water (D_2O) molecules are considered.

The importance on NQEs increases in the limit of low temperature, and so the effect of isotopic substitution. Accordingly, the difference between boiling temperatures of H_2O and D_2O is of only 1 degree (T = 373 K), the difference between melting points is about 4 degrees (T = 273 K), while the difference between the glass transition temperatures can reach 10 degrees (T = 136 K), depending on the preparation of the sample [23, 24]. The picture is anyway more complicated, as the difference of 7 degrees between the the maximum density temperatures suggests. An example of the isotope substitution effect on the HB is the Ubbelonde effect, describing the change in the OO distance [8].

1.1.3 The phase diagram of water

The preferred physical states of bulk water at different temperatures and pressures are reported in the phase diagram in Figure 1.1. Within each phase, the material is uniform with respect to its chemical composition and physical state. Typically, water on Earth is a liquid, but it becomes ice if its temperature is lowered below 273 K or transformed in vapour if its temperature is raised above 373 K, at atmospheric pressure. A line in a phase diagram represents the pairs of values

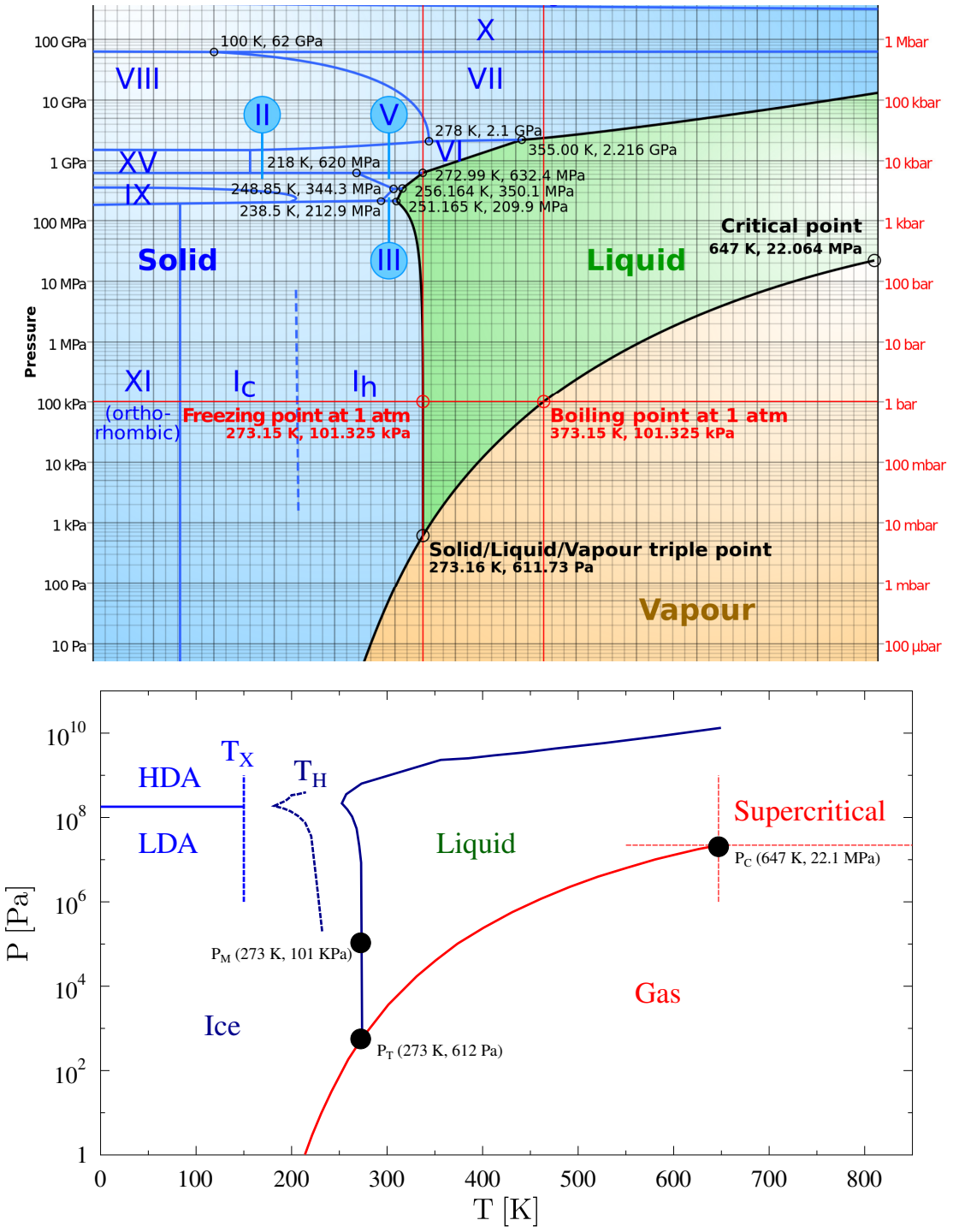

Figure 1.1: The phase diagram of water. The top panel from [10] reproduces the solid, liquid and vapour stable phases of water, while the bottom panel highlights the regions studied in this work.

of temperature and pressure when two phases can stably coexist in any relative proportions (having the same Gibbs free energy). Here, a slight change in temperature or pressure may cause the phases to abruptly change from one physical state to the other. Where three phase lines join, there is a triple point, when three phases stably coexist. Under the singular conditions of temperature and pressure where liquid water, gaseous water and hexagonal ice stably coexist, there is a triple point where both the boiling point of water and melting point of ice are equal. This happens when $T_T = 272.16$ K and $P_T = 612$ Pa. Four phase lines cannot meet at a single point. A critical point occurs at the end of a phase line where the properties of the two phases become indistinguishable from each other, for example when, under singular conditions of temperature and pressure, liquid water is hot enough and gaseous water is under sufficient pressure that their densities are identical.

One can appreciate the complexity in the phase diagram of water considering the number of triple points occurring in it. There is one critical point defined as $T_C = 647$ K and $P_C = 22.064$ MPa, where the line dividing the vapour and liquid phases ends. For temperatures and pressures larger than T_C, P_C, it is not possible to recognize the phase as either liquid or gaseous, and it is then defined as Supercritical water (SCW).

When a pure water sample, with resistivity larger than 25 MΩ, is cooled in the region of the melting point, it can happen that no phase transition from liquid to solid occurs, and that the sample enters a metastable phase where it is still liquid even if its temperature is below 273 K and its thermodynamic coordinates in the phase diagram would suggest it to be in the solid phase. This condition is defined as supercooling [25–27] and occurs when the number of nucleation centres in the sample, that is the impurities within, is particularly low. The Gibbs energy for this state must have a local minimum or can be thought as an unstable equilibrium state. Indeed, a small perturbation can brake this fragile equilibrium and bring to the transition to ice with release of heat. There is no experimental way to super-cool bulk water under 232 K [28] unless in micrometre-sized droplets that have been evaporatively cooled as in Ref [29], where T = 227 K was reached.

The known ices can be roughly divided by cluster analysis of their structures into crystalline and amorphous ices, the former presenting an ordered HB network, the others with features similar to glasses and with no crystalline structure. The density of these latter can largely change when moving in the phase diagram.

In the next Chapters 4, 5 and 6 we will discuss the change in dynamical molecular observables in the passage from liquid to solid for H_2O and D_2O, as well as the passage from liquid to

supercritical region and from high to low density amorphous ice.

1.2 The Neutron as a probe

The strange behaviour in passing through thick materials puzzled scientists like Rutherford, forcing them to imagine strange explanations for what was not an α, a β or a γ radiation. In 1932 Chadwick understood the puzzle and opened the way for the basic properties of the neutron as we all know: a mass of 1.008 a.m.u., the same as the proton within 1%, as the standard model can easily predict; no electric charge, explaining why they can penetrate thick metal samples; half-integer spin, as can be evinced by the laws governing neutron stars dynamics. What emerged by a more complete study of this particle is its anomalous nuclear magnetic momentum, that should be zero due to its vanishing charge and instead is 1.91 in the Bohr magnetic moment units, being this a fortune for those that can study the magnetic properties of superconductors thanks to neutron spin-echo technique.

The existence of this work of thesis has its origin a long time ago, in a difficult moment for Humanity. The Nobel prize in 1938 to Enrico Fermi came to underline its contribution to the understanding of slow neutron interactions with matter, and the resulting production of nuclear fission. Its fruitful work gave us nuclear fission facilities, that have been in the past the main neutron sources for neutron science as well as energy for everyday life.

Fission reactor facilities are able to offer a continuous flux of neutrons thanks to the fission reactions $^{235}\mathrm{U} + \mathrm{n} \rightarrow \mathrm{X} + \mathrm{Y} + 2.5\ \mathrm{n}$, where 2.5 is the average number of neutrons generated in the reaction, each of which has about 2 MeV of energy. These neutrons are then treated with moderators around the core and let escape through neutron guides in order to be used on corresponding beam lines.

Aside nuclear facilities, spallation neutron sources appeared during the '70s of the last century. These sources are based on acceleration of electrons or protons hitting a target composed of some heavy element generating a large number neutrons. In the case of proton acceleration, the charged particle energy can reach hundreds of MeV and generate neutrons up to the same high energy. The fluxes from these latter facilities differ for two reasons from those accessible in reactor neutron sources: firstly, the energy of the neutron can easily reach hundreds of eV; secondly, the flux is not continuous but pulsed, enabling time of flight techniques for the measure of neutron energies.

Obviously, both kind of sources are of great importance in the frame of condensed matter

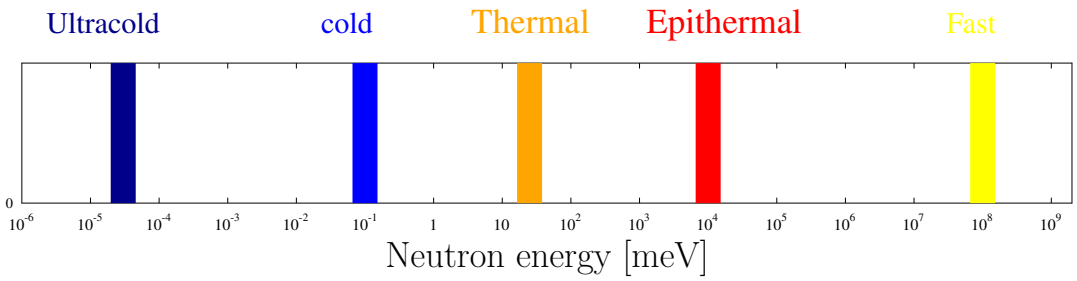

Figure 1.2: Usual definition of neutron "temperature" according to its energy. Thermal and Epithermal regions are those most investigated in this work.

studies, for a community that increases year after year, both with pros and cons. However, due to the subject of this work, all the proposed experiments have been performed at pulsed sources. As explained in Chapter 2, the reason is that we are interested in quantities based on single-particle scattering and in regimes of neutron energy transfer comparable or greatly larger than the water molecule binding energies, that means energies between tens of meV up to hundreds of eV, that only pulsed spallation sources can access.

Depending on the energy of the neutron used as a probe, common use defines a name based on the temperature that condensed matter would have being in thermal equilibrium with that neutron. This procedure is based on the simple equivalence between energy and temperature through the Boltzmann constant k_B, that is

$$E = k_B T. \tag{1.1}$$

Neutrons whose energy corresponds to ambient temperature, that is around 25 meV (for a temperature of 300 K) are called *thermal neutrons*. Even if there is no convention establishing the exact boundaries for thermal region, we can imagine it going from some meV up to 500 meV. Neutrons with these energies are well suited to study property of condensed matter such as molecular vibrations and rotations. After the higher limit, up to some keV, we speak of *epithermal neutrons*, source of knowledge of the nuclear momentum distributions through the technique of neutron Compton scattering [30]. At energies lower than the meV, *cold* and *ultra cold neutrons* can be used to study diffusion processes or explore the structure of molecules through crystallography. Aforementioned neutrons are referred to as slow, against the *fast neutrons*, with energies up to tens of MeV and whose importance is mainly related to industry and cultural heritage matters such as the study of the response of electronic devices irradiated with cosmic rays.

Chapter 2

Inelastic Neutron Scattering

Thermal and epithernal neutron scattering is the framework where the experimental results presented in this work have been obtained. For this reason, and for a definition of notation and constants, a brief revision of the theory describing neutron interactions with condensed matter will be reported in the present chapter.

The basic behaviour of a neutron entering a condensed-matter medium can be described considering the incident wave function as a plane wave defined by the wave number k, and the scattered wave function as the first term of an expansion in spherical harmonics, that is a spherical wave in the reference frame of the centre of mass,

$$\psi(\mathbf{x}) = e^{ikz} \qquad \psi'(\mathbf{x}) = -\frac{b}{r}e^{ikr} \tag{2.1}$$

with b a constant taking into account the intensity of the scattered wave, and hence related to the cross section of the interaction, dependent on the scattering nuclide and known as the *scattering length*, with a positive value corresponding to a repulsive potential (in most cases). The scattering is elastic, that is we consider the same modulus k in both the definition of ψ and ψ', if the position of the nucleus is fixed and if the energy of the neutron is too small to excite the internal structure of the nucleus. The first of these two conditions will be soon relaxed, since we are mostly interested in atomic motion, considering it equivalent to the motion of the nucleus, while the second condition will be maintained for all the treatment. Anyway, any information about resonances or adsorption probability of the neutron by the scattering centre is embedded in the imaginary part of the scattering length, that is in general a complex number. If the absorption is near a resonance, the imaginary part largely changes with the neutron energy,

otherwise b can be thought as non depending at all on the energy at all. With these hypothesis, from the experimental definition of the differential cross section, we can obtain the result

$$\frac{d\sigma}{d\Omega} = \frac{\text{Number of neutron throught detector area per second}}{\text{Incident flux } \times \text{ detector angular acceptance}} = \frac{v\,|\psi'|^2\,dS}{v\,|\psi|^2 d\Omega} = |b|^2 \tag{2.2}$$

and hence, integrating over the angular dependence, the total scattering cross section is

$$\sigma_{\text{tot}} = 4\pi|b|^2. \tag{2.3}$$

2.1 Theory of Thermal Neutron Scattering

We relax now the conditions on the elasticity of the scattering and the restiction to the neutron wave functions. The scattering of a neutron of incident wave vector $\mathbf{k}$ and final wave vector $\mathbf{k}'$ on a single nucleus passing from the state λ to the state λ' can be generally expressed in terms of the double differential cross section

$$\left(\frac{d^2\sigma}{d\Omega dE'}\right)_{\lambda\to\lambda'} = \frac{d^2\sigma}{d\Omega dk'}\frac{dk'}{dE'} = \frac{m}{\hbar^2 k'}\frac{d^2\sigma}{d\Omega dk'} = \frac{m}{\hbar^2 k'}\frac{W_{\mathbf{k}\lambda\to\mathbf{k}'\lambda'}}{\Phi} = \frac{m^2}{\hbar^3 k k'}W_{\mathbf{k}\lambda\to\mathbf{k}'\lambda'} \tag{2.4}$$

where the transition rate from the initial to the final state, W, has been introduced, E and E' are the neutron energies before and after the scattering and m is the neutron mass. Finally, $d\Omega$ and dE' are the detector angular and energy acceptances. The Fermi Golden Rule relates this transition rate to: a) the density of states ρ, b) the matrix of states of the potential V of the interaction neutron-nucleus and c) the energy conservation, with the positively defined energy lost by the neutron, $E - E' = \hbar\omega$, adsorbed by the scattering centre, according to the equation

$$W_{\mathbf{k},\lambda\to\mathbf{k}',\lambda'} = \frac{2\pi}{\hbar}\rho_{\mathbf{k}'\lambda'}|\langle\mathbf{k}',\lambda'|V|\mathbf{k},\lambda\rangle|^2\delta\left(\hbar\omega + E_\lambda - E_{\lambda'}\right) \tag{2.5}$$

In an experiment, the prepared incident neutron and the detected neutron are far away from the scattering centres, and then their wave functions can be defined as plane waves. In this case the matrix element $\langle\mathbf{k}',\lambda'|V|\mathbf{k},\lambda\rangle$ can be expressed as

$$\langle f|V|i\rangle = \langle\mathbf{k}'\lambda'|V|\mathbf{k}\lambda\rangle = \int d\mathbf{r}\,d\mathbf{R}\,e^{-i\mathbf{k}'\cdot\mathbf{r}}\phi_{\lambda'}(\mathbf{R})Ve^{i\mathbf{k}\cdot\mathbf{r}}\phi_\lambda(\mathbf{R}) \tag{2.6}$$

As discussed in the Introduction, the fact that neutrons are extremely penetrating particles is due to their vanishing charge, excluding any interaction with paired-electron clouds and distant nuclei through the long distance electric potential. They only scatter when they hit the small nucleus at the centre of the atom, occupying a part of section over about 10^{30}. This was clear to Enrico Fermi, that introduced a simple form for V, called the Fermi pseudo potential, based on the idea of a point like scattering centre:

$$V = V(\mathbf{r} - \mathbf{R}) = a\delta(\mathbf{r} - \mathbf{R}) = \frac{2\pi\hbar^2}{m} b\delta(\mathbf{r} - \mathbf{R}) \tag{2.7}$$

where b is the already mentioned scattering length[1] and the square of his magnitude, already introduced in Eq. 2.3, is of the order of 1 barn = 10^{-28} m^2. The merit of the Fermi pseudo potential far exceeds the admirable simple physical interpretation in its form, making the integration processes also very simple. The integration over the position of the neutron will disappear, since the scattering requires an overlap of the probing particle and of the scattering centre. Eq 2.6 can evolve in the simpler

$$\langle f|V|i\rangle = \int d\mathbf{r}\, d\mathbf{R}\, e^{-i\mathbf{q}\cdot\mathbf{r}} \phi_{\lambda'}(\mathbf{R}) a\delta(\mathbf{r} - \mathbf{R})\phi_\lambda(\mathbf{R}) = a\langle\lambda'|e^{-i\mathbf{q}\cdot\mathbf{R}}|\lambda\rangle \tag{2.8}$$

with $\mathbf{q} = \mathbf{k} - \mathbf{k}'$ being the momentum transferred from the neutron to the system.

The second quantity that we need in order to calculate the double differential cross section is $\rho_{\mathbf{k}',\lambda}$. Applying the same condition of plane wave for the scattered neutron, no quantization of energy or momenta affects its density of states. If then the reader excuses the liberty we take in using a unitary spatial volume, not affecting the following results, the density of final states that the neutrons can reach after the scattering is

$$\rho_{\mathbf{k}'} d\mathbf{k}' = \frac{1}{(2\pi)^3} k'^2 dk\, d\Omega \tag{2.9}$$

Grouping these quantities, thanks to a wonderful (but not casual) cancellation of constants, we can express the double differential cross section in the form

$$\left(\frac{d^2\sigma}{d\Omega dE'}\right)_{\mathbf{k}\lambda\to\mathbf{k}'\lambda'} = \frac{k'}{k} \left|b\langle\lambda'|e^{-i\mathbf{q}\cdot\mathbf{R}}|\lambda\rangle\right|^2 \delta\left(\hbar\omega + E_\lambda - E_{\lambda'}\right) \tag{2.10}$$

Since this moment, the sample has been thought as composed of a single nucleus. No coherent or incoherent scattering can occour, the two being possible when a sum over a great

[1] In particular, this is the *bound* scattering length, since it is relative to a nucleus fixed in space. Since an actual nucleus is in general *free*, the scattering length should be replaced with $b_f = \frac{M}{m+M} b$

number of atoms is introduced and interference can act between the resulting scattered waves. Also, when more than an atom is considered, it is not possible to univocally define the states $|\lambda\rangle$ and $|\lambda'\rangle$. The initial state of the nucleus, λ, must be replaced with an average over a thermal ensemble possibilities, accordingly with weights n_λ, and a sum over all the final accessible states needs to be performed. In practice,

$$\left|b\langle\lambda'|e^{-i\mathbf{q}\cdot\mathbf{R}}|\lambda\rangle\right|^2 \to \sum_{\lambda'}\sum_{\lambda} n_\lambda \sum_{j,j'} b^*_{j'} b_j \langle\lambda|e^{-i\mathbf{q}\cdot\mathbf{R}_{j'}}|\lambda'\rangle\langle\lambda'|e^{+i\mathbf{q}\cdot\mathbf{R}_j(t)}|\lambda\rangle \tag{2.11}$$

The sums over initial and final states involves the delta function for the energy conservation. It is useful to write this function in its integral form,

$$\delta\left(\hbar\omega + E_\lambda - E_{\lambda'}\right) = \int_{-\infty}^{\infty} dt e^{i(\hbar\omega - E_\lambda + E_{\lambda'})t/\hbar} \tag{2.12}$$

Also, combining the definition for the energy of the nuclear states, $H|\lambda\rangle = E_\lambda|\lambda\rangle$, with H the Hamiltonian of the system, and introducing the time dependent Heisenberg operator for the nuclear position $R_j(t) = e^{iHt/\hbar}R_j e^{-iHt/\hbar}$, and finally using the unitary condition for the energy eigenvector base $\sum_{\lambda'}|\lambda'\rangle\langle\lambda'| = 1$, it is possible to simplify the actual result in

$$\frac{d^2\sigma}{d\Omega dE'} = \frac{k'}{k}\sum_{\lambda} n_\lambda \sum_{j,j'} b^*_{j'} b_j \int_{-\infty}^{\infty} \langle\lambda|e^{-i\mathbf{q}\cdot\mathbf{R}_{j'}} e^{i\mathbf{q}\cdot\mathbf{R}_j(t)}|\lambda\rangle \frac{e^{-i\omega t}}{2\pi\hbar} dt \tag{2.13}$$

and recognizing $(2\pi\hbar)^{-1}\int \ldots \exp\left(-i\omega t\right)$ as the Fourier transform $\mathcal{F}_t \ldots$ of $\ldots$, we can write

$$\frac{d^2\sigma}{d\Omega dE'} = \frac{k'}{k}\sum_{j,j'} b^*_{j'} b_j \mathcal{F}_t\langle e^{-i\mathbf{q}\cdot\mathbf{R}_{j'}} e^{i\mathbf{q}\cdot\mathbf{R}_j(t)}\rangle \tag{2.14}$$

with the ensemble average $\langle\ldots\rangle = \sum_\lambda n_\lambda\langle\lambda|\ldots|\lambda\rangle$

2.2 Coherence and Incoherence

For a pure target that has only one nuclide with nuclear spin $I = 0$, we have $b_j = b$ for every j, and if the inter atomic distance d is always the same, the neutron scattering is coherent and the double differential cross section simplifies to the form

$$\left(\frac{d^2\sigma}{d\Omega dE'}\right)_{\text{no isotopes, } I=0} = \frac{k'}{k}|b|^2 \sum_{j,j'} \mathcal{F}_t\langle e^{-i\mathbf{q}\cdot\mathbf{R}_{j'}} e^{i\mathbf{q}\cdot\mathbf{R}_j(t)}\rangle \tag{2.15}$$

that, considering a general displacement from the mean value of the nuclear position small enough compared to the internuclear distance d, has the two limit cases

$$\left(\frac{d\sigma}{d\Omega}\right)_{kd\ll 1} = 2|b|^2 \qquad\qquad \left(\frac{d\sigma}{d\Omega}\right)_{kd\gg 1} = |b|^2 \tag{2.16}$$

In an actual situation these ideal conditions are not satisfied, and so two quantities are defined, $\langle b\rangle = \sum f_i b_i$ and $\langle |b|^2\rangle = \sum f_i |b|_i^2$, with f_i the fraction of atoms of type i. The scattering can be thought as composed of two contributions

$$\left(\frac{d^2\sigma}{d\Omega dE'}\right)_C = \frac{k'}{k}|\langle b\rangle|^2 \sum_{j,j'} \mathcal{F}_t \langle e^{-i\mathbf{q}\cdot\mathbf{R}_{j'}} e^{i\mathbf{q}\cdot\mathbf{R}_j(t)}\rangle \tag{2.17}$$

where pairs of atoms are considered together with their interference effects, and

$$\left(\frac{d^2\sigma}{d\Omega dE'}\right)_I = \frac{k'}{k}\left(\langle |b|^2\rangle - |\langle b\rangle|^2\right) \sum_{j} \mathcal{F}_t \langle e^{-i\mathbf{q}\cdot\mathbf{R}_{j}} e^{i\mathbf{q}\cdot\mathbf{R}_j(t)}\rangle \tag{2.18}$$

where atoms are considered individually. Finally, for the total cross section we have

$$\frac{\sigma_T}{4\pi} = \langle |b|^2\rangle = |\langle b\rangle|^2 + \left(\langle |b|^2\rangle - |\langle b\rangle|^2\right) = |b_C|^2 + |b_I|^2 = \frac{\sigma_C + \sigma_I}{4\pi} \tag{2.19}$$

The sources of incoherent scattering are in those situations that neglect the three hypothesis of Eq. 2.15, and they are referred to as isotopic or spin incoherence. For example, the scattering length depends on the spin of the system nucleus + neutron, giving rise to two different length, b^+ relative to the state $I + \frac{1}{2}$ and b^- relative to the state $I - \frac{1}{2}$, with I the spin of the nucleus. If the only difference in the atoms of a target is in their spin, the averages above are evaluated from the spin statistics with the weight

$$g_+ = \frac{I+1}{2I+1} \qquad\qquad g_- = \frac{I}{2I+1} \tag{2.20}$$

In terms of these weights it is possible to define the coherent and incoherent cross sections (in the case of simple spin incoherence) as:

$$\frac{\sigma_S}{4\pi} = g_+|b_+|^2 + g_-|b_-|^2 \qquad \frac{\sigma_C}{4\pi} = |g_+ b_+ + g_- b_-|^2 \qquad \frac{\sigma_I}{4\pi} = g_+ g_- |b_+ - b_-|^2 \tag{2.21}$$

from which is straightforward the definition of b_C and b_I, and, for the inverse transformations,

$$b_+ = b_C + \sqrt{\frac{g_-}{g_+}} b_I \qquad\qquad b_- = b_C - \sqrt{\frac{g_+}{g_-}} b_I \tag{2.22}$$

and, of course and by definition,

Element	σ_C [barn]	σ_I [barn]	σ_A[barn]
H	1.758	80.27	0.333
D	2.050	7.640	0.001
C	0.001	5.551	0.003
O	4.232	0.001	0.002
Ti	2.870	4.350	6.090
Fe	0.400	11.62	2.560
Zr	0.020	6.460	0.185
Sn	0.022	4.892	0.626

Table 2.1: Coherent and Incoherent neutron cross sections for some of the elements treated in this work.

$$b_C = g_+ b_+ + g_- b_- = \langle b \rangle \tag{2.23}$$

2.3 Incoherent Scattering

In this work on Inelastic Neutron Scattering (INS) we are principally concerned with single-particle dynamics. In Table 2.3 the coherent, incoherent and absorption cross sections for the atoms concerned to the present experiments are reported. As it can be appreciated, all the atoms but oxygen have a larger incoherent than coherent cross section. Then, we will develop our calculations with special interest on the incoherent phenomena.

2.4 Harmonic approximation

We approach the problem starting from the simplest case of a sample composed of a single element. We express every j-atom position as a mean position $\vec{j}$ plus a displacement $\vec{u}_j$. The spatial homogeneity of the sample guarantees that the correlation function

$$I(\mathbf{q}, t) = \frac{1}{N} \sum_j \langle e^{-i\mathbf{q}\cdot\mathbf{R}_j} e^{i\mathbf{q}\cdot\mathbf{R}_j(t)} \rangle = \langle e^{-i\mathbf{q}\cdot\mathbf{u}(0)} e^{i\mathbf{q}\cdot\mathbf{u}(t)} \rangle = \langle e^U e^V \rangle \tag{2.24}$$

evaluated on the ensemble average gives the same result for each of the N nuclei. If the forces in the sample are linear functions of the displacement with respect to the rest position, the system is harmonic and a superposition principle can be used to express the overall displacement as

the sum over normal modes. Therefore, the argument of the exponential can be developed in the normal mode expansion

$$\mathbf{q}\cdot\mathbf{u} = \left(\frac{\hbar}{2MN}\right)^{\frac{1}{2}} \sum_s \frac{\mathbf{q}\cdot\mathbf{e}_s}{\sqrt{\omega_s}}[a_s e^{-i\omega_s t} + a^\dagger e^{i\omega_s t}] \tag{2.25}$$

with a_s and $a_s^\dagger$ the creation and annihilation operator for a normal mode of energy $\hbar\omega_s$ in the $\mathbf{q}$ direction. Omitting some long calculations based on the commutation properties of a and $a^\dagger$ and hence U and V, it is possible to write

$$I(\mathbf{q},t) = \langle e^U e^V\rangle = e^{\langle U^2\rangle} e^{\langle UV\rangle} = \left(1 + \langle UV\rangle + \frac{1}{2!}\langle UV\rangle^2 \ldots \frac{1}{p!}\langle UV\rangle^p\right) e^{-2W}, \tag{2.26}$$

having introduced the series expansion known as phonon expansion, and having introduced the Debye - Waller factor

$$2W = \frac{\hbar}{2MN}\sum_s \frac{(\mathbf{q}\cdot\mathbf{e}_s)^2}{\omega_s}\langle 2n_s + 1\rangle = \frac{\hbar}{2MN}\sum_s \frac{(\mathbf{q}\cdot\mathbf{e}_s)^2}{\omega_s}\coth\left(\frac{\hbar\omega_s}{2k_BT}\right). \tag{2.27}$$

The number operator n_s appears through its quantum definition when creation and annihilation operators are applied. Its equality to $\coth\left(\frac{\hbar\omega_s}{2k_BT}\right)$ holds when the average of the operator is taken over an ensemble of Maxwell Boltzmann particles at temperature T.

The phonon expansion represents the ensemble of the processes when $1, 2 \ldots p$ neutrons lose $\hbar\omega > 0$ or gain $\hbar\omega < 0$ enough energy to insert or cancel a harmonic mode of frequency ω_s in the overall motion of the scattering centre. The Debye - Waller factor takes into account the fact that the scattering nucleus is indeed moving, and so it is in part delocalized in a volume whose linear dimension is of the order of $\sqrt{\langle u^2\rangle^2_{\text{modes}}}$. When ω is bigger enough with respect to K_BT, the hyperbolic cotangent function reaches the constant value 1, and the relation $\hbar\omega/4 = M\omega^2\langle u^2\rangle$ holds on a time scale greater than ω^{-1} and for a particle in its ground state.

The Incoherent cross section can be then read in the form

$$\left(\frac{d\sigma^2}{d\Omega dE'}\right)_I = \frac{\sigma_I}{4\pi}\frac{k'}{k}\frac{N}{2\pi\hbar}e^{-2W}\int_{-\infty}^{\infty}(1 + \langle UV\rangle\ldots)e^{-i\omega t}dt. \tag{2.28}$$

It is possible to obtain important pieces of information from INS considering only the first two terms of this expansion, in particular the second one. Indeed, the first term is the elastic contribution with no dependence on the energy transfer. It is expressed by a single differential cross section

$$\left(\frac{d\sigma}{d\Omega}\right)_{I,\text{elastic}} = \frac{\sigma_I}{4\pi}Ne^{-2W} \tag{2.29}$$

where a directional dependence can be found in the Debye-Waller factor. The second term corresponds to the one phonon creation or annihilation is expressed as a double differential

cross section

$$\left(\frac{d\sigma^2}{d\Omega dE'}\right)_{I,1\text{ ph}} = \frac{\sigma_I}{4\pi}\frac{k'}{k}\frac{1}{2M}e^{-2W}\sum_s \frac{(\mathbf{q}\cdot\mathbf{e}_s)^2}{\omega_s}\left[\langle n_s+1\rangle\delta(\omega-\omega_s)+\langle n_s\rangle\delta(\omega+\omega_s)\right]. \quad (2.30)$$

2.5 Dynamic Structure Factor

The appearance, in previous chapters, of a Fourier transform of the Intermediate correlation function, as well as its name, suggest that a more physical quantity can be related to the cross section. This quantity is called the Dynamic structure factor, and it is defined as

$$S(\mathbf{q},\omega) = \mathcal{F}_t I(\mathbf{q},\omega), \quad (2.31)$$

allowing a more direct definition of the incoherent double differential cross sectionas

$$\left(\frac{d^2\sigma}{d\Omega dE'}\right)_I = b_I\frac{k'}{k}NS(\mathbf{q},\omega). \quad (2.32)$$

Being this a shared property of all the nuclei in an homogeneous sample, the sum over all nuclei has been replaced with the dynamic structure factor times the number of scattering centres N. When compounds are considered, with more elements or isotopes composing the same molecule, different contributions are defined due to the dependence upon the mass and $(\mathbf{q}\cdot\mathbf{e}_s)$. Moreover, in this case the scattering from different elements is weighted by different cross sections as well. In the case of water, it is straightforward to introduce a H-projected dynamic structure factor, meaning that the experimental content is mainly related to the H small mass and high cross section. If only scattering processes with positive energy loss of the neutron are studied, looking at Eq. 2.30, we can express the dynamic structure factor as

$$S(\mathbf{q},\omega) = \frac{1}{2M}e^{-2W}\sum_s \frac{(\mathbf{q}\cdot\mathbf{e}_s)^2}{\omega_s}\langle n_s+1\rangle\delta\left(\omega-\omega_s\right) \quad (2.33)$$

The case of a discrete sum over well defined frequencies, $\sum_s \delta(\omega-\omega_s)$, well representing the case of a monoatomic crystal, is a too limiting condition when other samples, such as the water molecule at the base of the next discussion, are considered. The previous equations can be simply modified considering a continuous function $z(\omega)$ defined as the phonon density of states. In this case the condition $\int_0^\infty z(\omega)d\omega =$ number of modes, should be taken into account for the normalization of this function. Also, for a polycrystalline or isotropic material, the substitutions $(\mathbf{q}\cdot\mathbf{e}_s)^2 \to q^2$ and $2W = q^2\langle u^2\rangle$, with $\langle u^2\rangle$ representing the mean square displacement of the struck nucleus

$$S(\mathbf{q},\omega) = \frac{1}{2M}e^{-q^2\langle u^2\rangle}\frac{q^2}{\omega}z(\omega)\langle n+1\rangle. \quad (2.34)$$

This will be the basis for the data reduction of INS experiments proposed in the next Chapters 5, 6 and 7. Anyway, it is still possible to learn how water dynamics depends on the phonon density of states if the harmonic model is studied in detail. This will be done in the Chapter 4, where a discussion on how the information on the normal modes of this so important molecule can be used to determine the kinetic energy of its constituent atoms.

2.6 INS spectrometers

In order to evaluate the H density of states, the INS experiments we will discuss have been performed with the spectrometers Mari and Sequoia, whose experimental set up, geometry and detector configuration is discussed below.

Sequoia [31] is a fine resolution thermal - epithermal spectrometer located on the beamline 17 at the SNS of the Oak Ridge National Laboratory in Tennessee (USA). It works in direct geometry mode, with the initial energy of the neutron defined by a chopper, and the final energy evaluated with the time-of-flight (t.o.f.) technique.

Neutrons come out of a moderator composed of ambient-temperature water poisoned with Gd and encounter, after about 10 meters a first chopper (T_0 chopper). The purpose of the T_0 chopper is to suppress the prompt pulse of fast neutrons produced when the proton beam strikes the target. This suppression is accomplished by having an approximately 0.20 m thick piece of the alloy Inconel X-718 in the beam when the proton pulse hits the target. This piece of inconel must be out of the beam in sufficient time for the 0.01 - 2 eV neutrons to pass. It can operate at rotational speeds between 30 Hz and 180 Hz in multiples of 30 Hz.

At about 18 meters from the moderator a Fermi chopper reduces the large range of neutrons so far come and defines the incident energies in the suggested range from 5 meV to 4 eV. It is composed of a series of neutron adsorbing blades closely packed and able to rotate up to frequencies of 600 Hz around a vertical axis perpendicular to the beam line. The energy resolution can be of 2-5% of the energy transfer for incident energies lower than 100 meV, or of the 5-10% for higher incident energies.

Along the same line, at about 20 meters from the moderator, the sample position is at the centre of a cylindrical geometry covered by the detectors. In the horizontal plane passing through the sample, the detector distance is about 5.5 m. The detector array is an assembly of linear position sensitive detectors with dimensions 1.2 m (heigh) times 2.5 cm (width) and filled with ^{3}He at a pressure of 1 MPa. When a neutron enters a detector, the reaction $n+$ ^{3}He$\rightarrow$

$T+p$ generates a tritium and a proton sharing 0.76 MeV. The electron shower generated by the passage of these charged energetic particles are collected by wires at high voltage and with low resistance, able to determine the position along the detector where the neutron arrived. Knowing the position of the detector from the sample, the initial energy and the initial neutron path, it is possible to define the final energy of the neutron, and the energy transfer $\hbar\omega$ with a t.o.f. measure, and the angular position of the detectors, together with the initial and final energies will define the momentum transfer $\mathbf{q}$.

Mari is a chopper spectrometer in Target Station 1 at ISIS spallation neutron source in Oxfordshire, UK. A good resolution makes it ideal for the study of phonon densities of states in crystalline and disordered systems, and crystal field excitations in magnetic materials. It has a wide continuous detector bank coverage ranging from 3 degrees to 134 degrees. Being the only chopper spectrometer at ISIS not to be equipped with a pixilated detector array using position sensitive detectors, MARI is the instrument of choice for studies of polycrystalline and powdered samples, and liquids. MARI also boasts the lowest instrumental background of the ISIS suite of chopper spectrometers, making the machine highly sensitive despite the relatively low incident neutron flux. The moderator is composed of liquid methane at 105 K poisoned with Gd.

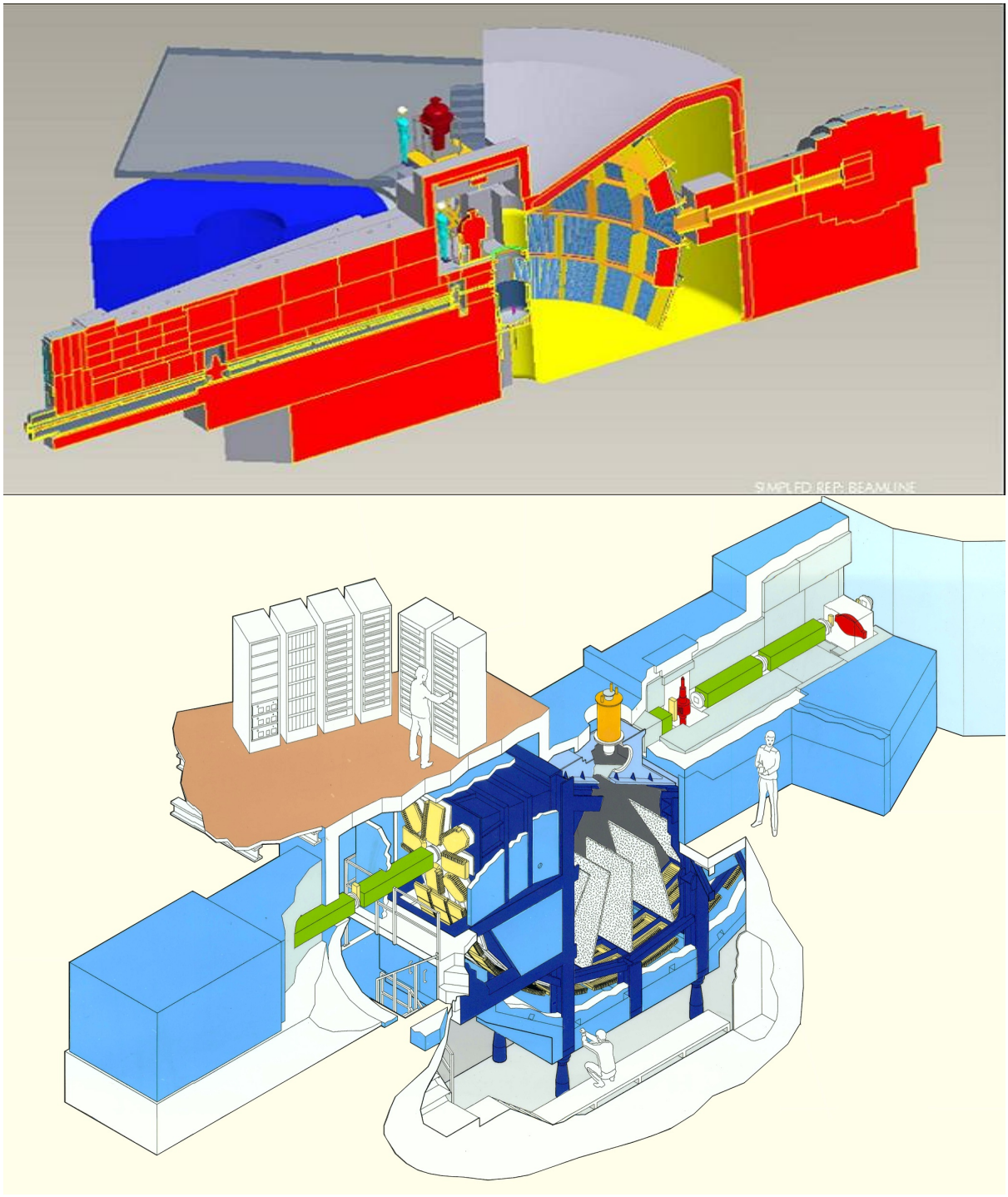

Figure 2.1: A picture of the Sequoia spectrometer (top) and the MARI spectrometer (bottom).

Chapter 3

Momentum Distributions

The main properties of the neutron Compton profile are presented as the main experimental tool of investigation in the following Chapters 5 and 6. In particular, I present some new symmetry properties, numerical improvements and physical conditions that I implemented in the data analysis of the experiments presented in this Thesis regarding the multivariate momentum distribution. These achievements have been introduced in the data reduction routines for future experiments on the VESUVIO spectrometer at ISIS.

3.1 Scattering from a single free nucleus

The Dynamic structure factor is generally related to the measure of vibrational spectra, as we will do in the experiments proposed in the next chapters. These vibrations are originated by potentials due to atoms surrounding the nucleus hit by the probing neutron. If no other atom was in the proximity of the one struck, going back to equation 2.10 and considering that also $|\lambda\rangle$ and $|\lambda'\rangle$ would be plane waves, the quantity

$$\langle\lambda'|e^{i\mathbf{q}\cdot\mathbf{R}}|\lambda\rangle = \int e^{(\hbar\mathbf{q}-\mathbf{p}+\mathbf{p}')\cdot\mathbf{R}/\hbar}d\mathbf{R} = \hbar\delta\left(\hbar\mathbf{q}-\mathbf{p}+\mathbf{p}'\right) \tag{3.1}$$

would request for momentum conservation by a Dirac δ function. The condition for momentum conservation is always fulfilled when no external forces are acting, as in this case. When we try to express $S(\mathbf{q},\omega)$ in terms of the so-simplified matrix elements, combining energy and momentum conservations, we have

$$S(\mathbf{q},\omega) = \sum_{\lambda} n_\lambda\,\delta\left(\hbar\omega - \frac{\hbar^2q^2}{2M} - \frac{\hbar\mathbf{q}\cdot\mathbf{p}}{M}\right). \tag{3.2}$$

Moreover, it is not possible to consider a discrete series for the average over all initial state since in the absence of an interaction energy is not quantized. We then have to substitute the sum with an integral over a continuous range of energy values. The result would then appear in the form

$$S(\mathbf{q},\omega) = \hbar \int n(\mathbf{p})\delta\left(\hbar\omega - \frac{\hbar^2 q^2}{2M} - \frac{\hbar\mathbf{q}\cdot\mathbf{p}}{M}\right) d\mathbf{p}. \tag{3.3}$$

The experimental conditions enabling the use of such a result in studies concerned with the condensed matter are fulfilled in the frame of Neutron Compton Scattering.

3.2 Momentum Distributions

Momentum distributions are indeed a key concept in a large part of modern Physics studies[1]. These quantities are needed in Compton-like scattering experiments, originally proposed by Compton [32] studying X-ray scattering by electrons, then applied to the measure of bound electron momentum distributions [33] and then generalized to all scattering processes where energy transfer is largely greater than any binding energy of the system. Deep Virtual Compton Scattering for the study of parton distribution functions in hadrons is an example.

It was first pointed out by Gol'ldanskii [34], Ivanof [35, 36], Hohenberg and Platzmann [37] that Neutron Compton Scattering (NCS), also named Deep Inelastic Neutron Scattering (DINS), could be a powerful tool for the study of atomic motions in condensed matter [38–41]. When, in an experiment, momentum, $\hbar\mathbf{q}$, and energy transfer, $\hbar\omega$, are much larger compared to momenta and energies characteristic of the system in its ground state, the Impulse Approximation (IA) can be applied. In this regime a single particle of the system is struck by the probe, according to our interest for incoherent scattering, and freely recoils after the scattering process. In principle, the conditions can be thought as those met in the case of a free single nucleus, with the exception that now we do not have only one scattering centre, but a great number of them, composing an ensemble of particles, and then a momentum or energy distributions can be accessed experimentally, together with the knowledge that they embed.

In theory, given the state $|\Psi\rangle$ describing the system, it is possible to define the momentum distribution through the annihilation and creation operators,

$$n(p) = \langle\Psi|a_p^\dagger\, a_p|\Psi\rangle \tag{3.4}$$

[1]This being fortunate for the Author, educated in hadron and parton phenomenology!

or considering the Fourier transform of the wave function,

$$n(p) = |\phi(p)|^2 = |\langle p|\Psi\rangle|^2 = \left|\frac{1}{\sqrt{2\pi}}\int dx e^{ipx/\hbar}\langle x|\Psi\rangle\right|^2 = \left|\frac{1}{\sqrt{2\pi}}\int dx e^{ipx/\hbar}\psi(x)\right|^2 \tag{3.5}$$

3.2.1 Fermi distributions

According to [42], atomic, electronic and nuclear systems, characterized by energies and inter-particle distances varying in a range containing several orders of magnitude, can all be treated in a very similar way. This is because the ratio of the typical binding energy and of the Fermi energy is constant for all these systems. Differences from a Maxwell - Boltzmann distribution can arise when the de Broglie wave length is comparable to interparticle distances, and in this case a strong dependence on Fermi or Bose statistics can be found. The limit temperature for the two regimes is defined as characteristic temperature and for a Fermi system it is derived from the Fermi energy, i.e. the highest single-particle energy level occupied at $T = 0$ K.

Since each energy level can be occupied by no more than one fermion, when no excitation due to thermal energy is added to the system, all lower energy levels are homogeneously occupied with a energy density $g(\omega) = g_0$, up to the level occupied by the most energetic particle, in the energy level E_F. The upper levels are no more occupied, with $g(\hbar\omega > E_F) = 0$. In this system the momentum distribution can be defined as

$$n_F(p) = n_0 \text{ for } p < p_F, \qquad n_F(p) = 0 \text{ elsewhere} \tag{3.6}$$

In particular, the Fermi energy for a metal like system at T = 0 K is defined as

$$E_F = \frac{p_F^2}{2m} = \frac{\hbar^2}{2m}\left(\frac{6\pi^2 n}{2\sigma+1}\right)^{\frac{2}{3}} \tag{3.7}$$

where $2\sigma + 1$ is the multiplicity due to the half-integer spin σ of the considered fermions. At a larger value of T, some fermions reach energy levels higher than E_F, and the momentum distribution is often taken of the form

$$n_F(p) = \frac{\mathcal{N}}{\exp(\frac{p^2 - p_F^2}{2mk_BT}) + 1} \tag{3.8}$$

that gives the previous result in the limit $T \to 0$. The factor $\mathcal{N}$ is not a normalization constant since this integral does not converge in the range $[-\infty, \infty]$. As an estimate of the importance of the statistics in the Water case, we can try to adapt the previous equation to the H in a H_2O molecule: the H spin is $\sigma_H = \frac{1}{2}$; the mass density is $\rho_H = \frac{1}{9}\rho_{H_2O} = 0.020$ a.m.u.Å^{-3} and $n_H = \rho_H/m_H$. The corresponding value of the Fermi wave number is $k_F = p_F/\hbar = 0.59$

$Å^{-1}$. We will later see that this value is an order of magnitude lower than the typical mean momentum of a water hydrogen, meaning that the quantum effect due to the fermionic nature of this atom is not important at the molecular level.

3.2.2 Harmonic and isotropic distribution

A result that we already used in the previous sections is to consider the weight n_λ, and then the probability function $n(p)$ for the simple case of a Maxwell Boltzmann distribution. In this case

$$n_\lambda = \frac{e^{-\beta E_\lambda}}{\sum_\lambda e^{-\beta E_\lambda}}, \tag{3.9}$$

with $\beta = 1/k_B T$ and k_B the Boltzmann constant. We know from the kinetic theory of gases that the mean kinetic energy of particles whose energies are distributed according to a Maxwell - Boltzmann statistical law is $\langle E_K \rangle = \frac{3}{2} k_B T$. Considering the dispersion relation $E = \frac{3p^2}{2M}$, we also know that the mean square momentum is $\langle p^2 \rangle = M k_B T$, and then the momentum distribution for a classical ensamble of non relativistic and non interacting particles is

$$n_{MB}(\mathbf{p}) = \left(\frac{1}{2\pi M k_B T} \right)^{\frac{3}{2}} e^{-\frac{p^2}{2M k_B T}} \tag{3.10}$$

The momentum distribution and the mean kinetic energy are generally related throught the equation

$$\int p^2 n(\mathbf{p}) d\mathbf{p} = 4\pi \int_0^\infty p^4 n(p) dp = 2M \langle E_K \rangle \tag{3.11}$$

The approximations for the validity of Eq. 3.12 are based on the fact that particles are non interacting in a perfect gas at thermodynamic equilibrium. Also, the momentum distribution has no angular dependence, and the wave function and the potential can be considered isotropic. A first generalization of Eq. 3.12 for interacting particle in an isotropic potential is

$$n_H(\mathbf{p}) = \frac{\exp\left(-\frac{p^2}{2M k_B T_*}\right)}{\sqrt{2\pi M k_B T_*}^3} = \frac{\exp\left(-\frac{p^2}{2\hbar^2 \sigma^2}\right)}{(\sqrt{2\pi}\sigma)^3} \tag{3.12}$$

with T_* an effective temperature taking into account the contributions from the interaction to $\langle E_K \rangle$, and $\sigma^2 = M k_B T_*$. In this case the (higher) mean kinetic energy can be directly related to the standard deviation σ and has the value

$$\langle E_K \rangle_H = \int p^2 n_H(\mathbf{p}) d\mathbf{p} = 4\pi \int_0^\infty p^4 n_H(p) dp = \frac{3\hbar^2 \sigma^2}{2M} \tag{3.13}$$

The condition for the validity of this equation is that the local nuclear potential must be isotropic and harmonic, since a Gaussian wave function and the resulting Gaussian momentum

distribution of Eq. 3.12 are the solution of a Schroedinger equation with a quadratic potential $V(r) = \frac{1}{2}M\frac{k_B^2 T_*^2}{\hbar^2}r^2$.

3.2.3 Anharmonic isotropic distribution

A Gaussian function for the momentum distribution can only be related to a harmonic potential $V(x) = \frac{1}{2}M\omega x^2$ with a quadratic dependence on the displacement from the mean position of the nucleus, x. Even if this is the basic assumption for all potentials in Nature, a number of deviations from this simple frame have been observed and related to mechanical deviations from the harmonic potentials, as cubic contributions (strongly related to thermal expansion of matter), or quantum effects such as the possibility of tunneling of the nucleus between double potential wells. It is generally not possible to find an analytical solution for complex potentials in condensed matter, and then a general form of the momentum distribution is introduced [43]

$$n_A(p) = \frac{\exp\left(-\frac{p^2}{2\hbar^2\sigma^2}\right)}{(\sqrt{2\pi}\sigma)^3}\sum_n a_n(-1)^n L_n^{\frac{1}{2}}\left(\frac{p^2}{2\sigma^2}\right) \tag{3.14}$$

with $L_n^{\frac{1}{2}}(x)$ the generalized Laguerre polynomials defined by

$$L_n^{\alpha}(x) = \frac{x^{-\alpha}e^x}{n!}\frac{d^n}{dx^n}\left(e^{-x}x^{n+\alpha}\right) \tag{3.15}$$

Equation 3.14 represents a function base and can then describe any momentum distribution. The Gaussian leading term is corrected by polynomials of decreasing importance, due to the numerical factors by which they are weighted. The first terms of this expansion are

$$L_0^{\frac{1}{2}}(x) = 1 \tag{3.16}$$

$$L_1^{\frac{1}{2}}(x) = \frac{1}{1!2^1}(3-2x) \tag{3.17}$$

$$L_2^{\frac{1}{2}}(x) = \frac{1}{2!2^2}(15-20x+4x^2) \tag{3.18}$$

$$L_3^{\frac{1}{2}}(x) = \frac{1}{3!2^3}(105-201x+84x^2-8x^3) \tag{3.19}$$

Each of these terms appears together with a coefficient a_n taking into account the importance of each contribution. We notice that, due to the properties of $n(p)$, the coefficient a_1 must vanish, while the leading Gaussian term has a weight $a_0 = 1$. The mean kinetic energy in this case

$$\langle E_K\rangle_A = \int p^2 n_A(\mathbf{p})d\mathbf{p} = 4\pi\int_0^\infty p^4 n_A(p)dp = \frac{3\hbar^2\sigma^2}{2M} = \langle E_K\rangle_H \tag{3.20}$$

does not differes from the result of a simple Gaussian momentum distribution.

3.2.4 Multivariate anisotropic distribution

If anisotropy is more important, or more simple to measure, than deviations from an harmonic model, a multivariate Gaussian function can be used to describe the system:

$$n_M(\mathbf{p}) = \Pi_\alpha \mathcal{N}_\alpha \exp\left(-\frac{p_\alpha^2}{2\hbar^2\sigma_\alpha^2}\right) = \mathcal{N}\exp\left(-\frac{p_x^2}{2\hbar^2\sigma_x^2} - \frac{p_y^2}{2\hbar^2\sigma_y^2} - \frac{p_z^2}{2\hbar^2\sigma_z^2}\right) \tag{3.21}$$

with $\alpha = x, y, z$ three spatial directions, $\mathcal{N}_\alpha = \frac{1}{\sqrt{2\pi}\sigma_\alpha}$ and $\mathcal{N} = \Pi_\alpha \mathcal{N}_\alpha$ the normalization factor. In the case of water molecule, it is possible to simplify the local potential affecting the H atom, as the product of three decoupled harmonic potentials, one per spatial degree of freedom, and with the stronger potential in the direction of the covalent bond (stretch mode). The resulting wave function, as well as the momentum distribution, is the product of three unidimensional Gaussian functions. The parameters σ_α represent the mean momenta along the three axes, and for each direction a mean kinetic energy $\langle E_K\rangle_\alpha$ is defined,

$$\langle E_K\rangle_M = \int\left(\sum_\alpha p_\alpha^2\right) n_M(\mathbf{p})d\mathbf{p} = \sum_\alpha \int_{-\infty}^{\infty} \mathcal{N}_\alpha p_\alpha^2 e^{-\frac{p_\alpha^2}{2\hbar^2\sigma_\alpha}} dp_\alpha = \sum_\alpha \frac{\hbar^2\sigma_\alpha^2}{2M} = \sum_\alpha \langle E_K\rangle_\alpha \tag{3.22}$$

In Chapter 4 a general interpretation for these quantities in relation with the geometry and dynamics of the water molecule is discussed. The Cartesian components of the vector $\mathbf{p}$, (p_x, p_y, p_z) can be transformed in the more proper polar components, (p, θ, ϕ) according to the transformation

$$p_x = p\cos\phi\sin\theta \qquad p_y = p\sin\phi\sin\theta \qquad p_z = p\cos\theta \tag{3.23}$$

In what follows we will prefer the polar coordinates because, for any powder, liquid or non oriented sample, we have different orientations for each atom, and only an angular average $n(p)$ of the previously defined $n(\mathbf{p})$ can be accessed. In particular,

$$n_M(p) = \int_\Omega \frac{d\Omega}{4\pi} n_M(\mathbf{p}) = \mathcal{N}\int_\Omega \frac{d\Omega}{4\pi}\exp\left(-\frac{p^2}{2}\left[\frac{\sin^2\theta\cos^2\phi}{\sigma_x^2} + \frac{\sin^2\theta\sin^2\phi}{\sigma_y^2} + \frac{\cos^2\theta}{\sigma_z^2}\right]\right) \tag{3.24}$$

The angular dependence in this function can be restricted in the quantity

$$\frac{1}{S^2(\theta,\phi)} = \frac{\sin^2\theta\cos^2\phi}{\sigma_x^2} + \frac{\sin^2\theta\sin^2\phi}{\sigma_y^2} + \frac{\cos^2\theta}{\sigma_z^2} \tag{3.25}$$

We first notice that in the case of isotropy, $\sigma_\alpha = \sigma\,\forall\alpha$, we have the simple case $S^2(\theta,\phi) = \sigma^2$ and $n_M(p) = n_H(p)$, as it should be. Secondly, there is a strong symmetry of the argument of the integral with respect to the integration domain, since the periodic trigonometric functions appear always as squared functions. In particular, we can simplify the integration domain as follows

$$\int_\Omega \frac{d\Omega}{4\pi} \quad\rightarrow\quad \int_{-1}^{1}\frac{d(\cos\theta)}{2}\times\int_0^{2\pi}\frac{d\phi}{2\pi} \quad\rightarrow\quad \frac{2}{\pi}\int_0^1 d(\cos\theta)\int_0^{\frac{\pi}{2}} d\phi \tag{3.26}$$

i.e., we used an 8-fold symmetry and we can look at only 1 part over 8 of the ellipsoidal momentum distribution. The use of this symmetry will be of great help when we will use this momentum distribution as the base of the fit procedure in the data analysis.

3.3 y-scaling in the Impulse Approximation

Now that we have a number of functions describing different physical situations, we can develop the experimental method used in order to analyse experimental data. Firstly, looking back at the condition for energy conservation in Eq. 3.3, we can introduce the recoil energy $\hbar\omega_r = \frac{\hbar^2 q^2}{2M}$ as the amount of energy gained by a still (but not fixed) nucleus, and write

$$\hbar\omega - \frac{\hbar^2 q^2}{2M} - \frac{\hbar\mathbf{q}\cdot\mathbf{p}}{M} = \hbar\omega - \hbar\omega_r - \frac{\hbar^2 q}{M} y = 0 \tag{3.27}$$

with the introduction of the quantity $\hbar y$, corresponding to the momentum of the target nucleus in the direction of $\mathbf{q}$ before the scattering, namely

$$y = \frac{1}{\hbar}\mathbf{p}\cdot\hat{\mathbf{q}} = \frac{M}{\hbar q}\left(\omega - \frac{\hbar q^2}{2M}\right) \tag{3.28}$$

We notice that y vanishes both if the target nucleus is stationary or if it is moving perpendicularly to $\mathbf{q}$. During an experiment in which $\hbar\mathbf{q}$ and $\hbar\omega$ are both measured, it is possible to access the probability distribution of finding a nucleus with a certain value of y, corresponding to the neutron Compton profile, $J(y)$. This quantity is simply interpretable as the projection of the momentum distribution $n(\mathbf{p})$ in the y-space, that is

$$J(y) = \hbar \int n(\mathbf{p})\delta\left(\hbar y - p_\parallel\right) d\mathbf{p} = \hbar \int n(\mathbf{p}_\perp, \hbar y) d\mathbf{p}_\perp \tag{3.29}$$

with the consideration $J(y) = \hbar J(\hbar y)$ and $\mathbf{p} = (\mathbf{p}_\perp, p_\parallel = \mathbf{p}\cdot\hat{\mathbf{q}})$. The West variable, combining momentum and energy transfer according to Eq. 3.27 allows the definition of a function, $J(y)$, that no more depends on $\mathbf{q}, \omega$ separately, but only on y. Since the momentum conservation at the base of the definition of the West variable is only an approximation ($\mathbf{q}, \omega \to \infty$), the validity of this scaling law holds only in limiting cases, in a regime known as the Impulse Approximation (IA). The dynamic structure factor in this regime is generally expressed as

$$S(\mathbf{q},\omega) = \hbar \int n(\mathbf{p}) \frac{M}{\hbar q} \delta\left(\hbar y - p_\parallel\right) d\mathbf{p} = \frac{M}{q} J(y) \tag{3.30}$$

leading to the formulation of its scaling property in the form

$$qS(\mathbf{q},\omega) = \text{function of } y \text{ only} \tag{3.31}$$

It exist a West variable for each element (or isotope) composing the experimental sample, since the definition of y is based on the mass M of the struck nucleus. This means that the momentum distributions and neutron Compton profiles of more elements can be studied simultaneously. For a disordered or non oriented sample the dynamic structure factor must be invariant under spatial reflections of the momentum transfer, that is $S(-\mathbf{q},\omega) = S(\mathbf{q},\omega)$, and then the neutron Compton profile is a even function of y, with a maximum for $y = 0$, meaning that the mean momentum of the nucleus in the direction of $\mathbf{q}$ is zero, even if the nucleus is certainly moving. Also, the normalization of the momentum distribution is naturally reflected in the normalization of $J(y)$. For every isotropic momentum distribution, $n(\mathbf{p}_\perp, \hbar y) = n(p_\perp^2 + \hbar^2 y^2) = n(p^2)$, Eq 3.29 can be expressed using polar coordinates for the variable $\mathbf{p}_\perp$, as follows

$$J(y) = 2\pi\hbar \int_0^\infty p_\perp n(p_\perp, \hbar y) = 2\pi\hbar \int_{|\hbar y|}^\infty p n(p) \tag{3.32}$$

leading to the also useful reverse equation

$$n(p) = \left(\frac{1}{2\pi\hbar^3 y} \frac{d}{dy} J(y) \right)_{\hbar y = p} \tag{3.33}$$

3.3.1 Deviations from the impulse approximation

Sensible deviations from the approximation discussed since now can come any time that the momentum transfer fails to be high enough. In this case interactions due to external forces sensibly affect the final trajectory of the struck particle. The scaling is no more exactly satisfied and an additional dependence on the momentum transfer must be considered. A well tested procedure [44] in considering these Final State Effects (FSE) is with an additive correction of terms in powers of $1/q$, as follows

$$J(y,q) = J(y) + \Delta J(y,q) = J(y) + \sum_{n=3}^{\infty} (-1)^n A_n(q) \frac{d^n}{dy^n} J(y) \tag{3.34}$$

The coefficient A_n are introduced in order to consider the inter particle potential, V, and are of the form

$$A_n(q) = \begin{cases} 1 & , n = 0 \\ 0 & , n = 1, 2 \\ O\left(\frac{1}{q}\right) & , n = 3, 4 \dots \\ O\left(\frac{1}{q^2}\right) & , n = 4, 6 \dots \end{cases} \tag{3.35}$$

The first term is defined as

$$A_3 = \frac{M}{36\hbar^2 q}\langle\nabla^2 V\rangle \tag{3.36}$$

where the Laplace operation on the potential, for an harmonic potential, is of the form

$$\langle\nabla^2 V\rangle = 3\bar{\omega}^2 = \frac{12\hbar^2\bar{\sigma}^4}{M} \tag{3.37}$$

having introduced the mean curvature of the potential, $\hbar\bar{\omega} = 2\hbar^2\bar{\sigma}^2/M$, that, in the case of the multivariate momentum distribution, is the average of the three curvatures $\hbar\omega_\alpha = 2\hbar^2\sigma_\alpha^2/M$. With this consideration, we can express the first term in this correction series as

$$A_3 = \frac{\bar{\sigma}^4}{3q} \tag{3.38}$$

Considering the same case, that is a general treatment for the already mentioned momentum distributions $n_M(p)$ and $n_H(p)$, we can express the second correction term, found in the literature as

$$A_4 = \frac{m^2}{72\hbar^4 q^2}\langle F^2\rangle = \frac{m^2}{72\hbar^4 q^2}\langle E_K\rangle\langle\nabla^2 V\rangle \tag{3.39}$$

as a function of the average mean square momentum only

$$A_4 = \frac{\bar{\sigma}^6}{6q^2} \tag{3.40}$$

As we will see in a moment, the fact that these parameters can be expressed as functions of an already introduced parameter, allows the fit procedure to be largely more accurate fixing the meaning of parameters that in the past were considered free.

We will now define the neutron Compton profile (NCP) $J(y,q)$ of Eq. 3.34, considering the terms with $n = 1,\ldots,4$, in the case of harmonic isotropic and multivariate momentum distributions.

3.3.2 Harmonic and isotropic $J(y,q)$

The neutron Compton profile in the IA for a system whose momentum distribution is harmonic and isotropic is defined through Eqs. 3.32 and 3.12, that is

$$J_H(y) = 2\pi\hbar\int_{|\hbar y|}^{\infty} p n_H(p)dp = \frac{\exp\left(-\frac{y^2}{2\sigma^2}\right)}{\sqrt{2\pi}\sigma} \tag{3.41}$$

The first correction due to FSE is in the form

$$-A_3\frac{d^3}{dy^3}J(y) = \frac{\sigma}{3q}\frac{1}{\sqrt{2}^3}H_3\left(\frac{y}{\sqrt{2}\sigma}\right)J(y) \tag{3.42}$$

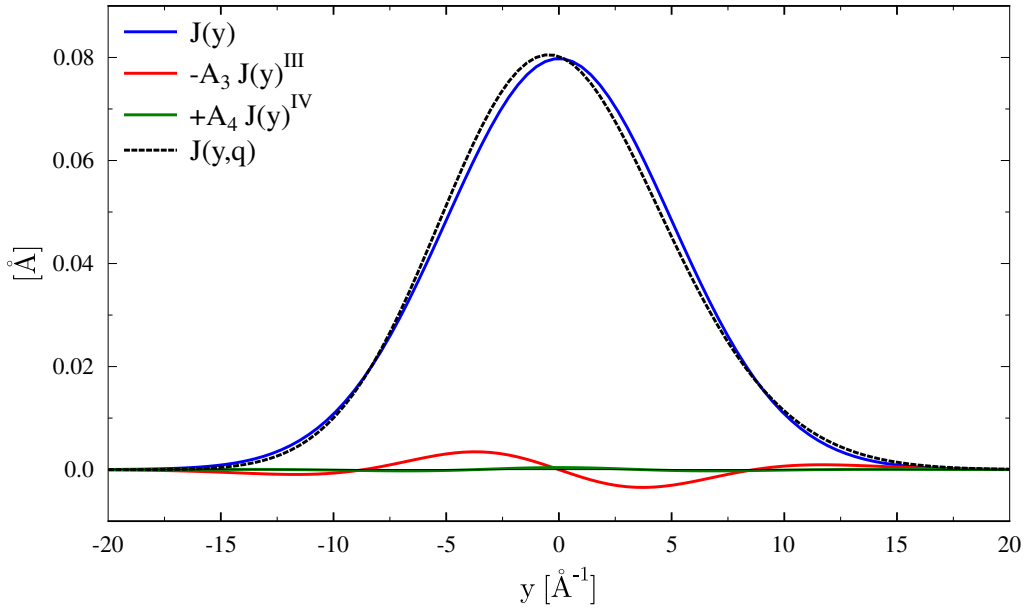

Figure 3.1: A neutron Compton profile is reported with (blue line, J(y,q)) and without (black line, J(y)) the FSE contributions in the case of a harmonic and isotropic momentum distribution with a value of $\sigma = 5$ Å^{-1}. A constant value for the momentum transfer $q = 70$ Å^{-1} has been considered.

with $H_3(x) = 8x^3 - 12x$. This is a structured correction, with a polynomial dependence upon y, and with an intensity weighted by the ratio σ/q. The following term is, similarly,

$$+A_4 \frac{d^4}{dy^4} J(y) = \frac{\sigma^2}{6q^2} \frac{1}{\sqrt{2}^4} H_4\left(\frac{y}{\sqrt{2}\sigma}\right) J(y) \tag{3.43}$$

with $H_4(x) = 16x^4 - 48x^2 + 12$. The final result for the $J(y,1)$ is then the sum of the leading order and these two corrections, that is

$$J(y,q) = J(y)\left[1 + \frac{\sigma}{3q}\frac{1}{\sqrt{2}^3} H_3\left(\frac{y}{\sqrt{2}\sigma}\right) + \frac{\sigma^2}{6q^2}\frac{1}{\sqrt{2}^4} H_4\left(\frac{y}{\sqrt{2}\sigma}\right)\right] \tag{3.44}$$

In the Figure 3.1 it is possible to see how the the two considered terms will affect the measured neutron Compton profile. The A_3 correction is an odd function of y, positive for $y \in [-\epsilon, 0]$ and negative for $y \in [0, \epsilon]$, contributing the an apparent shift of the centre of the NCP towards negative values of y. The A_4 contribution is an even function of y and it is generally small enough to be neglected as a contribution in an experiment.

3.3.3 Anharmonic $J(y,q)$

Similarly, through the definition Eq. 3.32 we can define a general function base with the physical interpretations of an isotropic but non-harmonic system relative to the momentum distribution of Eq. 3.14, that is

$$J_A(y,q) = \frac{\exp\left(-\frac{p^2}{2\sigma^2}\right)}{\sqrt{2\pi}\sigma} \sum_n \frac{c_{2n}}{n!2^{2n}} H_{2n}\left(\frac{y}{\sqrt{2}\sigma}\right) \tag{3.45}$$

with the first even Hermite polynomials

$$H_0(x) = 1 \tag{3.46}$$

$$H_2(x) = 4x^2 - 2 \tag{3.47}$$

$$H_4(x) = 16x^4 - 48x^2 + 12 \tag{3.48}$$

$$H_6(x) = 64x^6 - 480x^4 + 720x^2 - 120 \tag{3.49}$$

The condition on the normalization of $J(y)$ to unity, and its second moment in y equal to the standard deviation of the profile, require that c_0=1 and $c_2 = 0$ In principle, with this neutron Compton profile it is possible to fit any experimental profile, using σ, c_{2n} as fit. parameters, but still the physical interpretation of the coefficients is hard. Since the polynomials term added to the leading Gaussian are corrections to it, the FSE can be derived from the precedent section as that of a harmonic $J(y)$. The resulting $J(y,q)$ is in the form

$$J(y,q) = J(y)\left[1 + \frac{\sigma}{3q}\frac{1}{\sqrt{2}^3}H_3(x) + c_2 H_2(x) + c_4 H_4(x) + c_6 H_6(x)\right]_{x=\frac{y}{\sqrt{2}\sigma}} \tag{3.50}$$

3.3.4 Multivariate $J(y,q)$

Similarly, the neutron Compton profile related to a multivariate Gaussian momentum distribution together with the first correction of the FSE is derived using Eqs. 3.32 and 3.21

$$J_M(y) = \frac{1}{\sqrt{2\pi}\sigma_x\sigma_y\sigma_z}\frac{2}{\pi}\int_0^1 d(\cos\theta)\int_0^{\frac{\pi}{2}} d\phi S^2(\theta,\phi)\exp\left(-\frac{y^2}{2S^2(\theta,\phi)}\right). \tag{3.51}$$

As already mentioned, the angular integration of this function is a key aspect in the data analysis of the next experiments, since in a fit procedure this integration can be called a huge number of times, and the time required by the fit can be very large. As it is shown in the Fig 3.2, it is not possible to consider the fitting procedure stable if the number of steps for the angular integration both in $d(\cos\theta), d\phi$ is less then 35×35, that means more than 1×10^3 passages any time that the function is called. This potential complication can be anyway avoided through a deeper analysis in Fig. 3.3. In this Figure, the red, dark-red and green lines are the difference of

two integrated multivariate distributions: one has been integrated with a 45×45 grid in $\cos\theta, \phi$ and is takes as a *best integration*, while the others vary from 20×20 (red line) to 36×36 (green line). According to the previous section, the finer the integration grid, the more the integrated distribution converges to the *right value* or, equivalently, to the *best integration*. Moreover, the same difference is taken with a large integration grid defined by 12×12 steps. This difference divided by a factor of 10 is reported as an orange line in the Figure. The orange and green lines are approximately the same line, meaning that a more rough integration (12×12) does not differ from a finer integration (36×36) but for a constant value. On the other hand, when the difference of an isotropic distribution with the same width of the 45×45 integrated momentum distribution is taken, a difference with structural nodes appears (black line in the Figure, but see also Figure 3.5). With this in mind, it is clear that, if in the fitting procedure the amplitude of the profile is a free parameter, a wrong normalization constant due to a rough integration grid can be fixed in the very fitting parameter, and a faster estimate of the multivariate profile, with 12^2 steps, can be done.

In the same Fig. 3.3, it is possible to appreciate the different structures of a multivariate profile with respect to the isotropic one. The big difference between the two profiles in $y = 0$ is a simple consequence of the difference between the normalization constants and then the value that the function has at the origin, namely

$$\frac{\sigma_x\sigma_y\sigma_z}{\sigma^3} = \frac{3^{\frac{3}{2}}\sigma_x\sigma_y\sigma_z}{(\sigma_x^2+\sigma_y^2+\sigma_z^2)^{\frac{3}{2}}} > 1 \tag{3.52}$$

Also, there are 4 points, two in the figure and other symmetric two in the $y < 0$ region, where the two profiles intersect. However, the difference that mostly is important in NCS experiments, is the fact that in the region of the tail, the multivariate profile is always greater than the isotropic one, this bringing to the conclusion that, generally, a fit of an experimental line shape done with a multivariate momentum distribution will correspond to a higher kinetic energy with respect to an isotropic fit on the same data.

The FSE corrections are taken into account as before, with a small adaptation to the present case, giving the following result as the consequence of the passages in Appendix B

$$-A_3(q)\frac{d^3}{dy^3}J(y) = \frac{\sigma_x^4+\sigma_y^4+\sigma_z^4}{9\sqrt{2\pi}\sigma_x\sigma_y\sigma_z q}\int_\Omega d\Omega\left[\frac{y^3}{S^2(\theta,\phi)^4} - 3\frac{y}{S^2(\theta,\phi)^2}\right]\exp\left(-\frac{y^2}{2S^2(\theta,\phi)}\right) \tag{3.53}$$

In Fig. 3.3.4 it is possible to appreciate the difference of NCPcorrected by FSE and of the corrections themselves in the case of isotropic and multivariate distributions. While the functions in the IA would share the same position of the centroid, the corrected profile may have their maximum value in two different points due to the small difference in the two corrections.

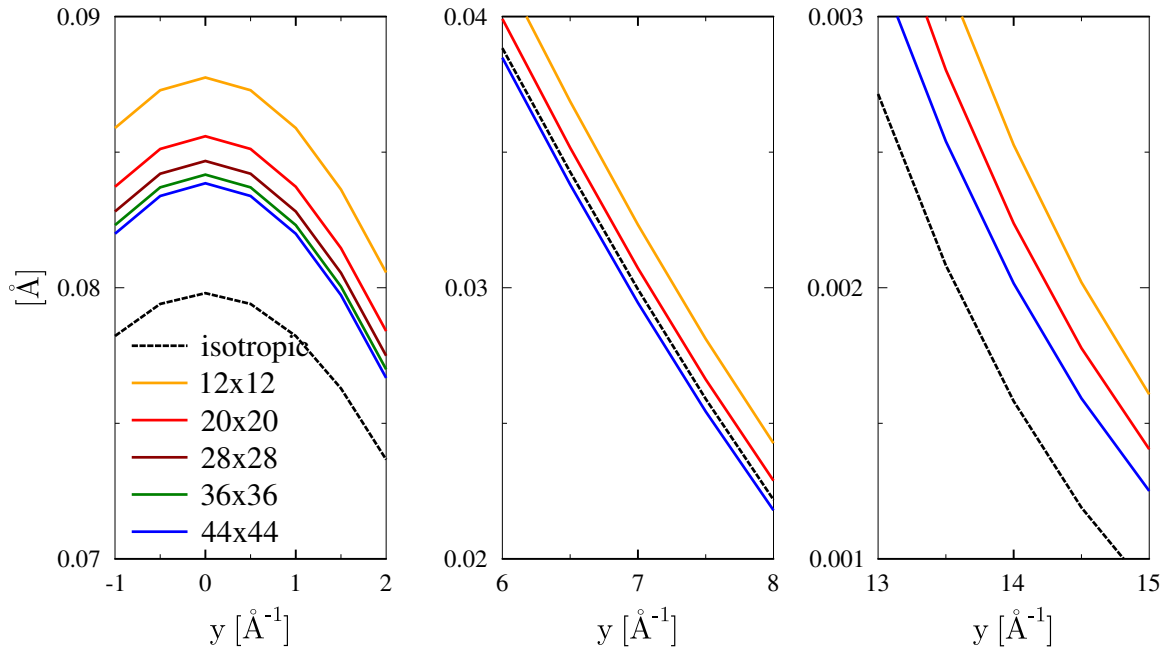

Figure 3.2: The multivariate neutron Compton profile as the result of a numerical integration in the variables $\cos\theta$ and ϕ. The numbers reported in the caption are the pairs of steps $(n_{\cos\theta}, n_\phi)$.

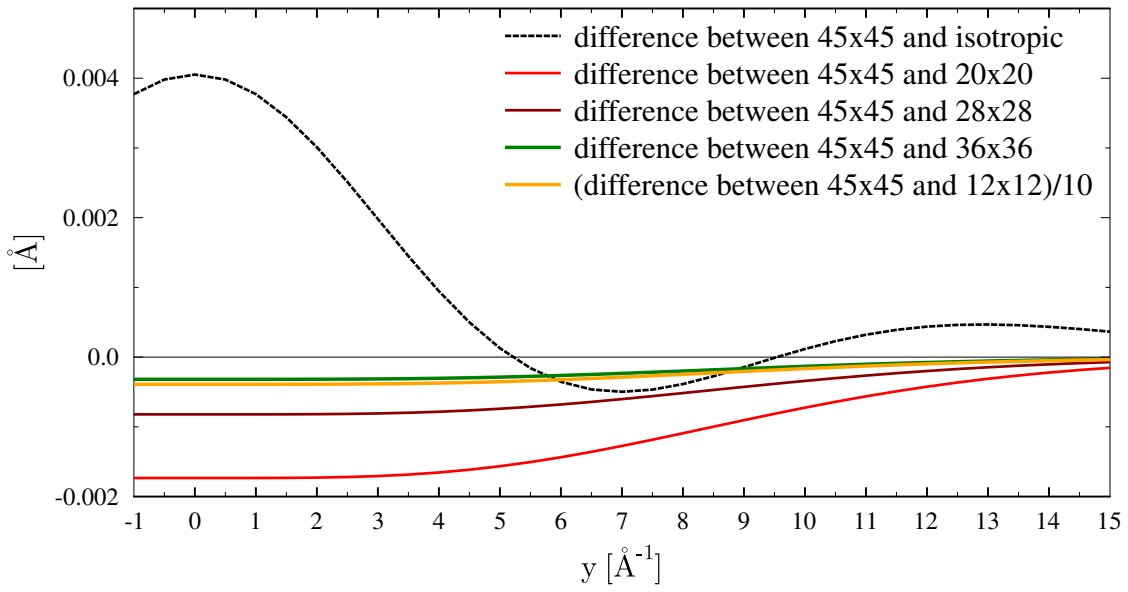

Figure 3.3: The multivariate neutron Compton profile as the result of a numerical integration in the variables $\cos\theta$ and ϕ. The numbers reported in the caption are the pairs of steps $(n_{\cos\theta}, n_\phi)$.

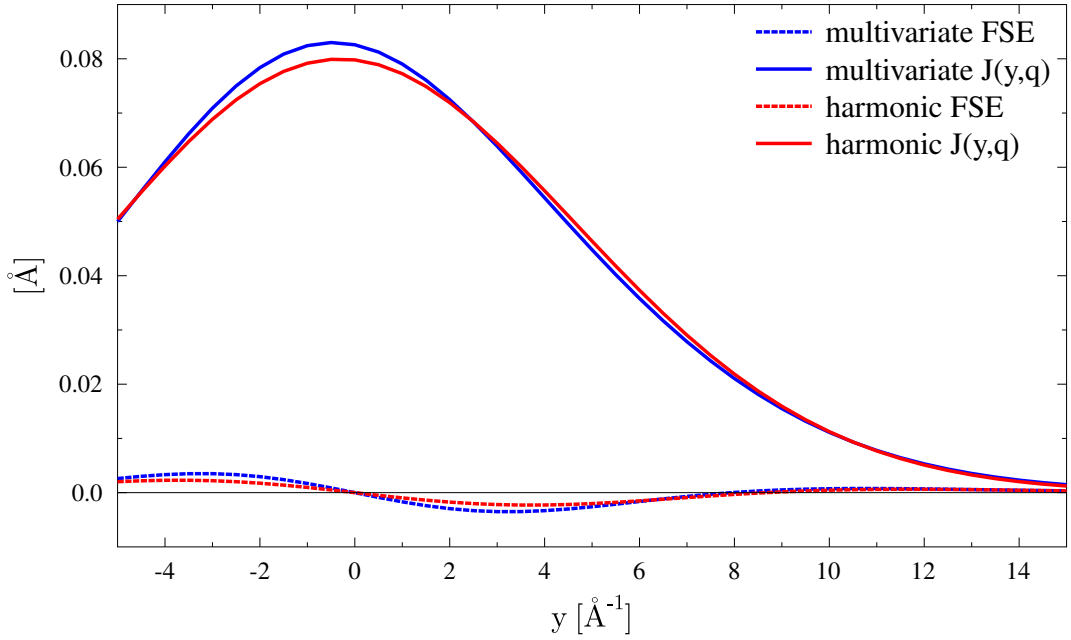

Figure 3.4: The multivariate neutron Compton profile as the result of a numerical integration in the variables $\cos\theta$ and ϕ. The numbers reported in the caption are the pairs of steps $(n_{\cos\theta}, n_\phi)$.

3.3.5 $J_M(y)$ as a Gauss-Hermite expansion

The isotropic momentum distribution has a practical important advantage: the very lower amount of time required for a fit. This problem has been introduced in the previous section, where we found the minimum number of steps for the angular integration in order to minimize it. An alternative way would be to relate the anisotropy of the distribution defined by the parameters σ_α to the first terms in the series defining the very general distribution $J_A(y)$. We then underline that we defined the Gauss-Hermite expansion as *anharmonic* because it can be so in principle, but there are some conditions that leave it harmonic, such as all the coefficients of the polynomials vanishing or the relations that we are going to deduce. The road that we intend to follow is the following.

We can imagine that, when the quality of data is good enough, a measure of the second, forth and sixth moment of $J(y)$

$$M_{2n}[J(y)] = \int_{-\infty}^{\infty} y^{2n} J(y) dy \qquad n = 1, 2, 3 \tag{3.54}$$

can be determined as non dependent upon the model and not affected by the noise on the tails of the distribution. These quantities have a different expression depending on the used model,

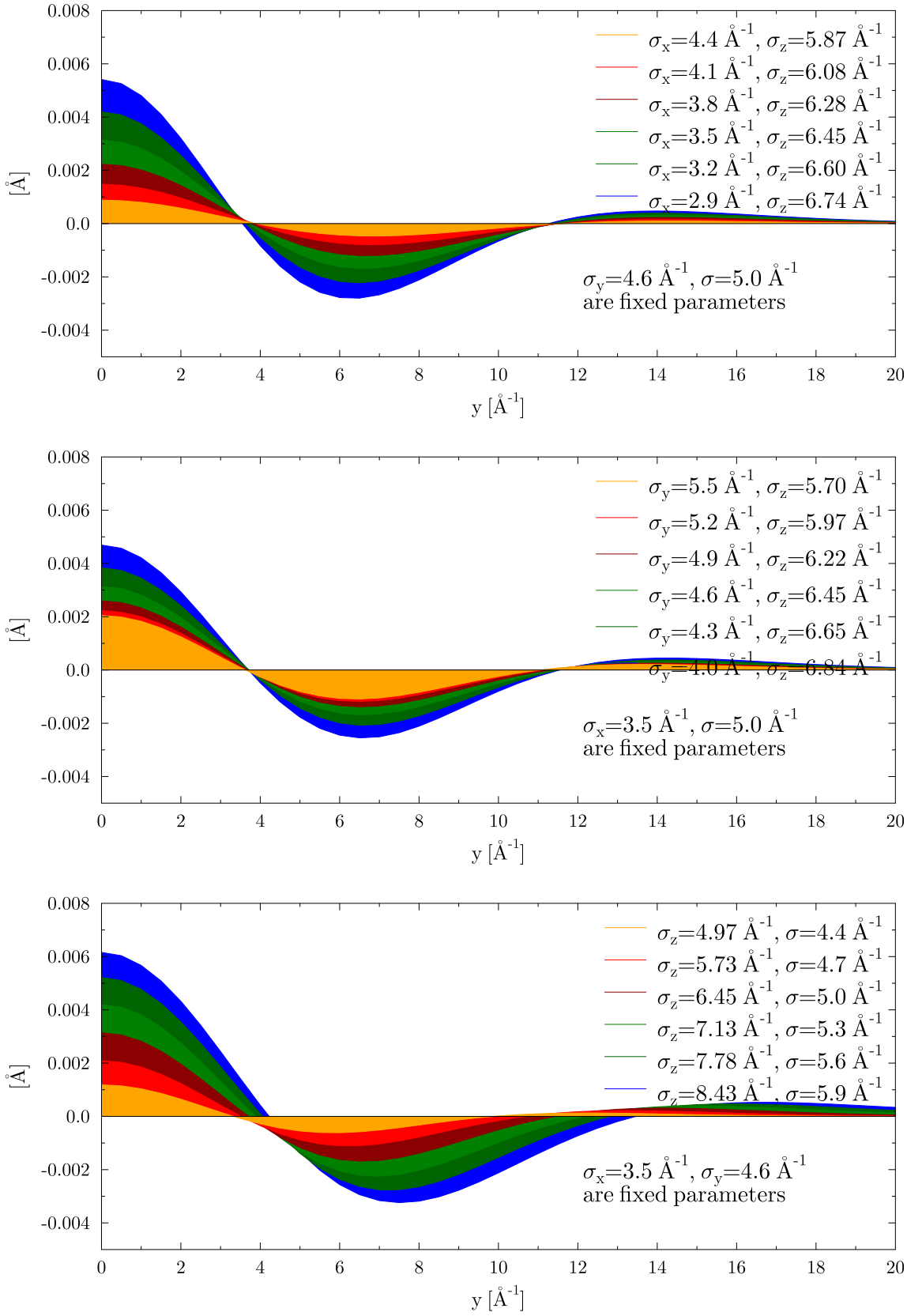

Figure 3.5: Differences between isotropic and multivariate NCPs.

i.e. a Gauss Hermite expansion or a multivariate Gaussian. Imposing that these 3 quantities are equal for the two models it is possible to fix the parameters of one knowing the parameters of the other, and in particular, have information on the anisotropy of the momentum distribution using a faster integration based on a Gauss-Hermite fit procedure.

The second moment for the Gauss-Hermite model has a contribution only from the pure Gaussian term, since all other terms have polynomials of degree ≥ 4,

$$M_2[J_A(y)] = \int_{-\infty}^{\infty} y^2 J_A(y) dy = \bar{\sigma}^2 \tag{3.55}$$

while for the multivariate Gaussian it gives the average contribution from the directional standard deviations

$$M_2[J_M(y)] = \int_{-\infty}^{\infty} y^2 J_M(y) dy = \frac{\sigma_x^2 + \sigma_y^2 + \sigma_z^2}{3}. \tag{3.56}$$

The equality between these two quantities yields the definition of the average value $\bar{\sigma}$ for the multivariate distribution

$$\bar{\sigma}^2 = \frac{\sigma_x^2 + \sigma_y^2 + \sigma_z^2}{3}. \tag{3.57}$$

The forth moment for Gauss-Hermite line shape gives as a result

$$M_4[J_A(y)] = \int_{-\infty}^{\infty} y^4 J_A(y) dy = 3(1 + c_4)\bar{\sigma}^4 \tag{3.58}$$

while for the anisotropic case we have

$$M_4[J_M(y)] = \int_{-\infty}^{\infty} y^4 J_M(y) dy = \frac{2\bar{\sigma}^4}{5} \left[\frac{\sigma_x^4 + \sigma_y^4 + \sigma_z^4}{\bar{\sigma}^4} + \frac{9}{2} \right] \tag{3.59}$$

and then, from the comparison of these two results we obtain

$$c_4 = \frac{2}{15} \left[\frac{\sigma_x^4 + \sigma_y^4 + \sigma_z^4}{\bar{\sigma}^4} - 3 \right] \tag{3.60}$$

that relates the first Hermite coefficient to the kurtosis of the multivariate Gaussian. Finally, from the comparison of the sixth moments for the two line shapes

$$M_6[J_A(y)] = \int_{-\infty}^{\infty} y^6 J_A(y) dy = 15\,(1 + 3c_4 + c_6)\,\bar{\sigma}^6 \tag{3.61}$$

and

$$M_6[J_M(y)] = \int_{-\infty}^{\infty} y^6 J_M(y) dy = \frac{12\bar{\sigma}^6}{7} \left[\frac{\sigma_x^6 + \sigma_y^6 + \sigma_z^6 - \sigma_x^2\sigma_y^2\sigma_z^2}{\bar{\sigma}^6} + \frac{27}{4} \right] \tag{3.62}$$

we can access the last condition defining the second Hermite coefficient as

$$c_6 = \frac{8}{315} \left[\frac{\sigma_x^6 + \sigma_y^6 + \sigma_z^6 + 6\sigma_x^2\sigma_y^2\sigma_z^2}{\bar{\sigma}^6} - 9 \right]. \tag{3.63}$$

Even if this procedure can make the anisotropic fit really fast, the highly non-linear combination of the σ_α as fit parameters leads to large correlations that are under study at this stage and that will be solved introducing *active parameters* that the fit procedure can easily access. Alternatively, one could look for the inverse relations giving the parameters of the multivariate knowing those of the anharmonic distribution, but in this way one is not sure that the resulting c_4 and c_6 parameters can correspond to a harmonic distribution.

In reference [45], Reiter *et al.*, propose a similar procedure for the analytic integration of a multivariate distribution with two equal variances, obtaining

$$\sigma^2 = \frac{2\sigma_x^2 + \sigma_z^2}{3} \qquad \text{and} \qquad c_{2n} = \left(\frac{\delta\sigma^2}{\bar{\sigma}^2}\right)^n \left\langle \left(\frac{1}{3} - \cos^2\theta\right)^n \right\rangle \tag{3.64}$$

with $\delta\sigma^2 = \sigma_x^2 - \sigma_z^2$. Explicitly,

$$c_4 = \frac{4}{45}\left(\frac{\delta\sigma^2}{\bar{\sigma}^2}\right)^2 \tag{3.65}$$

$$c_6 = \frac{16}{945}\left(\frac{\delta\sigma^2}{\bar{\sigma}^2}\right)^3 \tag{3.66}$$

that give the same result for the c_4 coefficient, wile the same result but with opposite sign for the c_6 coefficient, that can be explained redefining the quantity $\delta\sigma^2 = \sigma_x^2 - \sigma_z^2 \to \sigma_z^2 - \sigma_x^2$. In conclusion, the equations for a degenerate multivariate distribution proposed in the reference are here generalized to the case of three different variances.

In Figure 3.6 a graphical representation of the link equations is presented as the second (red) and third (orange) Hermite corrections to a Gaussian line-shape (green) in order to exactly reproduce an integrated multivariate NCP (blue).

3.4 The Vesuvio spectrometer

The NCS measurements we deal with in this work have been performed on the VESUVIO spectrometer [46, 47] at the ISIS Pulsed Neutron and Muon Source (Rutherford Appleton Laboratory, UK). VESUVIO operates in the IA regime where the incident neutron wavelengths in the range 30 $\text{Å}^{-1} \leq q \leq 200\text{Å}^{-1}$ are much less than interatomic spacings and thus atoms scatter incoherently, with scattered intensity being the sum of intensities from individual atoms in the sample. Also, the energy transfer, 1 eV $\leq \hbar\omega \leq$ 100 eV, largely exceeds binding molecular energies. It works in inverse-geometry mode, *i.e.*, detectors fix the scattered neutron final energy and evaluate the incident energy through a t.o.f. technique. The count rate as a function of the

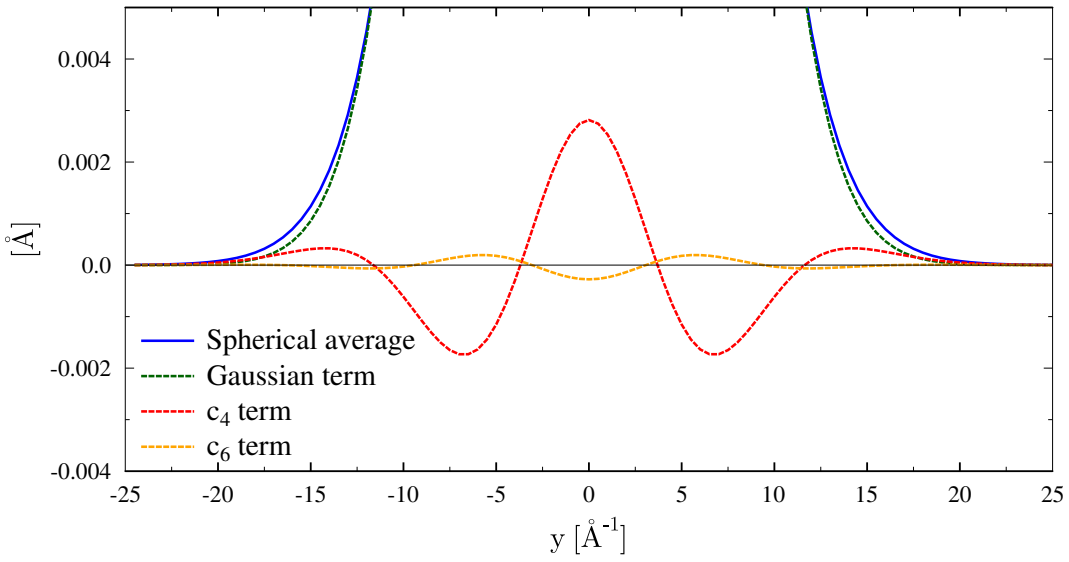

Figure 3.6: The second (red) and third (orange) Hermite corrections to a Gaussian line-shape (green) are reported. Their sum exactly reproduces the integrated multivariate NCP (blue) when the link equations are used.

t.o.f. t is defined as

$$C(t) = \sqrt{\frac{8E_0^3}{m_N L_0^2}}\, I(E_0) D(E_1) \left(\sum_M N_M \frac{d^2\sigma_M}{d\Omega dE_1} \right) d\Omega \tag{3.67}$$

where $I(E_0)dE_0$ is the number of incident neutrons s^{-1} with energies between E_0 and $E_0 + dE_0$, $D(E_1)$ is the probability that a neutron of energy E_1 is detected, m_N is the neutron mass, L_0 is the distance between the moderator and the sample, N_M is the number of atoms of mass M in the sample and $\frac{d^2\sigma_M}{d\Omega dE_1}$ is the double differential cross-section for mass M. Incoming neutrons are moderated by a water bath at T=295 K. The resulting energy spectrum shows a peak at about $E_0 = 300$ meV, and an epithermal tail of the form $E_0^{0.9}$.

Neutrons scattered in the forward direction are detected by Yttrium Aluminum Perovskite scintillators [48], located at a distance L_1, ranging between 0.5 m and 0.75 m from sample position, in the angular range 32.75^o to 72.5^o. In the backward direction scattered neutrons are detected by ^{6}Li scintillators, located at a distance ranging between 0.46 m and 0.67 m from sample position, in the angular range 130^o to 163^o. At each scattering angle the energy of the scattered neutrons E_1 is selected by using Au analyzer foils (E_1 =4897 meV). The instrument operates using the Foil Cycling (FC) technique, in forward scattering [49, 50], and the Double

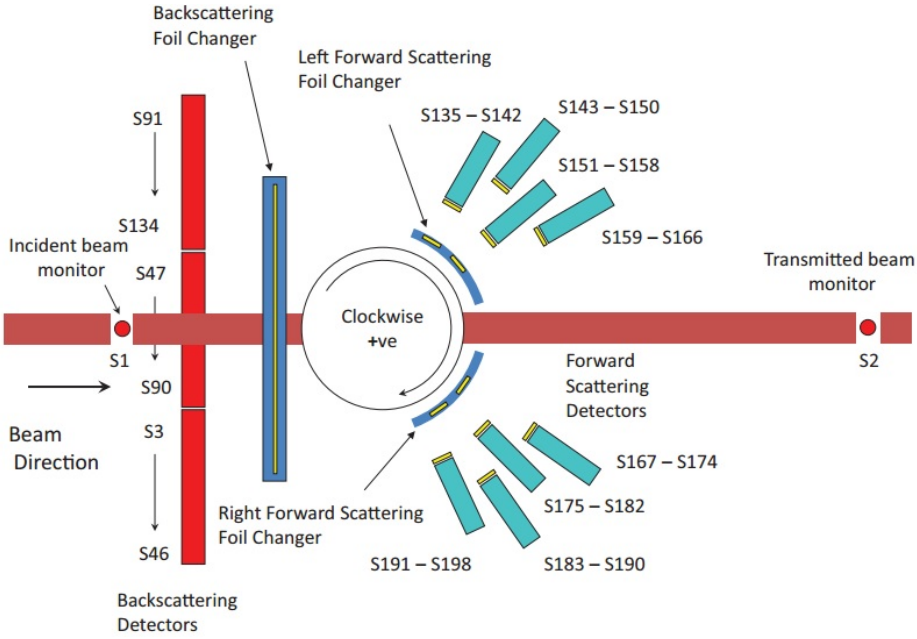

Figure 3.7: Schematics of the VESUVIO spectrometer at ISIS.

Difference (DD) technique [51], in backward scattering. A schematic picture of the instrument is presented in Figure 3.4.

The FC technique is used in order to increase the energy resolution. It is based on the alternation of presence and absence of a secondary gold foil in the secondary neutron path, between the sample and the detector. When the difference is taken between the two alternated measures, an improvement of about $1/\sqrt{2}$ on the resolution full-width-half-maximum is obtained, while the loss in statistics is only about 10%.

The DD technique for backward scattering detectors has the same goal as the FC but it is based on two independent measures done with resonant foils of the same material but with different thickness. When a linear combination of the two measures is taken, it is possible to reduce the principal contribution to the experimental width, the one coming from the width of the nuclear resonance for the gamma capture.

During an experiment, the double differential cross-section from Eq. (3.67) can be expressed as a function of the NCP

$$\frac{d^2\sigma_M}{d\Omega dE_1} = b^2 \left(\frac{E_1}{E_0}\right)^{1/2} \frac{M}{\hbar q} J(y). \tag{3.68}$$

Due to the finite q values in the scattering process, the NCP at each l detector retains the q dependence, expressed by the function $F(y,q)$. The latter includes a further broadening due to experimental resolution function, $R(y,q)$ The $F(y,q)$ function is related to the count rate via

the expression

$$F(y,q) = \frac{BM}{E_0\ I(E_0)} q\, C_l(t) \tag{3.69}$$

where B is a constant taking into account the detector solid angle, its efficiency at $E = E_1$, the time-energy Jacobian, the free-atom neutron cross section and the number of particles hit by the neutron beam. NCS data sets presented in the following Chapters have been y-scaled according to Eq. (3.69).

VESUVIO works as a mass-selecting spectrometer, since the position of the recoil peak depends on the mass of the struck nucleus. In Figure 3.4, simulations of t.o.f. spectra for forward (top) and backward (bottom) scattering detectors are reported for H, D, O and two experimental containers available at ISIS, a copper and a TiZr cells.

It is possible to define the mean value of the energy of the neutron when scattered by a nucleus of mass M. The general form of the result can be obtained imposing $y = 0$ yielding

$$E_i \left(1 - \frac{m_N}{M}\right) - E_f \left(1 + \frac{m_N}{M}\right) + 2\frac{m_N}{M}\sqrt{E_i E_f}\cos\theta = 0 \tag{3.70}$$

Solving the previous equation with respect to the initial energy, being the final fixed by a resonant foil, and introducing the parameter $X = M/m_N$ as the ratio of the nucleus to neutron mass, we find

$$E_i(y=0) = E_f \left(\frac{X+1}{\cos\theta + \left[X^2 - \sin^2\theta\right]^{\frac{1}{2}}} \right)^2 \tag{3.71}$$

that gives the simple result for H when $X \simeq 1$

$$E_i(y=0) = \frac{E_f}{\cos^2\theta} \qquad \text{for Hydrogen, } M \simeq m_N \tag{3.72}$$

The result is that the energy of the scattered neutron depends on the mass of the nucleus and on the angular position of the detector. In particular, the energy change is very large for light masses and backward scattering is forbidden for H single scattering. On the contrary, in the limit X $\to \infty$ there is no angular dependence for the incident energy that is also always equal to the final energy, giving elastic scattering.

The average position of a nucleus in a t.o.f. spectrum is given once the geometry of the instrument is known. If L_0 is the distance of the sample from the moderator, that the neutron exits at time 0, and L_1 is the distance from the sample to the detector, the time when a scattered neutron joins the detector is

$$t = \sqrt{\frac{m}{2E_i}} L_0 + \sqrt{\frac{m}{2E_f}} L_1 \tag{3.73}$$

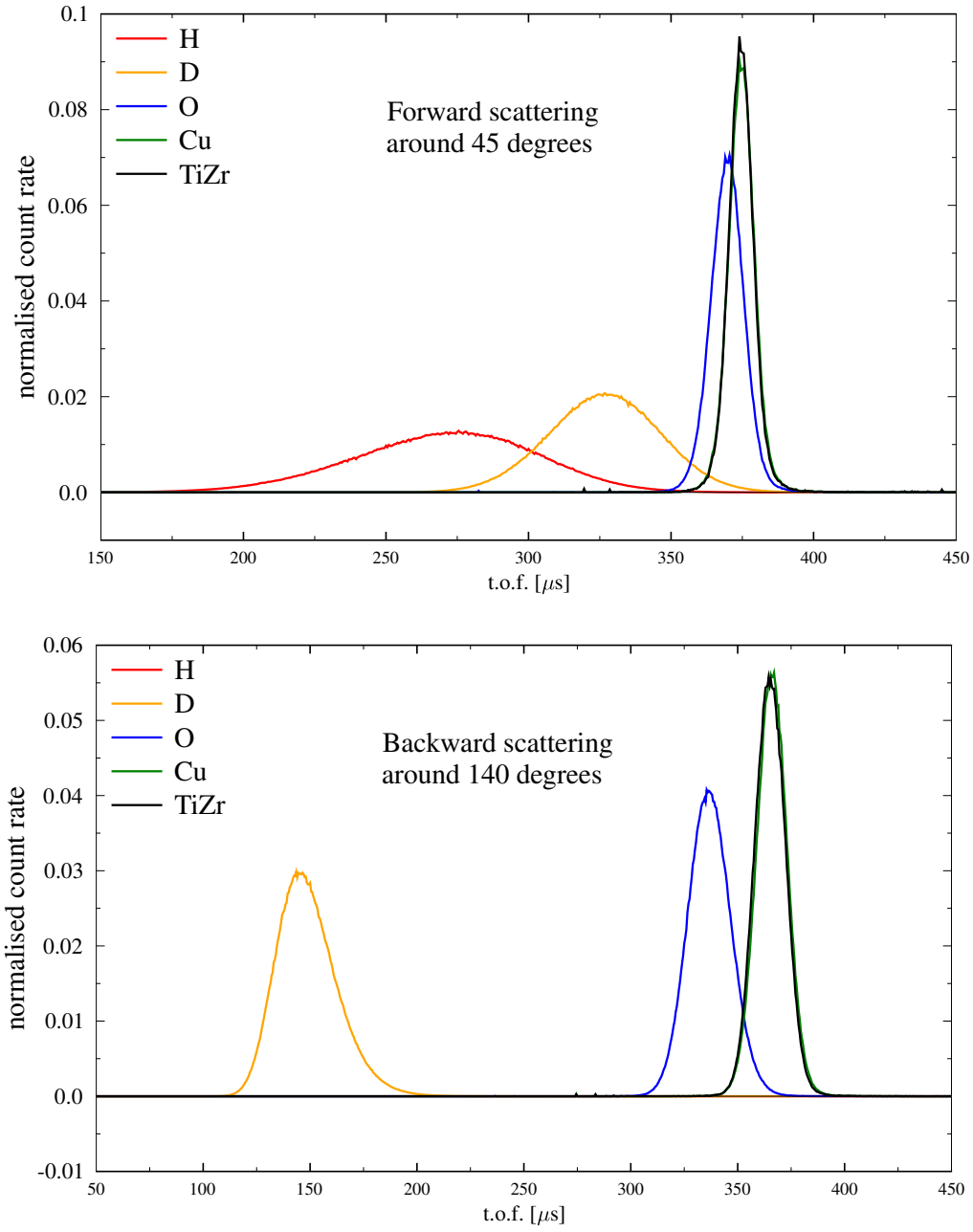

Figure 3.8: Simulations of t.o.f. spectra on VESUVIO for detectors in forward scattering (top) and backward scattering (bottom) for some typical masses.

The NCP corresponding to different masses will be centred at different times corresponding to $E_i(y=0)$, that means for H

$$t_H(y=0) = \sqrt{\frac{m}{2E_f}}\,(L_0\cos\theta + L_1) \qquad \text{for Hydrogen} \tag{3.74}$$

or in general

$$t_X(y=0) = \sqrt{\frac{m}{2E_f}}\left(L_0\frac{\cos\theta + \sqrt{X^2-\sin^2\theta}}{X+1} + L_1\right) \qquad \text{for } X>1 \tag{3.75}$$

It can be useful to interpret the factor $\sqrt{\frac{m}{2E_f}}$ as a time of 32.6 μs that a neutron takes in order to travel 1 meter at $E = E_f = 4897$ meV. This time is multiplied by an *effective distance* defined as the sum of final distance L_1 and the initial distance L_0 scaled by a kinematic factor depending on the mass M and the angular position of the detector . Moreover, there is a maximum t.o.f. corresponding to vanishing energy loss, i.e. to elastic scattering from a infinitely massive object, $t_\infty = t_{M\to\infty} = \sqrt{\frac{m}{2E_f}}(L_0+L_1)$.

Therefore, we can try to transform the t.o.f. spectra into spectra shifted with respect to this parameter and normalized to it, *i.e.*, changing variable from t to $z = (t_\infty - t)/t_\infty = 1 - t/t_\infty$, with the new variable changing in the range $0 < z < 1$. The mean position of an element in the new variable spectra is

$$z_H(y=0) = \frac{L_0}{L_0+L_1}\,(1-\cos\theta) \qquad \text{for Hydrogen} \tag{3.76}$$

and

$$z_X(y=0) = \frac{L_0}{L_0+L_1}\left(1 - \frac{\cos\theta + \sqrt{X^2-\sin^2\theta}}{X+1}\right) \qquad \text{for } X>1 \tag{3.77}$$

Examples of shifted spectra and a comparison with t.o.f. spectra is taken for experimental data on water in Figure 3.4. The spectra in the shift variable z, contrarily to those in t.o.f., have no dependence on the energy of the resonance foil and the dependence on the flight paths is reduced since the factor $(L_0+L_1)/L_1 \simeq 1$ for all the detectors. Therefore, this visualization method is undressed of all the geometry-dependence of the instrument, and can facilitate the reading of the physical information in the experimental data, with a particular benefit for the expanding community of non-physicists interested in the use of this spectrometer.

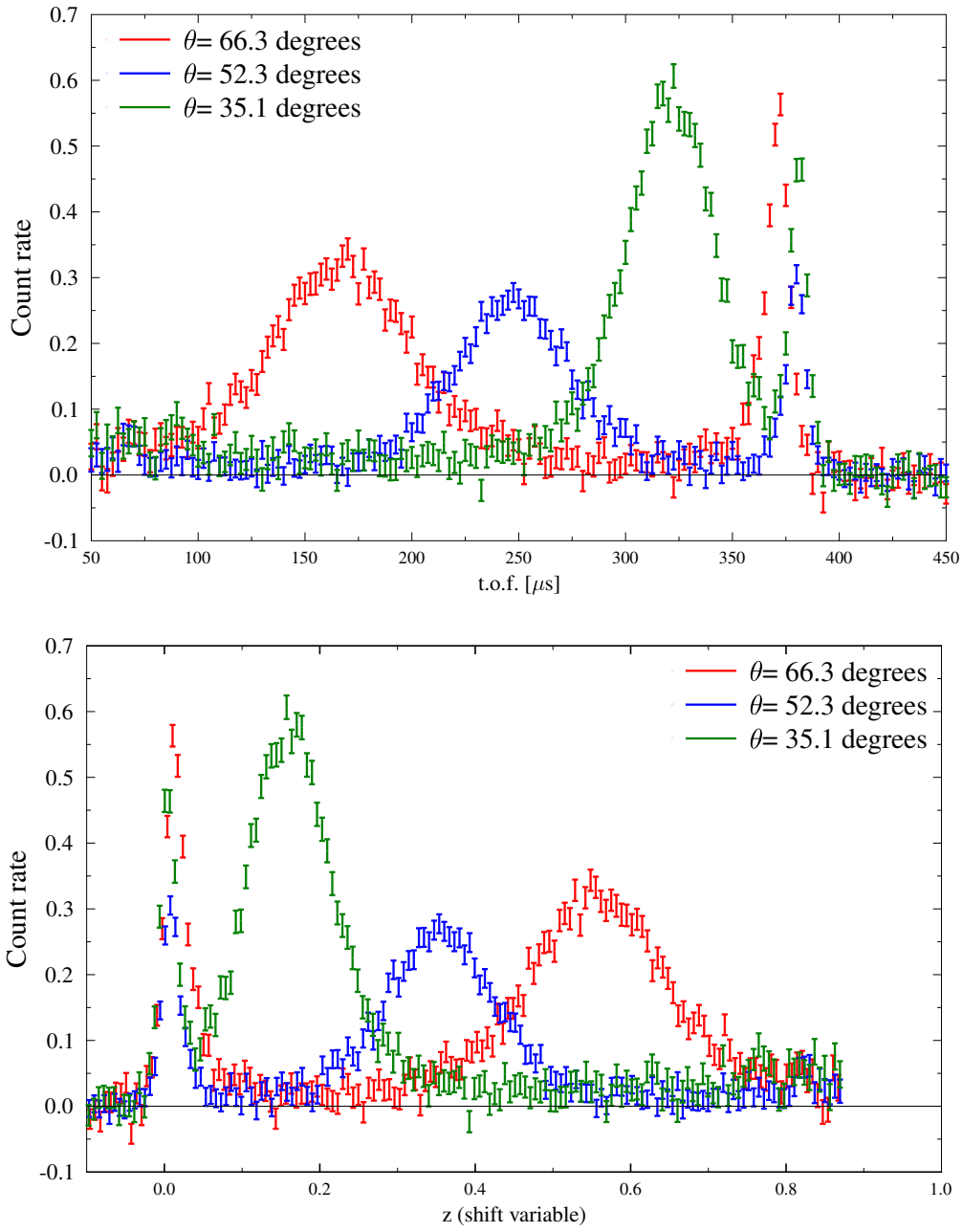

Figure 3.9: Experimental data for a water sample in the case of three detectors with different angular positions. In the top image the t.o.f. spectra as traditionally represented on VESUVIO, in the bottom image their transformation in the shift variable z quasi non dependent on the geometry of the instrument.

Chapter 4

Nuclear Kinetic Energies in a First-Order Quantum Harmonic Model

In this Chapter, I present a model that I developed for the evaluation of the parameters defining the amount of energy from each molecular vibration to the nuclear kinetic energies. Two force constants define the three internal modes and are fixed through the measured stretching and bending frequencies. The model can be applied to any triatomic XY_2 molecule in any phase and will be used in the following Chapters 5,6 and 7.

Water, as well as all triatomic non linear molecules, has 3×(number of atoms)−6 = 3 internal modes: two of them are symmetric vibrations, one stretching and one bending, and one is an antisymmetric stretching. This motions occur with variation of the inter nuclear distances and no displacement of the centre of mass. In addition, there are 6 external motions for the molecule as a rigid body: 3 translations and 3 rotations around the axes passing through the centre of mass. For an isolated molecule and no external interaction, the mean energies for the translational modes would be defined by the kinetic theory of the perfect gas as $k_B T/2$. The important action of the HBs hinders the translational and rotational modes to small vibrations of the molecule around mean positions in the water cluster. As a consequence, energies higher than the classical value define each translational mode, and there are no free rotations but librational modes.

In a first-order quantum model each s mode has a ZPE defined by its frequency ω_s. In addition, we impose the harmonic condition of i) full decoupling of the modes and ii) only quadratic terms for the nuclear potentials, as if the interaction were due to a spring of a given force constant. In principle, each atom can move when a vibration occurs, transforming a part of the energy enclosed in the vibration to its kinetic energy.

This is a single-molecule model, meaning that no external interaction is considered. Anyway, the effective action of the HBs is considered when the frequencies ω_s are experimentally measured, *e.g.*, the softening of the stretching force constant by the HB along the OH direction is enclosed in the experimental stretching frequency. Also, the very fact that frequencies are considered for the translational and librational modes is an effective introduction of the HB interaction.

Our goal is to define the parameters enabling to express the total mean kinetic energy for each atom as

$$\langle \mathcal{E}_K \rangle = \tau \sum_t^{\text{tra}} \frac{\hbar\omega_t}{4} \coth\left(\frac{\beta\hbar\omega_t}{2}\right) + \sum_r^{\text{lib}} \rho_r \frac{\hbar\omega_r}{4} \coth\left(\frac{\beta\hbar\omega_r}{2}\right) + \sum_v^{\text{vib}} f_v \frac{\hbar\omega_v}{4} \coth\left(\frac{\beta\hbar\omega_v}{2}\right). \quad (4.1)$$

4.1 Translation and rotation

We consider a symmetric triatomic molecule with two equal atoms of masses m and one atom of mass M and define the useful parameter $\mu = \frac{2m}{M}$.

The energy of the translation of the molecule of total mass $2m + M$ is divided amongst the nuclei through the two parameters

$$\tau_M = \frac{M}{2m+M} = \frac{1}{\mu+1} \qquad \tau_m = \frac{\mu}{2(\mu+1)}, \quad (4.2)$$

i.e., the ratio of each atom mass to the total mass. The fraction τ of translational energy of the centre of mass is the same for the three spatial directions, but in general different frequencies can be found in a vibrational spectrum relative to translations in different directions. Anyway, since the differences in these frequencies are often small compared to an experimental resolution, we consider an average frequency ω_t of the possible translational frequencies.

In Figure 4.1, the geometry of the molecule is presented. The two axes in the molecular plane are y and z and in their intersection lies the centre of mass of the molecule. The x axis is perpendicular to this plane and passes through the centre of mass as well. As a rigid body, the molecule can rotate around these axes and for each rotation a moment of inertia I can be geometrically defined. The parameter ρ defining the amount of kinetic energy that each nucleus

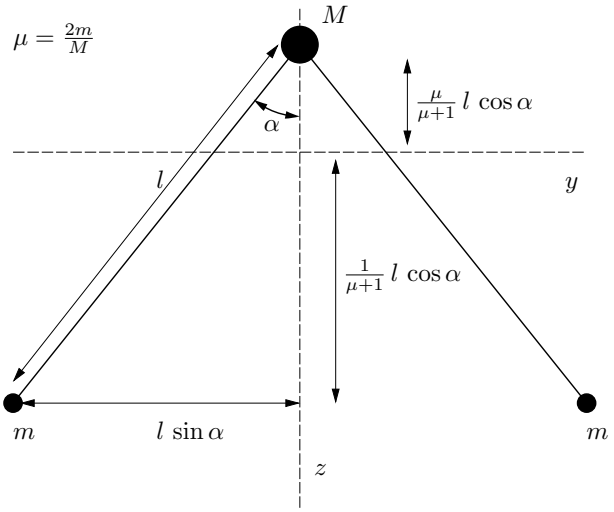

Figure 4.1: Geometry of the XY_2 molecule considered in the text.

receives form a librational vibration is defined by

$$3\rho = \rho_z + \rho_x + \rho_y = \frac{I_z}{I_z^{2m+M}} + \frac{I_x}{I_x^{2m+M}} + \frac{I_y}{I_y^{2m+M}}, \tag{4.3}$$

i.e., the sum over the three directions of the ratios of the nuclear moment of inertia around that axis to the total moment of inertia I^{2m+M} around the same axis. As a difference from the previous translational case, we have now three different fractions ρ_x, ρ_y and ρ_z with the same experimental problem of only an average librational frequency ω_ρ. For this reason, we have defined the average librational parameter ρ.

In particular, there is no angular motion of the mass M around the z axis, while the light atom moves at a distance $l\, \sin\alpha$, so that

$$I_z^M = 0 \qquad\qquad I_z^m = ml^2 \sin^2\alpha \tag{4.4}$$

Looking again at the Figure 4.1, the moments of inertia around the second molecular axis y are

$$I_y^M = M\left(\frac{\mu}{\mu+1}\right)^2 l^2 \cos^2\alpha \qquad\qquad I_y^m = m\left(\frac{1}{\mu+1}\right)^2 l^2 \cos^2\alpha. \tag{4.5}$$

Finally, for the rotation around the third axis x we have $I_x = I_z + I_y$. As a result, the parameters defining kinetic energies for the librational modes are

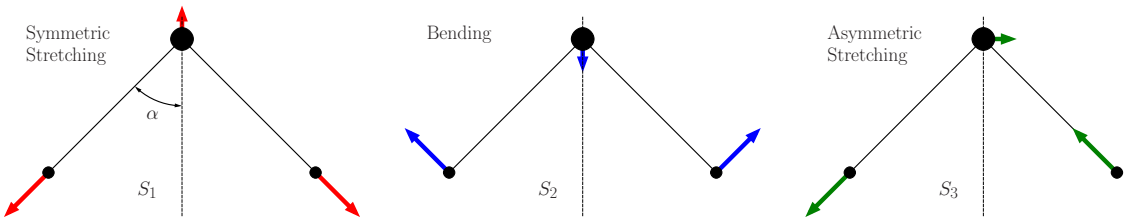

Figure 4.2: The three symmetry modes of vibration for a XY2 non linear molecule.

$$\rho_z^M = 0 \qquad \rho_z^m = \tfrac{1}{2}$$

$$\rho_y^M = \tfrac{\mu}{\mu+1} \qquad \rho_y^m = \tfrac{1}{2(\mu+1)} \tag{4.6}$$

$$\rho_x^M = \tfrac{\mu\cos^2\alpha}{(\mu+1)(1+\mu\sin^2\alpha)} \qquad \rho_x^m = \tfrac{(\mu+1)^2\sin^2\alpha+\cos^2\alpha}{2(\mu+1)(1+\mu\sin^2\alpha)}$$

Sum rules exist for these parameters. For example, given a mode s, the sum of twice the parameter for the atom m and the parameter for the atom M must be equal to 1, so that all the potential energy enclosed in the vibration is used to move the atoms and the energy conservation condition is fulfilled.

Finally, in the limit of infinite temperature, *i.e.*, k_BT largely higher than any binding energy of the molecule, each nucleus can be separated from the others and moves of simple translational motion with energy $3K_BT/2$. Indeed, in this limit one has

$$\frac{\hbar\omega_s}{4}\coth\left(\frac{\hbar\omega_s}{2K_BT}\right) \to \frac{K_BT}{2} \tag{4.7}$$

for each S, and then the sum of all the parameters for each atom must equal the number of degrees of freedom

$$3\tau + 3\rho + f_1 + f_2 + f_3 = 3 \qquad \text{as } T \to \infty. \tag{4.8}$$

4.2 Vibrations

For the sake of clarity, in the following sections we consider a light water molecule as an example of the application of the general treatment for any XY_2 molecule. For example, in the Chapter 6 we will apply the same procedure to the heavy water molecule.

We first define a harmonic potential affecting the three atoms. The force acting on each nucleus is due to the other two nuclei, and it is proportional to the displacement from the

mean distance and tends to bring back the nuclei to their mean position. Since these are the well-known features of the force due to an elastic spring, we use the classical result for the total potential energy of a system of three springs

$$U = q^T B_q q = \frac{k_{OH}}{2} q_1^2 + \frac{k_{OH}}{2} q_2^2 + \frac{k_{HH}}{2} q_3^2. \tag{4.9}$$

In particular, we introduced two equal springs with an elastic constant k_{OH} connecting the atoms H and H' to the atom O, and a spring with an elastic constant k_{HH} connecting H to H'. The vector $q = (q_1, q_2, q_3)$ has as components the moduli of the distances from O to H q_1, from O to H' q_2 and from H to H' q_3. These are the so called internal coordinates and B_q is the potential energy matrix in the base of the internal coordinates. The matrix B_q is diagonal and its elements are proportional to the force constants. The internal coordinates are related to the Cartesian coordinates through the transformation $q = Qx$, with the matrix Q given by

$$Q = \begin{pmatrix} 0 & 0 & -\sin\alpha & -\cos\alpha & \sin\alpha & \cos\alpha \\ \sin\alpha & -\cos\alpha & 0 & 0 & -\sin\alpha & \cos\alpha \\ -1 & 0 & 1 & 0 & 0 & 0 \end{pmatrix} \tag{4.10}$$

and $x = (y_H, z_H, y_{H'}, z_{H'}, y_O, z_O)$ the vector of the Cartesian coordinates, that is the nuclear displacements from the mean position along two molecular axes. The definition of the two axes is given in Figure 4.1. Cartesian coordinates are the best way to express the kinetic energy. Indeed, in the basis the kinetic energy matrix A_x is diagonal and its elements are proportional to the individual masses of the system

$$E = \dot{x}^T A_x \dot{x} = \frac{m}{2}(\dot{x}_H^2 + \dot{y}_H^2 + \dot{x}_{H'}^2 + \dot{y}_{H'}^2) + \frac{M}{2}(\dot{x}_O^2 + \dot{y}_O^2). \tag{4.11}$$

The kinetic and potential matrices A_x and B_q are expressed in two different bases. We find useful to transform them into a third basis composed of the so-called symmetry-adapted coordinates $S = (S_1, S_2, S_3)$. The symmetry coordinates are not unequivocally defined, being our definition depicted in Figure 4.2. The symmetry coordinates should reproduce the molecular normal modes introduced in the Chapter 2 and belong to a given symmetry group. In particular, for the water molecule and for any non-linear XY_2 molecule there are two symmetric modes and one anti-symmetric mode. The former are a stretching and a bending while the latter is a stretching as well. It is possible to transform the vector x into the vector S through the

transformation $x = \Sigma S$, with the matrix

$$\Sigma = \begin{pmatrix} -\sin\alpha & -\cos\alpha & -\sin\alpha \\ -\cos\alpha & \sin\alpha & -\cos\alpha \\ \sin\alpha & \cos\alpha & -\sin\alpha \\ -\sin\alpha & \cos\alpha & \sin\alpha \\ 0 & 0 & \mu\cos\alpha \\ \mu\cos\alpha & -\mu\sin\alpha & 0 \end{pmatrix}. \tag{4.12}$$

The matrix Σ enables the definition of the kinetic energy matrix in the symmetry-adapted basis A_S, in particular

$$E = \dot{x}^T A_x \dot{x} = \dot{S}^T \left(\Sigma^T A_x \Sigma\right) \dot{S} = \dot{S}^T A_S \dot{S}, \tag{4.13}$$

obtaining as an expression for A_S

$$A_S = m \begin{pmatrix} 1+\mu\cos^2\alpha & -\mu\cos\alpha\sin\alpha & 0 \\ -\mu\cos\alpha\sin\alpha & 1+\mu\sin^2\alpha & 0 \\ 0 & 0 & 1+\mu\cos^2\alpha \end{pmatrix}. \tag{4.14}$$

In the case of the potential energy matrix, two coordinate transformations are required, the first one is $q \to x$ and the second one is $x \to S$, obtaining

$$U = q^T B_q q = S^T \left(\Sigma^T Q^T B_q Q \Sigma\right) S = S^T B_S S, \tag{4.15}$$

obtaining the potential energy matrix in the base of the symmetry-adapted coordinates B_S whose components are

$$\begin{pmatrix} k_{OH}(1+\mu\cos^2\alpha) + 2k_{HH}\sin^2\alpha & \left[2k_{HH} - k_{OH}\mu(1+\mu\cos^2\alpha)\right]\frac{\sin 2\alpha}{2} & 0 \\ \left[2k_{HH} - k_{OH}\mu(1+\mu\cos^2\alpha)\right]\frac{\sin 2\alpha}{2} & (2k_{HH} + k_{OH}\mu^2\sin^2\alpha)\cos^2\alpha & 0 \\ 0 & 0 & k_{OH}(1+\mu\cos^2\alpha)^2 \end{pmatrix}. \tag{4.16}$$

4.2.1 Eigenvalues and free parameters

The matrices A_S and B_S are now expressed in the same base and they can be used in order to write the secular equation describing the system

$$|B - \lambda A| = \left[(b_{11} - \lambda a_{11})(b_{22} - \lambda a_{22}) - (b_{12} - \lambda a_{12})^2\right](b_{33} - \lambda a_{33}) = 0. \tag{4.17}$$

Here $\lambda = \omega^2$ is one of the three eigenvalues of the system proportional to the square of the frequency of the relative vibrational mode. The secular equation is such that the symmetric

and anti-symmetric components are not mixed. Both the kinetic and potential energy matrices are indeed block matrices $(2 \times 2) \otimes (1 \times 1)$.

We point out that we can experimentally access the eigenvalues through the measure of a vibrational spectrum. Hence, the secular equation will be used to define the unknown force constants. For example, the k_{OH} parameter is easily defined through the anti-symmetric part of the secular equation, leading to the result

$$k_{OH} = \frac{m\lambda_3(1 + \mu\cos^2\alpha)}{(1 + \mu\sin\alpha\cos\alpha)^2}. \tag{4.18}$$

For water vapour, the asymmetric stretching frequency is $\nu_3 = 3738$ cm^{-1} and the angle $2\alpha = 108.4$ degrees, giving as a result a value for the force constant $k_{OH} = 7.66 \times 10^2$ kg/m. It is interesting to point out the weak dependence of the force constant on the molecular angle. Indeed, for a rectangular water molecule with $2\alpha = 90$ degrees the force constant would be $k_{OH} = 7.76 \times 10^2$ kg/m, while for a linear molecule with $2\alpha = 120$ degrees the parameter would be $k_{OH} = 7.65 \times 10^2$ kg/m changing for less then 2%.

The symmetric part of the secular equation

$$D(\lambda) = \frac{1+\mu}{4}\left[8k_{OH}k_{HH}(1+\mu)\cos^2\alpha - M\lambda\mu(4k_{HH} + 2k_{OH}(1+\mu\cos^2\alpha) - M\lambda\mu)\right] \tag{4.19}$$

defines the second free parameter k_{HH} of the model

$$k_{HH} = \frac{M\lambda_2\mu\left[2k_{OH}(1+\mu\cos^2\alpha) - M\lambda_2\mu\right]}{4\left[2k_{OH}(1+\mu)\cos^2\alpha - M\lambda_2\mu\right]} \tag{4.20}$$

In principle, it is not clear which frequency should be used in this case between ω_1 and ω_2, both corresponding to a symmetric vibration. The fact that the number of physically-observable frequencies (ω_1, ω_2 and ω_3) exceed by one the number of free parameters (k_{OH} and k_{HH}) gives the possibility to test the accuracy of the model. Indeed, after that two frequencies are used to fix the parameters it is possible to evaluate the third frequency within the model and compare that value with the measured one. This is done in Table 4.1, where we try to fix k_{HH} the first time using ω_2 and reporting the evaluated ω_1 and then fixing k_{HH} using ω_1 and then evaluating ω_2. As one can see, while in the former case the discrepancy between the evaluation and the measure of ω_1 is of about the 20%, in the latter case a negative eigenvalue leading to an imaginary non-physical frequency is found.

In the literature, examples of models with more than 2 force constants can be found, for example in Ref. [52,53]. Anyway, we decided not to follow this example since, even if one could expect to improve the accuracy of the model introducing more free parameters, no possible test

	solid	liquid	vapour
2α [degrees]	108.4	105.5	104.3
ν_1 [cm^{-1}]	3085	3289	3686
ν_2 [cm^{-1}]	1650	1645	1596
ν_3 [cm^{-1}]	3220	3490	3738
k_{OH} [10^2 kg/m]	5.684	6.684	7.673
$k_{HH}(\nu_2)$ [10^2 kg/m]	5.957	3.713	2.807
evaluated ν_1 [cm^{-1}]	5245	4661	4536
$k_{HH}(\nu_1)$ [10^2 kg/m]	-0.25	-0.53	-0.01
evaluated ν_2 [cm^{-1}]	581i	885i	143i

Table 4.1: The parameters and the corresponding results for the force constants in the case of light water in its three stable phases. $k_{HH}(\nu)$ is the parameter fixed using the frequency ν, while the corresponding evaluated frequency is the estimate of the only frequency that has not been used to fix the force constants.

on physical observables can be done such as the one now discussed. In order to understand why the accuracy of the model is of the 20%, I tried the same evaluations on a number of triatomic XY_2 molecules reporting the results in the Table 4.2. Interestingly, for 6 of the considered molecules over a total of 8, the accuracy is more or less the same and no dependence on μ is shown.

Then, we decide to use ω_2 to define k_{HH}. The angular dependence of both k_{OH} and k_{HH} for the ice Ih, liquid and gas phases of water are reported in Figure 4.3.

4.2.2 Eigenvectors and energy fraction

Once that the free parameters are fixed, it is possible to go back to the secular equation and evaluate the eigenvector in the symmetry base for each internal vibration

$$(B_S - \lambda A_S)\, S = 0. \tag{4.21}$$

Due to the block structure of the matrices, one eigenvector $\mathcal{A} = (0, 0, 1)$ corresponds to the antisymmetric stretching and two eigenvectors of the form $\mathcal{S} = (1, v(\lambda), 0)$ are related to the symmetric vibrations. The parameter

$$v(\lambda) = \frac{\left(2k_{OH}\mu(1 + \mu\cos^2\alpha) - 4k_{HH} - M\lambda\mu^2\right)\sin(2\alpha)}{8k_{HH}\cos^2\alpha + k_{OH}\mu^2\sin^2(2\alpha) - 2M\lambda\mu(1 + \mu\sin^2\alpha)} \tag{4.22}$$

Molecule	ν_2 [cm^{-1}]	ν_3 [cm^{-1}]	2α [deg]	μ	ν_1 [cm−1]	evaluated ν_1 [cm^{-1}]	error
H_2O	1594	3756	104.3	0.12	3654	4536	21%
D_2O	1178	2788	104.5	0.25	2666	3269	20%
F_2O	461	831	103.0	2.37	928	1285	32%
H_2S	1183	2626	92.1	0.06	2615	3046	15%
D_2S	855	1999	92.0	0.12	1896	2250	17%
H_2Se	1034	2358	91.0	0.03	2344	2719	15%
Cl_2O	296	686	110.9	4.37	639	593	07%
SO_2	518	1362	120	1.	1151	1474	25%

Table 4.2: The accuracy of the present model tested on a number of triatomic XY_2 molecules. The relative error is defined as the difference of the experimental and evaluated frequencies divided by their average.

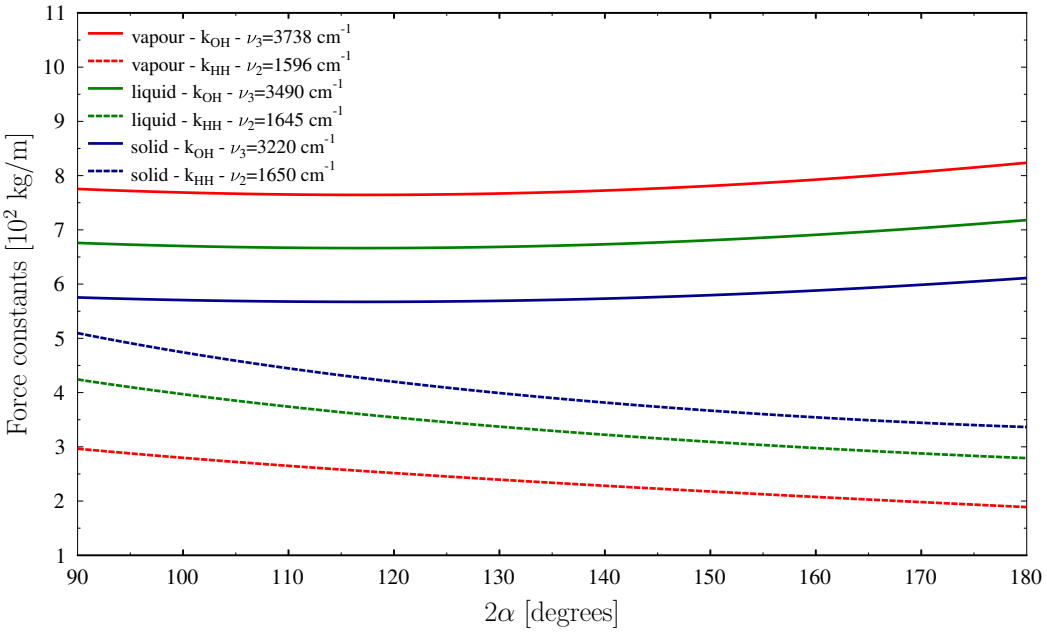

Figure 4.3: Angular dependence for the force constants when the experimental frequencies for vapour, liquid and solid water are considered.

has the two limiting cases $v(\lambda) \ll 1$ for $\lambda \to \lambda_1$ and $v(\lambda) \gg 1$ for $\lambda \to \lambda_2$. When these vectors are evaluated, the corresponding vectors in the Cartesian space can be defined through the transformation Σ. In particular, $x_{\mathcal{A}} = \Sigma\mathcal{A}$ and $x_{\mathcal{S}}(\lambda) = \Sigma\mathcal{S}$. Due to the symmetry of each vibration, there are some conditions on the components of the vectors $x_{\mathcal{S}}$ and $x_{\mathcal{A}}$. In particular,

$$\text{Symmetric vibration} \begin{cases} y_H &= -y_{H'} \\ z_H &= z_{H'} \\ y_O &= 0 \\ z_O &= -\mu z_H \end{cases} \tag{4.23}$$

and

$$\text{Antisymmetric vibration} \begin{cases} y_H &= y_{H'} \\ z_H &= -z_{H'} \\ y_O &= -\mu z_H \\ y_O &= 0 \end{cases} \tag{4.24}$$

In both cases, two parameters such as x_H and y_H are enough to define the other four parameters and the first two equations in the system $x = \Sigma S$ are sufficient to define the Cartesian vectors. When this is done and all the Cartesian displacement are known, it is possible to evaluate the fraction of kinetic energy of each atom when one of the three vibrations takes place. As already mentioned at the beginning of the Chapter, the mean kinetic energy for one of the three nuclei, *e.g.*, the H, is $m(\dot{y}_H^2 + \dot{z}_H^2)$ and in a harmonic motion this is proportional to $m(y_H^2 + z_H^2)$, with the frequency ω the proportional constant. Hence, the ratio of the nuclear kinetic energy to the total kinetic energy can be expressed as

$$f_{m,\lambda} = \frac{\mu(\dot{x}_1^2 + \dot{y}_1^2)}{2\left(\mu(\dot{x}_1^2 + \dot{x}_2^2) + \dot{x}_3^2 + \dot{y}_3^2\right)} \tag{4.25}$$

for the atom of mass m, while for the atom of mass M one has the similar result

$$f_{M,\lambda} = \frac{\dot{x}_3^2 + \dot{y}_3^2}{\mu(\dot{x}_1^2 + \dot{x}_2^2) + \dot{x}_3^2 + \dot{y}_3^2}. \tag{4.26}$$

These are the fractions of the total kinetic energy that each atom takes from an internal vibration. In the Table 4.3, these parameters in the case of the internal vibrations of a water molecule in the case of the ice Ih, liquid and vapour phases are reported

Ice Ih H_2O	f_1	f_2	f_3
H	0.480	0.446	0.479
O	0.039	0.107	0.041
Liquid H_2O	f_1	f_2	f_3
H	0.500	0.450	0.478
O	0.000	0.100	0.044
Vapour H_2O	f_1	f_2	f_3
H	0.496	0.453	0.477
O	0.008	0.093	0.045

Table 4.3: The kinetic energy fractions relative to the internal vibrations of a water molecule in the case of the ice Ih, liquid and vapour phases evaluated within the present model.

Chapter 5

The Melting of Light Water

I have analysed new INS experiments and re-analysed some published NCS measurements using anisotropic momentum distributions. The INS results are used to build the kinetic energy contributions through our harmonic model described in Chapter 4 and compared with the observed contributions of the multivariate Compton profiles. From the comparison, conclusions on the anharmonic contributions to the hydrogen dynamics are drawn.

5.1 Looking for anharmonicity

A detailed description of the structure and dynamics of the HB network in water is essential to reach a thorough understanding of the unique properties of this liquid, necessary both for the evolution of life and its continuance. Water properties are brought about by the hydrogen bonded environment, in a picture where each molecule is involved in about four HBs with strengths considerably less than covalent bonds but considerably greater than the natural thermal energy. Evidence of the particular uniqueness of liquid water are in its many physical and chemical properties which occur for instance when low density structuring naturally occurs at low and supercooled temperatures.

The dynamics of the proton that participates in hydrogen bonding is a subject of great interest and the quantum effects associated with protons have a significant impact on the behavior of HB networks. Quantum effects influence the vibrational dynamics probed in INS, *i.e.*, the protons participating in HBs, as well as the static properties of ice and water, with the quantum behaviour originating from zero-point motion. It has been recently suggested that a detailed description of the strength of the HB is a prerequisite to elucidate the influence of quantum

nuclear effects on the hydrogen bonding [8]. The picture proposed is that this effect arises from a competition between anharmonic quantum fluctuations of intermolecular bond bending and intramolecular covalent bond stretching, where the latter fluctuations tend to strengthen HBs whereas the former to weaken them.

Quantum effects, such as those associated with the breaking and distortion of HBs are uniquely revealed by measuring the proton momentum distributions, $n(p)$, and mean kinetic energy, $\langle E_K \rangle$, using NCS [40, 46, 54] and by computer simulations using open Path Integral Molecular Dynamics (PIMD) [55, 56]. Indeed in recent years several NCS and PIMD studies have been devoted to study these both physical quantities in ice and water in a wide temperature range 269 K $< T <$ 673 K [14,27,40,56–67]. The knowledge of the $n(p)$ provides a unique insight of the effective potential the proton experiences in its local environment [40].

The dynamic structure factor $S(\mathbf{q}, \omega)$ accessed through INS is directly related to the density of vibrational states $g(E)$ weighted by the squared amplitudes of the atomic oscillations [68–70].

Values of proton mean kinetic energy and momentum distributions can also be calculated using empirical models [52]. In this case, the frequencies of a set of quantum harmonic oscillators are derived from optical data and hydrogen-projected vibrational neutron spectra, under the assumptions of decoupling amongst internal and external modes. This procedure has been already employed in solid and liquid H_2S [71] and in SCW [72].

Sample	T	ω_x	ω_y	ω_z	$\langle E_K \rangle_x$	$\langle E_K \rangle_y$	$\langle E_K \rangle_z$	$\langle E_K \rangle$
	[K]	[meV]	[meV]	[meV]	[meV]	[meV]	[meV]	[meV]
Ice	271	114±10	152±13	347±11	28.9±2	38.1±3	86.7±3	153.7±2
Water	285	63± 9	207±17	335±10	18.3±2	51.8±4	83.8±2	153.9±3
	673	69±13	193±20	368±17	32.3±4	51.8±5	92.5±4	176.6±4
(Ref [65])	673							178.0±4
(Ref [57])	673							178.0 ± 11

Table 5.1: Total kinetic energy $\langle E_K \rangle$ and its three directional contributions, $\langle E_K \rangle_\alpha$ from the NCS data. The three effective frequencies, $\hbar\omega_\alpha$ are defined through Eq. 5.1. The last two values for the $\langle E_K \rangle$ were obtained in Refs. [57, 65] through the fit of a Gauss - Hermite NCP.

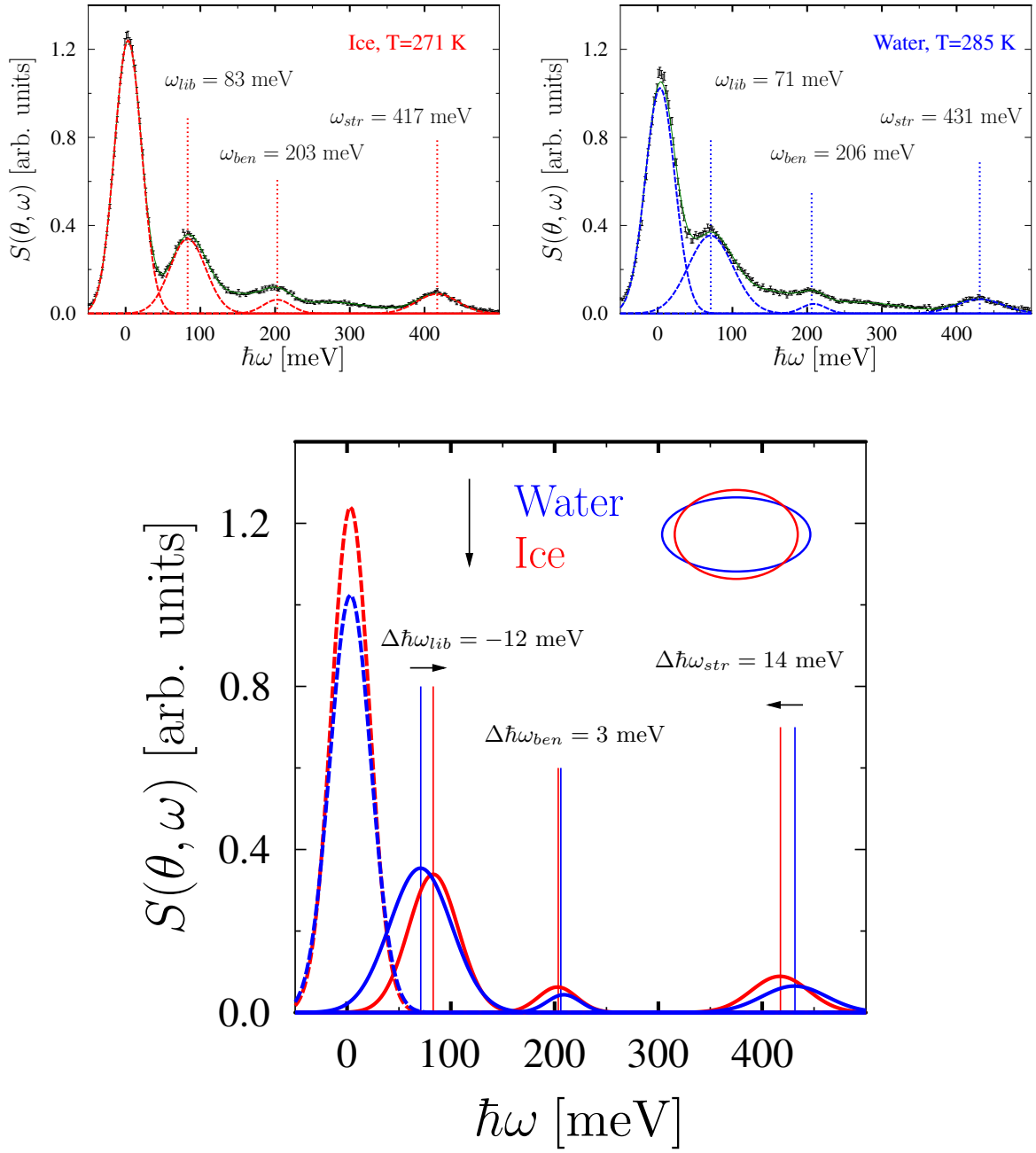

Figure 5.1: Top. A slice of the dynamical structure factors from INS experiments as seen from a detector bank at $\theta = 20$ degrees, for ice *I*h at T = 271 K (left) and water at T = 285 K (right). Experimental data are reported as black points while the total fit is reported as green line. Individual Gaussian contributions to the fit, together with their central values, are reported as red lines for ice and blue lines for water. Bottom. The same individual fits as above, but superposed in order to highlight the red- and blue-shifts in the phase transition from water to ice.

5.2 INS and NCS experiments and data analysis

Recent NCS experiments have been performed on the VESUVIO spectrometer on ice *I*h at T = 271 K [63], water at T = 285 K [27] and T = 673 K [65]. The corresponding data have been fitted anew, using the angular average of the multivariate Gaussian distribution (Eq. 3.21). The new analysis of these data was motivated by the update of the fitting routines according to the discussion in Chapter 3. The variances σ_α^2, the corresponding directional contributions $\langle E_K \rangle_\alpha$, the total mean kinetic energy $\langle E_K \rangle$ are reported in Table 5.1. In the same Table, the values of the frequencies $\hbar\omega_\alpha$, defined through

$$\frac{\hbar^2 \sigma_\alpha^2}{2M} = \langle E_K \rangle_\alpha = \frac{\hbar\omega_\alpha}{4} \coth\left(\frac{\hbar\omega_\alpha}{2k_B T}\right) \tag{5.1}$$

are also reported. A comparison is made reporting the values for two other measurements at T = 673 K of Refs. [57, 65], where the results for the kinetic energy were obtained through the isotropic-anharmonic momentum distribution of Eq. 3.14.

In addition to the NCS measurements, INS experiments have been performed on the SEQUOIA spectrometer on ice *I*h at T = 271 K and water at T = 285 K [17] using an incident neutron energy E_i= 600 meV. In Figure 5.1, a *slice* of the dynamic structure factor $S(\mathbf{q}, \omega)$ measured through INS by a detector in the angular position θ = 20 degrees is reported (top). The data correspond to ice (left panel) and water at T = 285 K (right panel).

In Ref. [17], the $S(\mathbf{q}, \omega)$ was reduced in order to obtain the H-projected density of states $g(E)$ through a procedure that will be discussed in Chapter 7. From the stretching component, one can derive the stretching contribution to the H mean kinetic energy

$$\langle E_K \rangle_{str} = \frac{3}{4} \int_{E_m}^{E_M} g(E)_{str}\, E\, dE \tag{5.2}$$

with E_m and E_M the minimum and maximum values defining the stretching region. In principle, for a one-phonon density of states the E_m value should lie where the minimum between bending and stretching components can be found, while the value for E_M can go up to infinity. In order to maximize the signal-to-noise ratio, we set the two values to 355 meV and 480 meV respectively. Values for $\langle E_K \rangle_{str}$ in the case of ice and water from Eq. (5.2) are reported in Table 5.2. For water at T = 673 K, the value of $\langle E_K \rangle_{str}$ has been derived using the $g(E)_{str}$ line shape from Figure 4 of Ref [73]. The corresponding value $\langle E_K \rangle_{str}$ = 115± 5 meV is reported in the same Table.

Within the assumption of decoupled quantum librational and vibrational harmonic oscillations, the main peaks in the experimental $S(\mathbf{q}, \omega)$ are fitted with Gaussian line-shapes. Frequen-

cies are derived for librational, bending and stretching modes, namely ω_{lib}, ω_{ben} and ω_{str}. These fits are reported in Figure 5.1 (top) over the aforementioned experimental data. In the same Figure, the individual Gaussian line-shapes are reported as well, together with vertical lines defining their central values. A broad Gaussian contribution is found around 300 meV, where an overtone is expected for the combination of libtation and bending modes. In the lower panel, the fitted contribution for ice and water at T = 285 K are superposed, in order to highlight the red-shift of the stretching and bending bands, *i.e.*, $\Delta\hbar\omega_{str} = 12$ meV and $\Delta\hbar\omega_{ben} = 3$ meV, and the blue-shift of the librational band, *i.e.*, $\Delta\hbar\omega_{lib} = 12$ meV. The values of these frequencies can be rearranged in order to define three molecular frequencies, ω_α, according to [63, 64]:

$$\begin{aligned} \omega_x &= \omega_{lib} \\ \omega_y &= \tfrac{1}{2}\left(\omega_{lib} + \omega_{ben}\right) \\ \omega_z &= \omega_{str} \end{aligned} \tag{5.3}$$

The values of ω_α for ice and water at T = 285 K, together with the value of $\langle E_K \rangle_z$ derived from ω_z using Eq. 5.1, are reported in Table 5.2. In the case of water at T = 673 K, the values of ω_α listed in the Table 5.2 are obtained from the Raman spectroscopic data of Ref. [73], and for the librational mode, a simple average of the three librational frequencies has been considered. This procedure yields quantities directly comparable to those obtained from the NCS data, but independently derived from INS.

T			$\hbar\omega_x$	$\hbar\omega_y$	$\hbar\omega_z$	$\langle E_K \rangle_z$	$\langle E_K \rangle_{str}$
[K]			[meV]	[meV]	[meV]	[meV]	[meV]
Ice	271	INS	83 ± 2	143 ± 5	417 ± 5	104 ± 1.2	98 ± 4
Water	285	INS	72 ± 3	139 ± 8	429 ± 6	107 ± 1.5	100 ± 4
	673	Raman	59	130	445	113	115 ± 5

Table 5.2: Values of $\hbar\omega_\alpha$ obtained applying Eq. 5.3 to the librational, bending and stretching frequencies obtained from the INS data. The component $\langle E_K \rangle_z$ corresponding to the frequency $\hbar\omega_z$ is obtained using Eq. 5.4, while the values for $\langle E_K \rangle_{str}$ are from Ref. [17] and [73] (see text).

It must be noticed that a linear combination of frequencies, such as the one proposed in Eq. 5.3, is only possible in the limit of infinite mass for the oxygen atom, and in the limit of $\hbar\omega_i >> 2k_BT$, where $i = lib, ben$ and str. An evolution of this procedure is represented by the harmonic model of Chapter 4, here applied to the INS observed frequencies in order to define a

set of kinetic energies $\langle \mathcal{E}_K \rangle_\alpha$. In particular,

$$\begin{aligned}
\langle \mathcal{E}_K \rangle_x &= \rho \tfrac{\hbar\omega_{lib}}{4} \coth\left(\tfrac{\hbar\omega_{lib}}{2k_BT}\right) + \tau \tfrac{1}{2} k_B T \\
\langle \mathcal{E}_K \rangle_y &= \rho \tfrac{\hbar\omega_{lib}}{4} \coth\left(\tfrac{\hbar\omega_{lib}}{2k_BT}\right) + f_2 \tfrac{\hbar\omega_{ben}}{4} \coth\left(\tfrac{\hbar\omega_{ben}}{2k_BT}\right) + \tau \tfrac{1}{2} k_B T \\
\langle \mathcal{E}_K \rangle_z &= (f_1 + f_3) \tfrac{\hbar\omega_{str}}{4} \coth\left(\tfrac{\hbar\omega_{str}}{2k_BT}\right) + \tau \tfrac{1}{2} k_B T
\end{aligned} \tag{5.4}$$

The calculated values for $\langle \mathcal{E}_K \rangle_\alpha$ and the total mean kinetic energy $\langle \mathcal{E}_K \rangle$ are reported in Table 5.3, together with the corresponding values of $\langle E_K \rangle_\alpha$ and $\langle E_K \rangle$ from NCS.

5.3 Results and discussion

The values reported in Table 5.1, here obtained re-analysing experimental NCP of Refs. [27, 63, 65], are in full agreement with the previous values of $\langle E_K \rangle$ and give new results for the directional contributions $\langle E_K \rangle_\alpha$.

The opposite shifts reported in the lower panel of Figure 5.1 suggest that large changes in the single-particle dynamics in the water molecule are partially cancelled when the total mean kinetic energy is considered. This is confirmed by the small difference in the $\langle E_K \rangle$ values for ice and water at T = 285 K in Table 5.1. Moreover, as an inset in the same Figure 5.1 and looking at the data in Table 5.2, INS can be used to access the anisotropy of the momentum distribution, applying Eq. 5.3 or 5.4. As mentioned, the application of Eq. 5.3 requires that the O is not moving at all. The implication that all the vibrational energy is taken by the H is reflected in the larger value of $\langle E_K \rangle_z$ against that of $\langle E_K \rangle_{str}$ in Table 5.2. Anyway, when the O motion is enabled, through Eqs. 5.4, values of $\langle \mathcal{E}_K \rangle_z$ in Table 5.3 are found in good agreement with those of $\langle E_K \rangle_{str}$ in Table 5.2. There are two comments on this. First, it is fundamental to take into account the motion of the oxygen in order to avoid an overestimate of H stretching energy of 5-10%. Second, the simple hypothesis of a stretching line-shape symmetric with respect to the maximum value gives a good result in the evaluation of $\langle E_K \rangle_{str}$. In particular, only a symmetric line-shape, here defined as a Gaussian in Figure 5.1, allows to avoid the integration in Eq. 5.2 (ore equivalently replace $g(\omega) \to \delta(\omega - \omega_{str})$), and enables the use of Eqs. 5.4.

Moreover, the anisotropic momentum distribution that one can define from INS observables when the $\langle \mathcal{E}_K \rangle$ values are obtained are reported in Figure 5.2. Here, the experimental NCS data are reported in the form of the radial momentum distribution $4\pi p^2 n(p)$ together with the experimental error for ice, water at T = 285 K and T = 673 K (from top to bottom). Each

	T [K]	$\langle E_K \rangle_x$ [meV]	$\langle \mathcal{E}_K \rangle_x$ [meV]	$\langle E_K \rangle_y$ [meV]	$\langle \mathcal{E}_K \rangle_y$ [meV]	$\langle E_K \rangle_z$ [meV]	$\langle \mathcal{E}_K \rangle_z$ [meV]	$\langle E_K \rangle$ [meV]	$\langle \mathcal{E}_K \rangle$ [meV]
ice	271	28.9±2	21.6±1	38.1±3	34.4±1	86.7±3	98.8±1	153.7±2	154.8±1
water	285	18.3±2	19.4±1	51.8±4	33.5±2	83.8±2	101.7±2	153.9±3	154.6±1
water	673	32.3±4	31.4	51.8±5	39.4	92.5±4	107.9	176.6±4.1	178.7

Table 5.3: Comparison between experimental NCS $\langle E_K \rangle$ and $\langle E_K \rangle_\alpha$ from Table 5.1 and the harmonic values $\langle \mathcal{E}_K \rangle_\alpha$ and $\langle \mathcal{E}_K \rangle$ obtained through Eq. 5.4.

panel presents the radial momentum distribution obtained from the values $\langle \mathcal{E}_K \rangle_\alpha$ in Table 5.3 as a green dashed line, and the difference between this function and the NCS experimental function as a red line. These figures show a qualitatively agreement of the NCS and INS line-shapes, resulting in a good agreement of the total mean kinetic energies $\langle E_K \rangle$ and $\langle \mathcal{E}_K \rangle$. The differences in the components $\langle E_K \rangle_\alpha$ and $\langle \mathcal{E}_K \rangle_a lpha$ should be related to anharmonic contributions, measured by NCS but not considered in the INS harmonic model, resulting in a strong couplings of librational, bending and stretching modes.

This study although confirms the effectiveness of the NCS techniques to provide quantitative values of $n(p)$ and $\langle E_K \rangle$ further shows how a combined use of NCS and INS can provide additional and unique information on the harmonic components of these physical quantities.

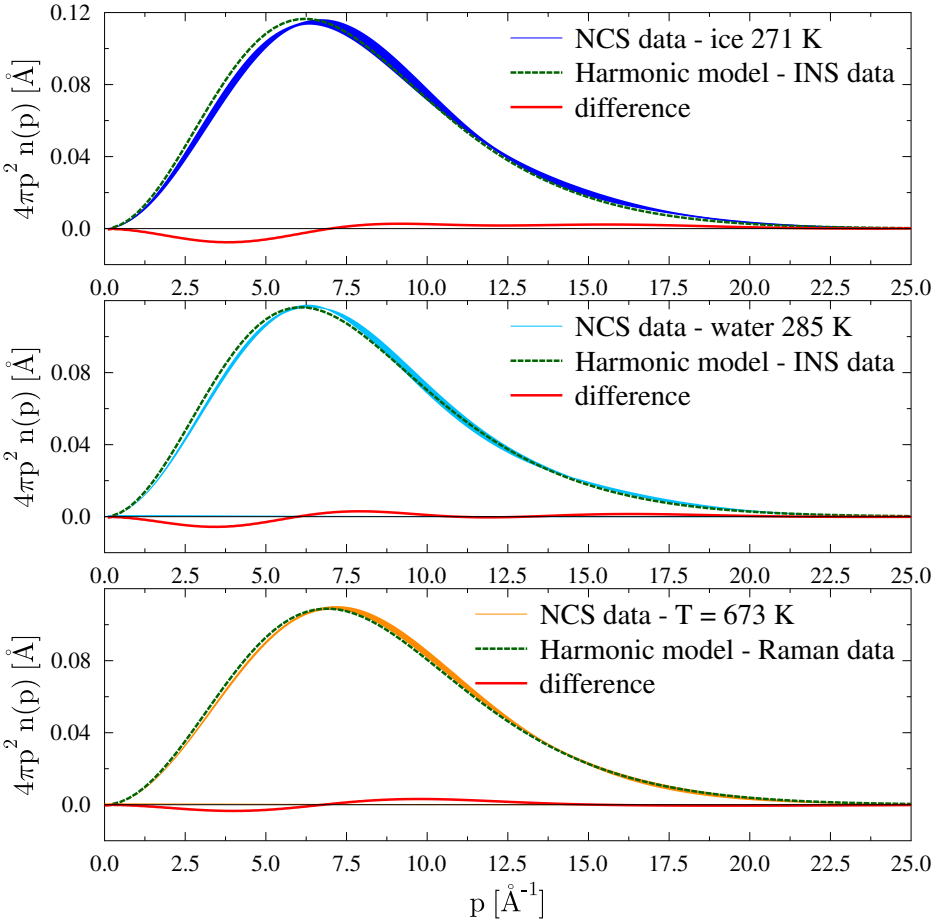

Figure 5.2: Experimental radial momentum distributions for ice *I*h at T = 271 K (upper panel), water at T = 285 K (middle panel) and water at T = 673 K (lower panel). The width of these curves represents the experimental error-bars. Radial momentum distribution defined from the values of $\langle \mathcal{E}_K \rangle_\alpha$ are reported for each temperature as green-dashed lines, while their difference with respect to the experimental curve is reported as red line.

Chapter 6

The melting of Heavy Water

New NCS experiments are presented showing the anisotropy in the momentum distributions of both deuterium and oxygen across the melting of heavy water. A first comparison with ab initio simulations highlights the importance of competing quantum effects across the phase transition. Then, a comparison with kinetic energy contributions from our harmonic model presented in Chapter 4 enables some considerations on the action of HB as an external force spoiling the harmonic approximation for the water molecule.

6.1 Competing Quantum Effects

Even at room temperature, quantum mechanics plays a major role in determining the quantitative behaviour of light nuclei, changing significantly the values of physical properties such as the heat capacity [74]. However, other observables appear to be only weakly affected by NQE: for instance, the melting temperatures of light and heavy water differ by less than 4 K, and the boiling temperatures by just 1 K. Recent theoretical work has attributed this to a competition between intra and inter molecular NQEs, which can be separated by computing the anisotropy of the quantum kinetic energy tensor. The principal values of this tensor change in opposite directions when ice melts, leading to a very small net quantum mechanical effect on the melting point.

Even though NQEs are very large – the zero-point energy content of an O–H stretching vibration is in excess of 200 meV – it is often the case that their net effect on macroscopic properties is relatively small. Recent theoretical analyses [75, 76] have suggested that these small differences could stem from a partial cancellation between quantum effects in the intra

and inter molecular components of the hydrogen bond – so that the net effect is small even if the individual contributions are large. In particular, the competition between quantum effects can be seen very clearly when decomposing the changes in quantum kinetic energy of protons and deuterons along different molecular axes [77, 78].

The mechanism that underlies the competition between changes in the different components of the quantum kinetic energy can be understood by considering as an analogy a two-level quantum system with an environment-dependent off-diagonal coupling β. A small change in the coupling $\Delta\beta$ – arising from a phase transition or some other change in the environment of the system – will shift its eigenvalues by the same amount proportional to $\Delta\beta$, but in opposite directions. Even though this picture is clearly over-simplified, it is consistent with a diabatic state model of the hydrogen bond, [79] it demonstrates that the notion of competing quantum effects CQEs is nothing exotic, and explains why it returns in many circumstances in the study of water and other hydrogen-bonded systems.

Competing quantum effects have in fact been identified in a diverse variety of simulations [75–78], and it seems entirely plausible that they are at the root of the explanation for why many of the properties of water depend only weakly on isotopic composition. The change of many thermodynamic properties on isotopic substitution can be related to changes in the quantum kinetic energy [77, 80].

Let us consider the free-energy of melting at temperature T, $\Delta_{\rm fus}G(T)$. The change in this free energy upon isotope substitution (for instance substituting all the D atoms in heavy water with H) can be related to a thermodynamic integration of the kinetic energy difference between the liquid and the solid phases for that atomic species, as a function of the isotope mass [81–83]:

$$\Delta_{\rm D\rightarrow H}\Delta_{\rm fus}G(T) = -\int_{m_{\rm D}}^{m_{\rm H}} \frac{E_{\rm K}^{(\rm l)}(\mu,T) - E_{\rm K}^{(\rm s)}(\mu,T)}{\mu}{\rm d}\mu. \tag{6.1}$$

As discussed in Ref. [84], one can often assume that $E_{\rm K}^{(\rm s,l)}(\mu)\sqrt{\mu}$ are nearly constant, so the integral can be approximated as

$$\Delta_{\rm D\rightarrow H}\Delta_{\rm fus}G(T) \approx 2\Delta_{\rm fus}E_{\rm K}(m_{\rm D},T)\left(\sqrt{\frac{m_{\rm D}}{m_{\rm H}}}-1\right) \approx 2\Delta_{\rm fus}E_{\rm K}(m_{\rm H},T)\left(1-\sqrt{\frac{m_{\rm H}}{m_{\rm D}}}\right). \tag{6.2}$$

Furthermore, elementary thermodynamic considerations imply that one can write

$$\Delta_{\rm fus}G(m,T) \approx \Delta_{\rm fus}H\left(m\right)\left(1-\frac{T}{T_{\rm fus}(m)}\right) \equiv \Delta_{\rm fus}S(m)(T_{\rm fus}(m)-T), \tag{6.3}$$

where $T_{\rm fus}(m)$ is the melting temperature of an isotopically-pure sample with isotope mass m and the latent heat of fusion $\Delta_{\rm fus}H(m)$ has been assumed to be constant in the vicinity of $T_{\rm fus}(m)$.

Combining Eqs. (6.2) and (6.3), one finds that the kinetic energy change upon melting per heavy water molecule, at temperature T, reads

$$\Delta_{\rm fus}E_{\rm K}(m_{\rm D},T) \approx \frac{\Delta_{\rm fus}S(m_{\rm H})\,(T_{\rm fus}(m_{\rm H})-T) - \Delta_{\rm fus}S(m_{\rm D})\,(T_{\rm fus}(m_{\rm D})-T)\,.}{2\left(\sqrt{m_{\rm D}/m_{\rm H}}-1\right)}. \tag{6.4}$$

Equation (6.4) relates the change in kinetic energy between the two phases (a quantity that would be zero if H and D nuclei did not behave as quantum particles) to macroscopic thermodynamic properties. Evaluating (6.4) at the melting temperatures of heavy and light water yields the more transparent expressions

$$\begin{aligned}
\Delta_{\rm fus}E_{\rm K}(m_{\rm D},T_{\rm fus}(m_{\rm D})) &\approx \frac{\Delta_{\rm fus}S(m_{\rm H})}{2\left(\sqrt{m_{\rm D}/m_{\rm H}}-1\right)}\left[T_{\rm fus}(m_{\rm H})-T_{\rm fus}(m_{\rm D})\right] \\
\Delta_{\rm fus}E_{\rm K}(m_{\rm D},T_{\rm fus}(m_{\rm H})) &\approx \frac{\Delta_{\rm fus}S(m_{\rm D})}{2\left(\sqrt{m_{\rm D}/m_{\rm H}}-1\right)}\left[T_{\rm fus}(m_{\rm H})-T_{\rm fus}(m_{\rm D})\right].
\end{aligned} \tag{6.5}$$

Thus the difference in melting temperature between light and heavy water is directly proportional to the change in the quantum kinetic energy of D upon melting. Moreover $\Delta_{\rm fus}E_{\rm K}$ depends only weakly on the temperature: if we insert the measured values for the entropies of fusion and the melting temperatures into Eqs. (6.5), we obtain $\Delta_{\rm fus}E_{\rm K}(m_{\rm D},T_{\rm fus}(m_{\rm D})) \approx -1.095$ meV per molecule of water, and $\Delta_{\rm fus}E_{\rm K}(m_{\rm D},T_{\rm fus}(m_{\rm H})) \approx -1.062$ meV.

This analysis predicts the change in the quantum kinetic energy of deuterons upon melting, $\Delta_{\rm fus}E_{\rm K}$, to be of the order of -0.5 meV per atom. This is a very small value: to put it into perspective, it is less than 0.5% of the quantum kinetic energy of a deuteron at the melting point. Achieving a level of accuracy sufficient to verify quantitatively this prediction in experiments or simulations will be extremely challenging, and is well beyond the scope of the present work. What one can do is investigate the reason why $\Delta_{\rm fus}E_{\rm K}$ is so small. As we show in the text, this is due to a near-complete cancellation of the changes in the three principal components of the kinetic energy of the deuterium atoms on melting.

The results from NCS experiments have stimulated the development of improved theoretical methods for evaluating the proton momentum distribution [85–88], as well as their application to benchmark systems, with a close interplay between theory and experiment [89,90]. One can infer the anisotropy of the particle momentum distribution from NCS experiments even in cases when only the spherically averaged $n(p)$ is available. In water, this provides insight into the local environment of the proton and can help elucidate the nature of hydrogen bonding [40,91,92], the structure of hydration shells, and the effects of confinement [93,94]. Indeed this information can be seen as the direct experimental counterpart of the decomposition of the quantum kinetic

energy along molecular axes, which has been used so successfully to unravel competing quantum effects in simulations [77, 78, 88].

The focus of NCS studies has recently broadened to consider also heavier atoms [88, 95, 96], which, although challenging because of their less-pronounced quantum nature, promise a more comprehensive picture of the underlying physics. Theoretical calculations [97, 98] demonstrate a sizeable excess of kinetic energy for the oxygen atoms in ice, relative to the classical value. This kinetic energy excess shows a clear dependence on the chemical environment [99], and on the microscopic structure. A direct, accurate measurement of the kinetic energy of the oxygen atoms could for instance shed light on recent findings that indicate an increased localisation of the oxygen in heavy water compared to light water, as evidenced by a 10 per cent overstructuring in the heavy water $g_{OO}(r)$ radial distribution function [100].

In the following, we presents the first direct experimental observation of CQEs achieved by measuring the deuterium momentum distributions $n(\mathbf{p})$ in heavy water and ice NCS and resolving their anisotropy. Results from the experiments, supplemented by a theoretical analysis, show that the anisotropy of the quantum kinetic energy tensor can also be captured for heavier atoms such as oxygen.

6.2 The Experiment

The experiment was performed on a D_2O sample, with a volume 6.3 x 6.3 x 0.5 cm^3, contained in Cu container equipped with Rh/Fe thermocouples, at three different temperatures: at T = 274 K (in the solid), at T = 280 K (in the liquid) and at T = 300 K (in the liquid) at ambient pressure. The temperatures of solid and colder liquid have been chosen respectively three degrees below and above the heavy water melting point. The integrated proton current for NCS data yielded $I = 5800\ \mu Ah$, for T = 274 K and T = 280 K and $I = 5400\ \mu Ah$ for T = 300 K. The Cu container was chosen to ensure an optimal separation of recoil peaks from Cu and O. Examples of t.o.f. data are reported in Fig. 6.1 and 6.2.

In Fig. 6.1, a general picture of the t.o.f. spectra for the back and forward scattering detectors is presented. The count rate and the quality of the data is anyway better in the forward detectors, and only these have been considered in the following data analysis of D. On the other hand, while in forward scattering the O signal and the copper container completely overlap, a good separation in the backward scattering detectors was found, and then the O analysis has been carried out for these detectors only. It is indeed expected that the greater

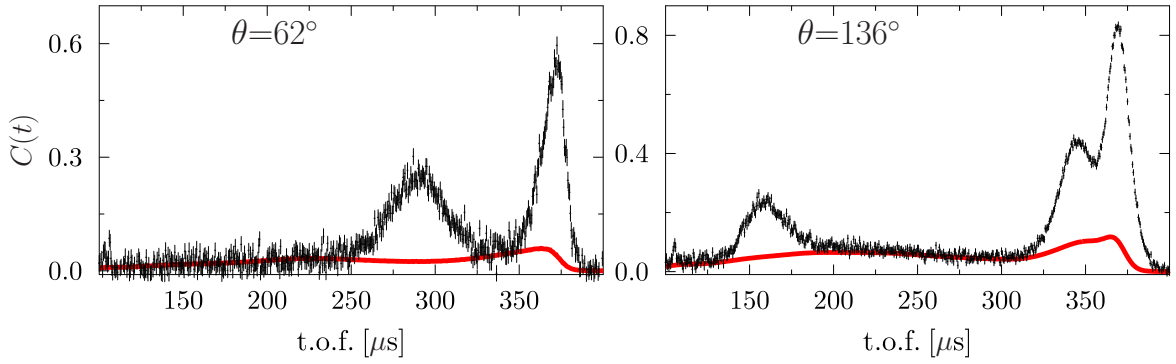

Figure 6.1: Experimental count rate (black) and simulated MS (red line) for a forward detector (left) and a backward group of detectors (right). On the left, it is possible to see the D signal centred around 280 μs, while the O signal is overlapping with the contribution from the copper container. Because of this no information could be extracted regarding the O momentum distribution from the forward scattering detectors. On the right, the D signal is found around 160 μs and the two signals from the O and the container are only partially overlapped.

the angle covered by a detector, the greater the q and the better the separation between two different nuclides, being the position of the centre of their signal related to $q^2/2M$. Data sets at each l-th detector were corrected for γ background using a standard procedure available on VESUVIO [101]. The red line in this figure represents the multiple scattering (MS) correction to the data. This contribution has been simulated through a Monte Carlo routine [63] and corresponds to the double and triple scattering occurring in a plane homogeneous slab filled with the number of atoms composing the experimental sample and container. These routines combine the approximate physical information, that is the NCP of each nucleus build up using a isotropic momentum distribution of guessed variance, with the instrument geometry, that is principal and secondary paths, angle of the detector and gold foil resonance parameters. The MS contribution must be thought as a small peak at the left of the heavy mass signal, representing principally double scattering from the container, and then a (more or less horizontal) line going towards the low t.o.f. region, where the contributions from D-D and D-cell double scattering have the same order of magnitude. The MS is simulated (together with the total scattering) and then subtracted to the experimental data through VESUVIO routines. It must be noticed that the difference between the actual sample and the simulated homogeneous sample is more relevant when the container scattering power is similar to the sample one. In this case, an effective thickness of the simulated slab is introduced.

In Fig. 6.2 (top), a deeper analysis of the case of D is presented. The signal span a large portion of the t.o.f. region, namely between 280 μs and 360 μs. For larger values of q the nuclear signals are broadened and appear to lower t.o.f. (being relative to higher initial energies). In Fig. 6.2 (bottom), the same spectra are transformed in the y variable corresponding to the D mass. It is possible to see how all these contributions can be now summed coherently. Anyway, it is possible to fit the copper-container contribution in the t.o.f. spectra with a Voigt line shape and subtracted from the experimental data. The top panel in Figure 6.3 reports examples of the experimental NCP for D $\bar{F}(y,q)$ averaged over all forward detectors, after both MS and container subtractions.

The O signal has been corrected by the MS contribution through the same simulation as the D. On the other hand, in this case it was not possible to recognize the cell contribution in the t.o.f. space for each detector separately. Both copper and O signal have been then transformed in the O y space, and the cell contribution has been fitted together with the O one. In the bottom panel of Figure 6.3, it is reported the average over all backward scattering detectors corresponding to the O NCP.

When the sample is isotropic, the particle momentum distribution only depends on the modulus of $\mathbf{p}$, and the $\hat{\mathbf{q}}$ direction is immaterial, so the NCP is simply $J_{\mathrm{IA}}(y) = 2\pi \int_{|y|}^{\infty} pn(p)\mathrm{d}p$. This ideal peak profile is broadened by finite-q correction terms $\Delta J(y,q)$, and by convolution with the instrumental resolution function $R(y,q)$, so the experimental NCP, $F(y,q)$, is

$$F(y,q) = [J_{\mathrm{IA}}(y) + \Delta J(y,q)] \star R(y,q). \tag{6.6}$$

The instrumental resolution is a quantity that can be simulated through the same Monte Carlo routines introduced for the correction of the MS, imposing that the nuclear momentum distribution has a vanishing variance. This will simulate the geometrical uncertainties related to the finite width of the gold resonance and of the FC or DD techniques. The additive term for the FSE has been already discussed in Chapter 3. One reasonable (and also insightful) way to extract the physical information content from the experimental $F(y,q)$ profile is to assume that the underlying $n(p)$ arises from the spherical average of an anisotropic Gaussian distribution [63, 71, 90, 97],

$$4\pi p^2 n(p) = \left\langle \frac{\delta(p-|\mathbf{p}|)}{\sqrt{8\pi^3}\sigma_x\sigma_y\sigma_z} \exp\left(-\frac{p_x^2}{2\sigma_x^2} - \frac{p_y^2}{2\sigma_y^2} - \frac{p_z^2}{2\sigma_z^2}\right)\right\rangle. \tag{6.7}$$

This expression involves three parameters – the variances σ_α^2 for $\alpha = x, y, z$ – which are related to three effective principal frequencies ω_α by $\sigma_\alpha^2 = \frac{m\omega_\alpha}{2\hbar}\coth\frac{\beta\hbar\omega_\alpha}{2}$, or to the three components

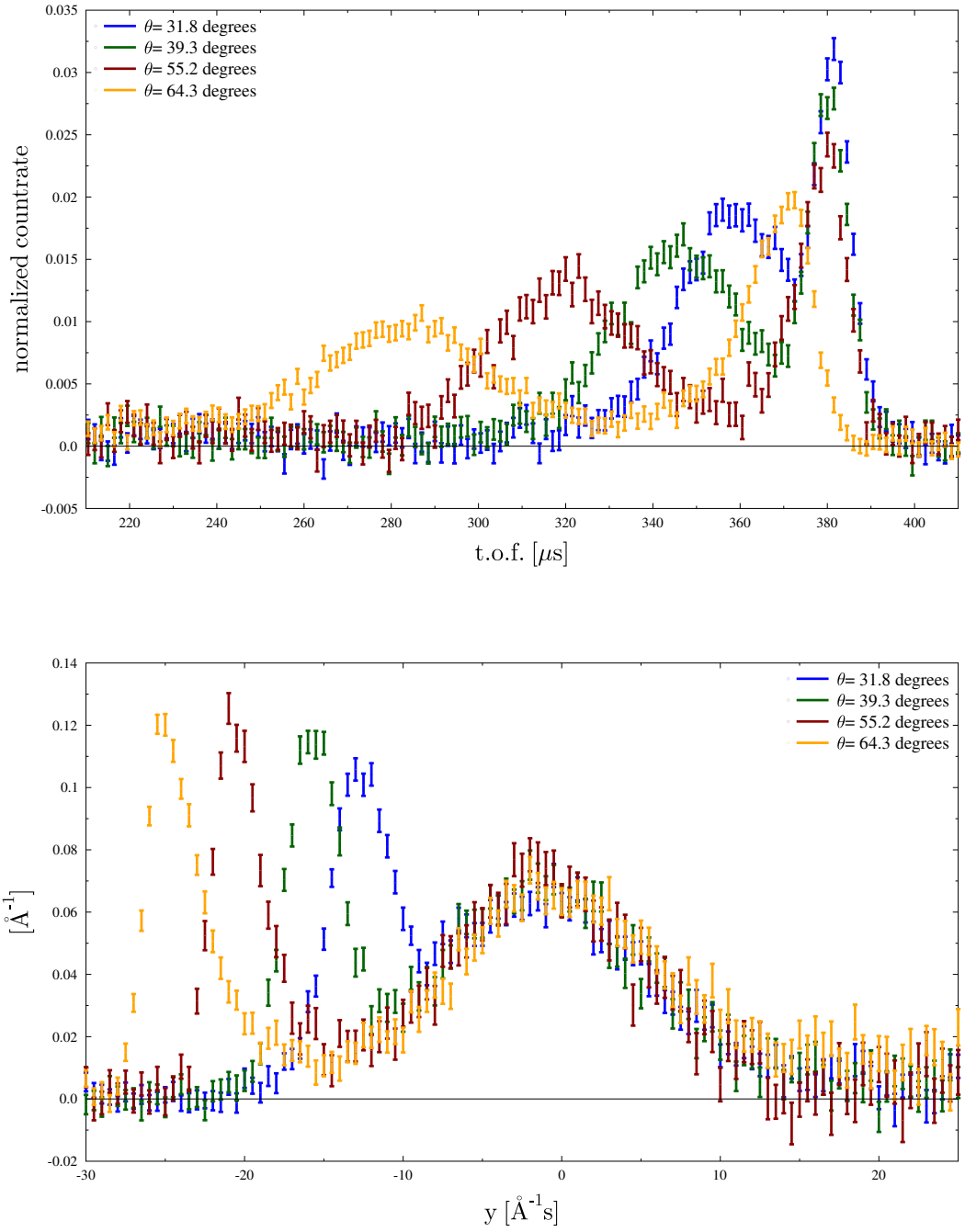

Figure 6.2: Top. Experimental spectra corresponding to four forward scattering detectors as function of the time of flight. The experimental data have been corrected for the γ-background, while the MS and sample container contributions are still present. Bottom. The same spectra as functions of y variable corresponding to D mass.The experimental data have been corrected for γ-background, while the MS and sample-container contributions are still present.

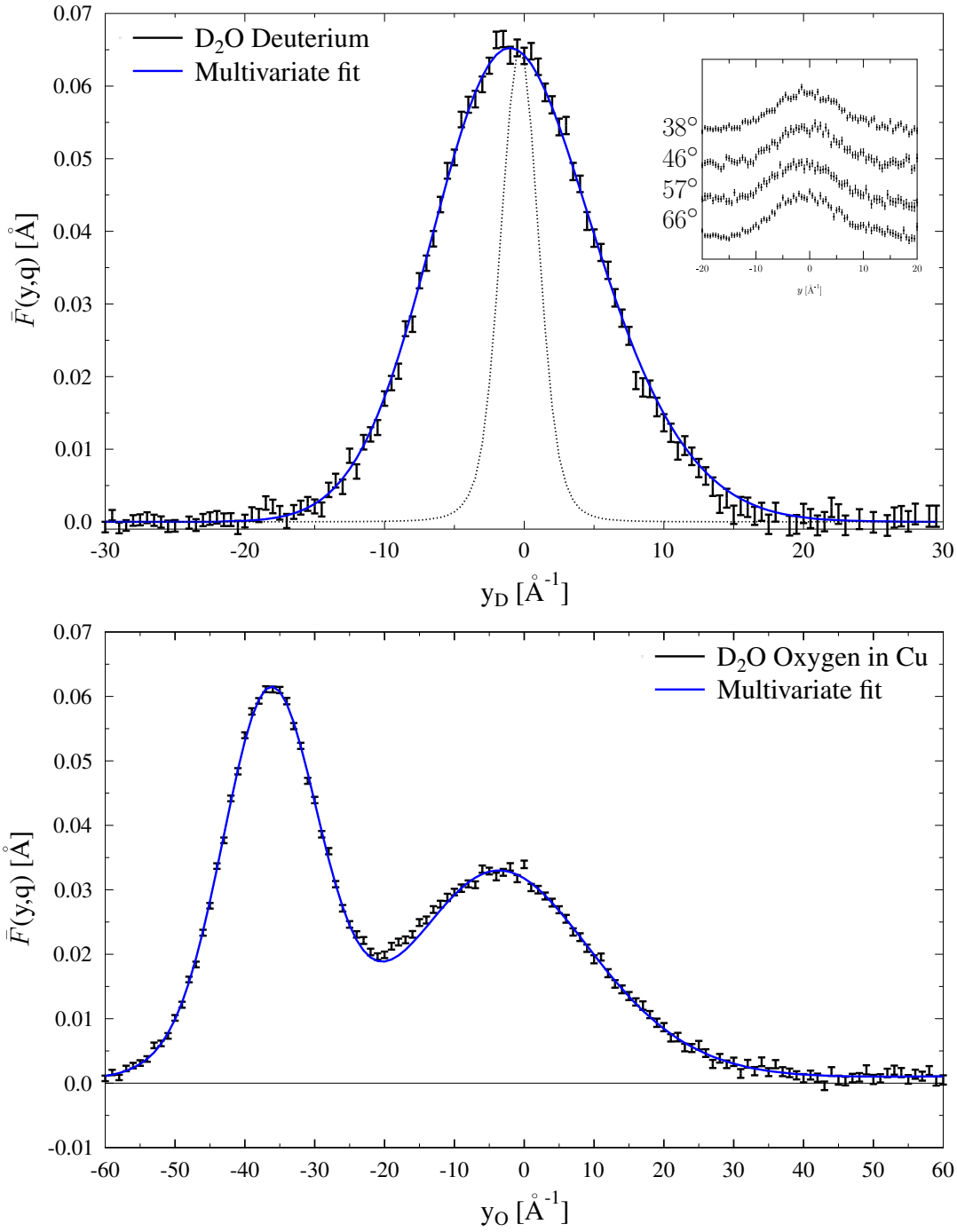

Figure 6.3: Experimental NCS profiles for heavy ice at T = 274 K. The two panels reports the detector-averaged NCS for D (upper panel) and O (lower panel). Best fits using multivariate Gaussian (blue line) are reported. In the case of the O profiles, the peak at $y = -40$ Å^{-1} is due to the contribution from the Cu sample container. The instrumental resolution is reported for the D as a black dotted line, and the insets show examples of the raw data from two individual detectors.

of the quantum kinetic energy by $\langle E_\alpha \rangle = \hbar^2 \sigma_\alpha^2 / 2m$. In the present study, this approach has been used to interpret NCS data acquired on heavy water in the solid at 274 K, and in the liquid at 280 K and 300 K. The fit procedure is based on the assumption that in the y space all spectra represent the same $J(y)$, that is they share the same variances σ_α. Other parameters are detector-dependent. For example, the amplitude of the function $J(y, q)$ can depend on the detector efficiency; the NCP should be centred at $y = 0$, while a small displacement can be introduced as parameter to take into account the imperfect knowledge of the geometry of the instrument. At the end the final fit for D has been done considering simultaneously all the detectors, imposing that all should share the same values for the σ_α, while the parameters A_l and c_l, namely the amplitude and centroid of each detector, could individually change. In the case of O, the backscattering spectra have been summed up in groups sharing the same angular position, and then a simultaneous fit of these grouped spectra has been done. In addition to the previous parameters, other 4 parameter per group have been introduced in this case, to take into account the amplitude, centroid Gaussian and Lorentzian width of the container contribution still present in the spectra and fitted with a Voigt function.

When, according to the previous discussion, the theoretical function $F_l^{the}(y, q)$ for the l detector is defined, a χ^2 procedure is used to find the best fit parameters, trying to minimize the quantity

$$\chi^2 = \sum_l \sum_i \frac{\left(F_l^{exp}(y_i, q_i) - F_l^{the}(y = y_i, q = q_i)\right)^2}{\text{Exp error}_i} \tag{6.8}$$

with i running over the experimental data for each detector. In Figure 6.3 the best fits obtained with an isotropic and the multivariate Gaussian ansatz for $n(p)$ have been reported for both D and O. Clearly, the multivariate Gaussian profile provides a better fit to the experimental data than an isotropic Gaussian. In fact, the best fit $\bar{F}(y, q)$ obtained for an isotropic model is visibly asymmetric. This is a signature of an over-estimation of the finite-q correction term $\Delta J(y, q)$, which occurs because the fit attempts to make up for the anisotropy inherent in the experimental data but absent in the isotropic model.

6.3 Computational methods

To complement this experimental study, we have also performed some new ab initio computer simulations of heavy water and ice, using the same density functional theory framework [102–105] as described in Ref. [88]. Tests with different basis sets and the inclusion of dispersion corrections produced no qualitative changes in the results. Nuclear quantum ef-

fects were incorporated using the PIGLET technique [88], which combines the path integral formalism [106, 107] with a correlated-noise Langevin equation [87, 88], thereby enabling fully converged results for room-temperature water to be obtained with as few as six path integral beads.

The conventional way to extract the particle momentum distribution from the path integral formalism involves opening the path and is computationally very demanding [89]. A simpler alternative is to assume that the momentum distribution can be modelled as a multivariate Gaussian as in (6.7), and to use the eigenvalues of the quantum kinetic energy tensor $\hbar^2 \langle p_\alpha p_\beta \rangle / 2m$ to estimate the principal components of this distribution. The only difficulty here lies in the fact that in the liquid the orientations of the water molecules change with time, so one cannot simply average the centroid virial estimator to obtain the anisotropic kinetic energy tensor.

The interaction between the atoms was modelled by explicitly solving the electronic structure problem within the density functional framework. The Becke-Lee-Parr-Yang exchange-correlation functional [102, 103] was used, together with GTH pseudopotentials [104], as implemented in the CP2K software suite [105]. Wave functions were expanded in the Gaussian DZVP basis set, while the electronic density was represented using an auxiliary plane wave basis, with a kinetic energy cutoff of 300 Ry. We used periodic supercells containing 64 D_2O molecules for the liquid, and 96 molecules for ice, at the experimental density. Tests with the TZV2P basis set, a smaller box of 32 waters, and the inclusion of dispersion corrections [108] did not change the results significantly. Benchmarks performed for the more challenging case of H_2O yielded a total kinetic energy per H atom of 148.2 meV when using our basic setup (BLYP, DZVP basis set, 6-beads PIGLET), the very same value when using the more refined TZV2P basis set, and a very small change to 148.9 meV when using conventional PIMD with 32 beads – a tiny difference that has an even smaller impact when one considers the differences between various phases and/or temperatures. Simulations were performed with a time step of 0.5 fs, starting from configurations equilibrated using an empirical force field [75], with a further 10 ps of ab initio classical molecular dynamics and 3 ps of ab initio PIGLET equilibration. Sampling was performed for 20 ps at each temperature in the liquid, and for 10 ps in ice, which has faster relaxation time.

Nuclear quantum effects were modelled using a combination of path integral molecular dynamics and a tailored correlated-noise Langevin dynamics, which allows one to obtain convergence with a far smaller number of imaginary-time slices. [88] In this case, we used 6 repli-

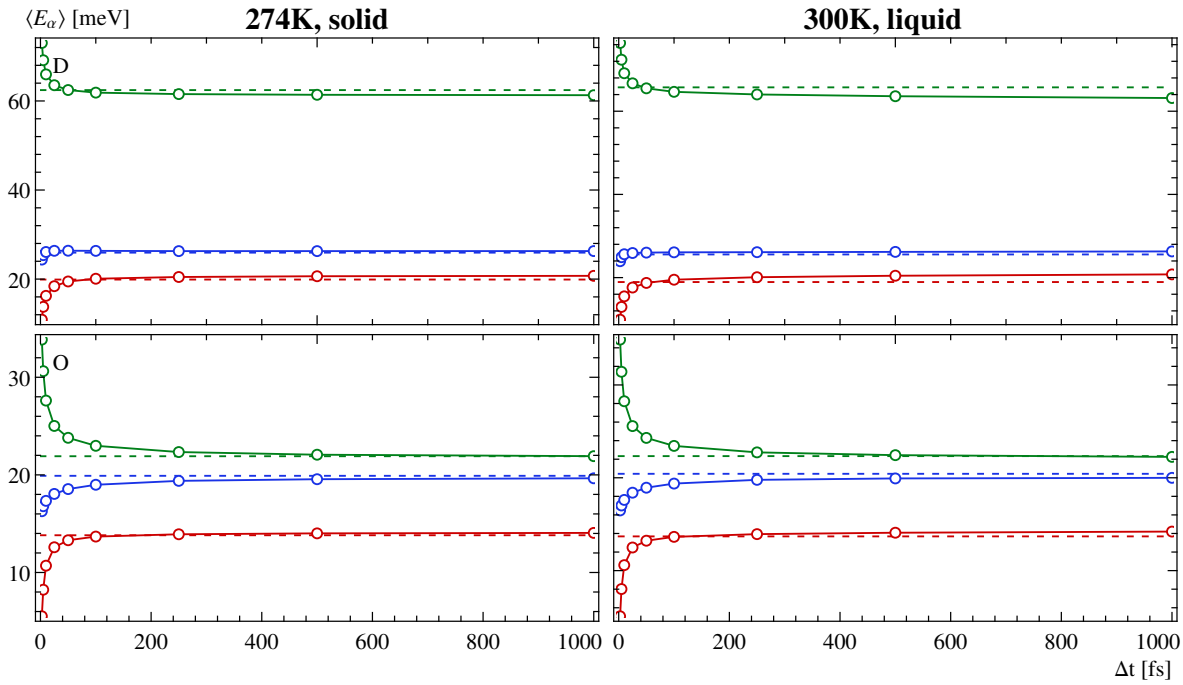

Figure 6.4: TAG approximation [88] to the principal components of the kinetic energy tensor as a function of the moving average window Δt. The left panels show the results for D_2O ice at 274 K, the right panels for the liquid at 300 K. The upper panels show the results for deuterium, the lower panels those for oxygen. The full lines are a guide for the eye, connecting the actual data points – the statistical error is smaller than 0.1 meV. The dashed lines indicate the values of the principal components obtained from the MSD approach.

cas, with a set of parameters designed for systems with frequencies up to $\omega_{\max}$ such that $\hbar\omega_{\max} < 20k_BT$, which can be obtained from an on-line repository [109]. This set of parameters has previously been shown to give full convergence of structural properties and the quantum kinetic energy in the case of room-temperature liquid water. Heavy water exhibits less pronounced quantum effects, making this setup a conservative, safe choice for the present application.

The quantum kinetic energy tensor was evaluated using the centroid virial formula

$$T_{\alpha\beta} = \frac{\delta_{\alpha\beta}}{2\beta} + \frac{1}{4P}\sum_{i=0}^{P-1}\left[(q_{i\alpha} - \bar{q}_\alpha)\frac{\partial V}{\partial q_{i\beta}} + (q_{i\beta} - \bar{q}_\beta)\frac{\partial V}{\partial q_{i\alpha}}\right]. \tag{6.9}$$

Here $q_{i\alpha}$ is Cartesian component α of the position of the i-th replica of the atom in the ring polymer, $\bar{\mathbf{q}} = \sum_i \mathbf{q}_i/P$ is the centroid of the ring polymer, $V(q)$ is the physical potential and $\beta = 1/k_BT$ is the inverse temperature. As discussed in the main text, we used two different approaches to prevent the changing orientation of the molecules in the liquid from spherically

averaging the tensor during the course of the simulation. The mean-square displacement (MSD) alignment approach requires one to align the centroid of each instantaneous configuration of each water molecule to a reference configuration. The same rotation matrix is then used to transform the kinetic energy tensor into the fixed reference frame, where it is averaged before its principal components are computed.

The transient anisotropic Gaussian (TAG) approximation, on the other hand, does not require one to define a molecular entity or a reference structure. It instead performs a running average of the estimator (6.9), computes the eigenvalues of the running-averaged tensor, and averages each of these eigenvalues to evaluate the best estimate of the corresponding principal component. Since averaging and diagonalization do not commute, the TAG estimates of $\langle E_\alpha \rangle$ depend on the width of the time window. As shown in Figure 6.4, however, after a rapid change for small Δt the eigenvalues of the tensor reach plateau values, after which the TAG estimate drifts on a much slower time scale to an isotropic tensor.

In the case of ice, the water molecules cannot change their orientation, and so the slow relaxation time is effectively infinite. The $\Delta t \to \infty$ limit of the TAG approximation corresponds to the correct approximation to the particle momentum distribution as a multivariate Gaussian – a quantity that could be also computed from the end-to-end distribution of an open-path simulation, however at a much greater expense [97]. Therefore, the left hand panels of Figure 6.4 demonstrate that the MSD approximation is close to the correct estimator, despite making the somewhat artificial assumption that the principal axes of the kinetic energy tensor are fixed relative to the molecular axes.

In the liquid, however, one can see that the values of $\langle E_\alpha \rangle$ drift slowly, and so one must choose a point to evaluate the TAG approximation that consitutes an acceptable compromise between converging the centroid virial estimator and avoiding the effect of orientational relaxation. It can be seen that the variation of the principal components is relatively small for values of Δt between 50 and 500 fs, and we chose here a value of 100 fs. Even though in principle the best value for ice would entail a very long averaging window, one must consider that in order to compare different thermodynamic state points it is important to use the same window, so that the effects of incomplete averaging of the estimator are comparable. Whenever it is possible to define individual, rigid molecular entities, one should also evaluate the MSD estimator to check that the results do not depend dramatically on Δt or other details of the analysis, as is the case here.

The overall kinetic energy change of D atoms in D_2O upon freezing is a very small quantity,

arising from a cancellation between contributions that vary in opposite directions. Despite this quantity being small, we are confident that the details of our calculations are sufficiently well converged to assess it reliably, for a given choice of density functional. We cannot however be so confident about the accuracy of density functional theory. It is very hard for an approximate ab initio framework such as DFT to capture quantitatively the result of the delicate cancellation, and match the value of -0.5 meV that can be estimated based on the simple thermodynamic arguments of section 6.1.

For this reason, it is interesting to see whether q-TIP4P/F, [75] an empirical force field that reproduces experimental observables such as the melting temperature, the temperature of maximum density, the red shift of the OH stretching frequency on condensation, can match the thermodynamic value of -0.5 meV for the change in the kinetic energy of the deuterium atoms on melting.

	257K		274K		277K		280K	
	liquid	ice	liquid	ice	liquid	ice	liquid	ice
$\langle E_K \rangle$ D	111.3	111.8	112.3	112.9	112.5	113.0	112.7	113.1
$\langle E_K \rangle$ O	56.0	56.6	57.8	58.2	58.1	58.5	58.4	58.9

Table 6.1: Kinetic energy of D and O atoms in D_2O at different temperatures around the melting point, as computed from a PIMD simulation using the q-TIP4P/F water model. [75].

As it is apparent from Table 6.1, q-TIP4P/F captures the sign and magnitude of the total kinetic energy change at 277K. Furthermore, $\Delta_{\text{fus}} E_K(m_{\text{D}}, T)$ varies very little with temperature, down to the actual melting temperature of D_2O computed for this model [83]. This insensitivity of $\Delta_{\text{fus}} E_K(m_{\text{D}}, T)$ to T justifies performing experiments slightly away from the melting temperature, and suggests that our results should not be dramatically affected by the fact that DFT calculations were performed at a temperature that is unlikely to be precisely the melting temperature of BLYP water.

6.4 Comparison of experimental and *ab-initio* results

Here we compare two different ways around this difficulty. One is to perform a running average of the kinetic energy estimator [88] – the so-called "transient anisotropic Gaussian" (TAG) approximation. For this we used a triangular averaging window of 100 fs, which has previously been shown to give converged results for light water. [88]. Another possibility is to assume

that the principal axes of the kinetic energy tensor will have a fixed orientation relative to the molecular geometry. One can then perform a mean-square displacement (MSD) alignment of the instantaneous configuration of each water molecule to a reference structure, rotating the kinetic energy estimator into the molecular reference frame, and computing its average and its eigenvalues [77, 78]. We will show that the two approaches give results that are consistent with one another, and that they enable a direct comparison with the NCS experiment.

In the upper panels of Figure 6.5, we compare the experimental and theoretical $n(p)$s for liquid D_2O at 300 K. There is a near-perfect agreement between theory and experiment in the case of D. The discrepancy is larger in the case of O, but still very small compared to the deviation from a classical, Maxwell-Boltzmann distribution.

The lower panels show that the discrepancy between theory and experiment is more pronounced when one focuses on the anisotropy of the distribution. The TAG and MSD approximations are consistent with each other. It is interesting that, despite the noticeable differences in the individual values of $\langle E_\alpha \rangle$, the theoretical and experimental $n(p)$s for D are almost indistinguishable. However, the theoretical and experimental $n(p)$s for O, which involve a larger discrepancy in the total $\langle E_K \rangle$ but smaller discrepancies in the individual components, show a more evident difference. Because of the averaging in Eq. (6.7), the computed $n(p)$ depends only weakly on how the kinetic energy components are distributed, but in a more pronounced way on the total kinetic energy.

The relative insensitivity of $n(p)$ to the partitioning of $\langle E_K \rangle$ into three principal components justifies the use of either the TAG or the MSD approach to estimate the anisotropy of the kinetic energy tensor. However, this insensitivity also means that extracting the anisotropy from the spherically-averaged $n(p)$ is an ill-conditioned problem. For this reason, the analysis of the experimental data typically yields larger relative errors in the individual components of the kinetic energy than in the total.

Bearing this in mind, let us now discuss how NCS can provide a direct verification of the concept of competing quantum effects in water. Table 6.2 collects all of the present experimental and theoretical results together in a compact form. The agreement between the total deuterium kinetic energy obtained by NCS and by simulation is almost perfect. The change in kinetic energy between the liquid at 300 K and 280 K is much smaller than the drop in classical thermal energy, which is consistent with the deuteron being almost completely frozen in its vibrational ground state. There is also agreement with previous experiments at $T = 292$ K within their (much larger) error bar [110].

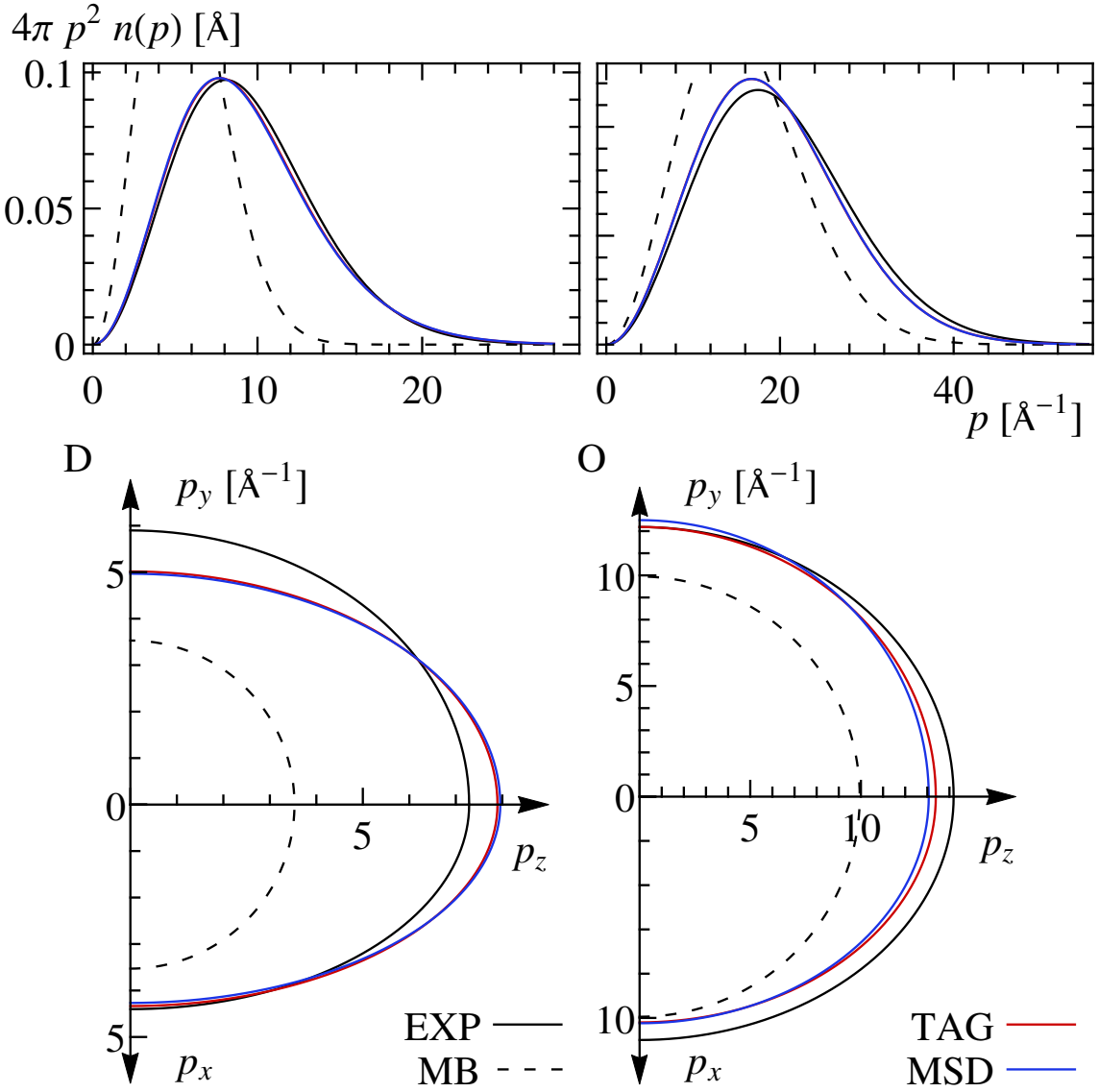

Figure 6.5: (Color online) Comparison of the momentum distributions of O and D in liquid D_2O at 300 K, as obtained from the analysis of NCS experimental data and from two different analyses of the ab initio PIGLET simulations. In all plots, the continuous black curve corresponds to the experimental data, the red curve to a TAG analysis and the blue curve to a MSD analysis of the simulation data. The dashed line corresponds to what would be expected if $n(p)$ were just a classical Maxwell-Boltzmann distribution. The upper panels show the spherically averaged $n(p)$, while the lower panels contain a graphical representation of the anisotropy. The curves correspond to iso-surfaces of the $n(\mathbf{p})$ cut along the xz and yz planes. The contour line is chosen in such a way that the intercepts on the axes are the values of σ_α.

	D [exp]	D [TAG/MSD]	O [exp]	O [TAG/MSD]
D_2O, $T = 300$ K, liquid				$\langle E_{COM} \rangle = 42.1$
$\langle E_x \rangle$	20.1±1.1	19.5 / 18.9	15.8±1.7	13.6 / 13.7
$\langle E_y \rangle$	36.1±2.3	26.1 / 25.6	19.5±1.3	19.4 / 20.4
$\langle E_z \rangle$	55.1±2.3	64.6 / 65.7	26.3±1.5	23.4 / 22.3
$\langle E_K \rangle$	111.3±3	110.2	61.6±3.1	56.4
D_2O, $T = 280$ K, liquid				$\langle E_{COM} \rangle = 39.5$
$\langle E_x \rangle$	18.8±1.1	19.4 / 18.9	16.0±2.3	13.6 / 13.7
$\langle E_y \rangle$	38.6±2.5	25.7 / 25.2	21.0±0.6	19.2 / 20.2
$\langle E_z \rangle$	54.2±2.4	63.6 / 64.6	24.1±2.1	23.2 / 22.2
$\langle E_K \rangle$	111.6±2	108.7	61.1±3.1	56.1
D_2O, $T = 274$ K, liquid				$\langle E_{COM} \rangle = 38.9$
$\langle E_x \rangle$		19.3 / 19.0		13.4 / 13.5
$\langle E_y \rangle$		25.8 / 25.3		19.1 / 20.1
$\langle E_z \rangle$		63.2 / 64.1		23.1 / 22.0
$\langle E_K \rangle$		108.3		55.6
D_2O, $T = 274$ K, solid				$\langle E_{COM} \rangle = 39.2$
$\langle E_x \rangle$	22.5±1.8	20.1 / 19.8	16.1±2.3	13.7 / 13.8
$\langle E_y \rangle$	37.4±2.5	26.3 / 25.9	20.1±1.6	19.0 / 19.9
$\langle E_z \rangle$	48.1±3.4	61.9 / 62.4	24.2±1.4	23.0 / 21.9
$\langle E_K \rangle$	108.0±2	108.3	60.4±4	55.7

Table 6.2: Comparison between theoretical and experimental components of the quantum kinetic energy for D and O in heavy water, at different temperatures. All values are in meV, and the theoretical results have a statistical error bar smaller than 0.1 meV. We also report the computed center-of-mass mean kinetic energy $\langle E_{COM} \rangle$ of the D_2O molecules.

The most interesting results in Table 6.2 concern the behaviour of the momentum distribution in heavy water upon freezing. When going from the liquid to the solid, the NCS data show substantial changes in $\langle E_x \rangle_{\mathrm{D}}$ (associated with motion perpendicular to the plane of the water molecule [77, 88]) and in $\langle E_z \rangle_{\mathrm{D}}$ (associated with motion parallel to the covalent O–H bond). However, the two components change in opposite directions, leading to a much smaller change in the total kinetic energy, which is not statistically significant given the experimental error bars. The increase in $\langle E_x \rangle_{\mathrm{D}}$ is a signature of the more hindered librations in the solid phase, while the decrease of $\langle E_z \rangle_{\mathrm{D}}$ signals a weakening of the covalent bond, which is consistent with the red shift of the stretching peak observed in the vibrational spectroscopy of ice [111]. These observations therefore provide a direct experimental verification of the competition between quantum effects resolved along different molecular axes.

Simulations predict the same qualitative effect on the different components of $\langle E_K \rangle$: $\langle E_z \rangle_{\mathrm{D}}$ decreases on freezing, but $\langle E_x \rangle_{\mathrm{D}}$ increases, leaving almost no change in the total kinetic energy. Performing simulations of the liquid at 280K, and of both the liquid and the solid at 274 K, allows us to infer that these effects are due to the phase transition and not the 6 K temperature drop. Note that our simulations show no sign of an increase in quantum kinetic energy upon supercooling, confirming previous theoretical results for light water [80]. The present experiments were deliberately performed well into the stable solid and liquid phases of heavy water, in order to focus on the experimental signature of competing quantum effects on melting without interference from the more controversial effects that have been observed in NCS measurements on supercooled water [58, 110].

While experiment and theory agree on the qualitative observation of a competition between quantum effects on melting, there are quantitative discrepancies that deserve further comment. For one thing, our DFT results predict $\Delta_{\mathrm{fus}} E_K \approx 0$, whereas simple thermodynamic arguments predict $\Delta_{\mathrm{fus}} E_K \approx -0.5\mathrm{meV}$ (see Eq. (6.5)). As discussed in the SI, a simple, empirical water model [75] yields predictions that are in agreement with the macroscopic thermodynamic data – which is perhaps unsurprising given that this empirical model accurately describes semi-quantitatively the change in melting temperature upon isotopic substitution [83]. While it is remarkable that an ab initio calculation can get so close to the correct result, it is clear that DFT has not yet reached the level of accuracy necessary to obtain a quantitative description of isotope effects. Neither have the NCS experiments reached the exquisite level of accuracy that is necessary to discern such a minute change in the total kinetic energy. As we have demonstrated, one can nevertheless gain insight into the competition of effects that leads to

a small kinetic energy change by resolving the anisotropy of the kinetic energy tensor. The quantitative differences between NCS and PIGLET on the individual components of the kinetic energy, however, indicate that at present this insight is only qualitative.

Table 6.2 also presents the results for the oxygen momentum distribution. While there is good qualitative agreement between theory and experiment, we observe a discrepancy of almost 10% in the total kinetic energy, which may stem from shortcomings of the modelling or from the analysis of the experimental data – which is made harder by the weaker signal given by oxygen and by the partial overlap between the $F(y,q)$ peak of the O and that of the Cu can. Nevertheless, the analysis captures even the comparatively weak anisotropy of the oxygen atom kinetic energy, demonstrating how promising it is to extend NCS to heavy atoms. We anticipate that software and instrument upgrades planned on VESUVIO in the near future will enable a greater precision in the study of the $n(p)$ of both light and heavy atoms, enabling one to access quantitative as well as qualitative information on the particle momentum distribution.

6.5 A harmonic model for heavy water

Let us consider a molecule (D_2O) with the $N = 3$ atoms in the $y - z$ plane. For each of its $3N - 6 = 3$ internal modes, one can define a symmetry-adapted coordinate system (S_1, S_2, S_3) as illustrated in Figure 6.6. To first order, each atom undergoes harmonic motions along the normal coordinates S_i $(i = 1, 2, 3)$. Quantum mechanically, these motions necessarily lead to the emergence of a zero point energy proportional to the vibrational frequency ω_i. The potential energy of the system is the result of three pair interactions with restoring forces proportional to the displacement from the mean nuclear positions. The proportionality constant for the two D-O pairs is given by

$$k_{OD} = \frac{m_D \lambda_3 (1 + \mu \cos^2 \alpha)}{(1 + \mu \sin \alpha \cos \alpha)^2}, \tag{6.10}$$

where $\omega_3 = \sqrt{\lambda_3}$ is the asymmetric stretch frequency, $\mu = 2m_D/m_O$ and m_D and m_O the nuclear masses. Likewise, the proportionality constant for the D-D pair is given by

$$k_{DD} = \frac{m_D \lambda_2 \left[k_{OD}(1 + \mu \cos^2 \alpha) - m_D \lambda_2\right]}{2\left[k_{OD}(1 + \mu) \cos^2 \alpha - m_D \lambda_2\right]}, \tag{6.11}$$

with $\omega_2 = \sqrt{\lambda_2}$ being the bending frequency. Equations (6.10) and (6.11) are derived from the secular equation $|B - \lambda A| = 0$, with A and B being the kinetic- and potential-energy matrices expressed in the symmetry coordinates $\{S_1, S_2, S_3\}$, $\lambda_i = \omega_i^2$ are the eigenvalues of the matrix and $|\ldots|$ indicates the value of its determinant. The symmetry of the modes allows to express

the dynamical 3×3 matrix as a $(2 \times 2)_{\mathcal{S}} \otimes (1 \times 1)_{\mathcal{A}}$ block matrix. Since only two observables, $\omega_2 = \sqrt{\lambda_2}$ and $\omega_3 = \sqrt{\lambda_3}$, are needed in order to fix the free parameters of the model, k_{OD} and k_{DD}, it is possible to evaluate the third eigenvalue of the secular equation, λ_1, and consider the difference with the measured value of ω_1^2 as an estimate of the accuracy of the model. In the case of heavy water, the symmetric stretching frequency evaluated within the present model is 20% higher than the measured one [112]. If one makes use of more than two parameters in an attempt to improve the accuracy of the model, then no prediction can be made on known observables and control on the accuracy of the model is lost.

The asymmetric $(1 \times 1)_{\mathcal{A}}$ block matrix has an eigenvector $s_{\mathcal{A}} = S_3$ that in Cartesian coordinates corresponds to a displacement vector $\xi_{\mathcal{A}} = (y_D, z_D, y_{D'}, z_{D'}, y_O, z_O) = (a, b, a, -b, -\mu a, 0)$, with $a = \sin\alpha$ and $b = \cos\alpha$, with no dependence on the stretching frequency. The symmetric $(2 \times 2)_{\mathcal{S}}$ block matrix has eigenvectors $s_{\mathcal{S}} = S_1 + v(\lambda) S_2$, with

$$v(\lambda) = \frac{\left(2k_{OD}\mu(1 + \mu\cos^2\alpha) - 4k_{DD} - m_O\lambda\mu^2\right)\sin(2\alpha)}{8k_{DD}\cos^2\alpha + k_{OD}\mu^2\sin^2(2\alpha) - 2m_O\lambda\mu(1 + \mu\sin^2\alpha)} \tag{6.12}$$

and with the limits $v(\lambda) \ll 1$ for $\lambda \to \lambda_1$ and $v(\lambda) \gg 1$ for $\lambda \to \lambda_2$. The corresponding displacement vector $\xi_{\mathcal{S}} = (c, d, -c, d, 0, -\mu d)$ in Cartesian coordinates is defined by $c = \sin(\alpha) + v(\lambda)\cos(\alpha)$ and $d = \cos\alpha - v(\lambda)\sin\alpha$. Each $i - th$ mode contributes to the kinetic energy of atom j with a fraction $f_{j,i} = \epsilon_{j,i} / \sum_j \epsilon_{j,i}$ of the mode energy, with $\epsilon_{j,i} = m_j(\dot{y}_{j,i}^2 + \dot{z}_{j,i}^2)/2$. The conditions imposed on the components of $\xi_{\mathcal{A}}$ and $\xi_{\mathcal{S}}$ reflect conservation of linear momentum in the two directions y and z only when these axes are defined as shown by reference frame R1 in Figure 1. However, the quantities $\epsilon_{j,i}$ depend only on the modulus of the vector (y_j, z_j) and then the energy fractions $f_{j,i}$ are invariant under axial rotation.

Following the previous discussion, one can numerically evaluate the parameters $f_{j,i}$ through Eqs. (6.10), (6.11) and (6.12) and the definition of $\xi_{\mathcal{S}}$ and $\xi_{\mathcal{A}}$. The calculation can be readily implemented in a computer routine and applied to any triatomic molecule. The sequential character of this procedure distinguishes the present model from others based on three independent force constants, the latter leading to a hard-to-solve system of coupled nonlinear equations.

Assuming an average frequency ω_τ corresponding to the translational modes, we can define $\tau_j = m_j / \sum_j m_j$. This parameter dictates the amount of energy that the $j - th$ atom draws from this particular vibration. Similar considerations apply to the rotational modes of frequency ω_ρ, whose contribution to the kinetic energy is defined by the ratio of moments of inertia $\rho_j = \bar{I}_j / \sum_j \bar{I}_j$. The quantity $\bar{I}$ corresponds to the spatial average of moments of inertia. With

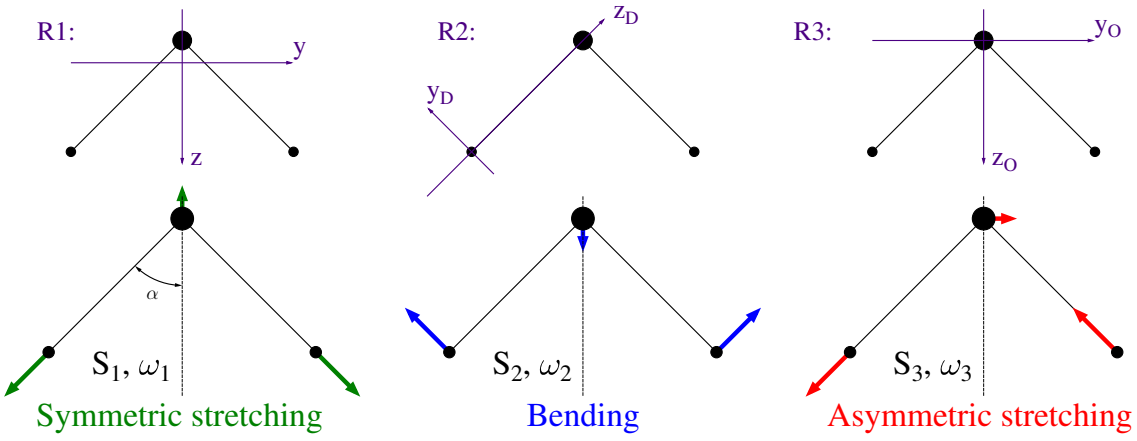

Figure 6.6: Definition of the symmetry coordinates for an isolated water molecule as used in the derivation of the coefficients f_i. The molecule lies in the $y-z$ plane and each axis may be oriented according to the reference frames R1, R2 and R3 (see text).

these definitions, the total mean kinetic energy of one atom (D or O) can be written as

$$\langle \mathcal{E}_K \rangle = 3\tau \langle \mathcal{E} \rangle_\tau + 3\rho \langle \mathcal{E} \rangle_\rho + \sum_{i=1}^{3} f_i \langle \mathcal{E} \rangle_i, \tag{6.13}$$

that is, as the sum of three translations, three rotations and three vibrations, each one with energy $\langle \mathcal{E} \rangle_s = \frac{\hbar\omega_s}{4} \coth \frac{\hbar\omega_s}{2k_B T}$, where $s = \tau, \rho, 1, 2, 3$. Let us now consider a reference frame x,y,z (with the x axis perpendicular to the molecular plane) centred at the average position of each nucleus, representing the three principal axes of an anisotropic $n(\mathbf{p})$. The following interpretation of the NCS observables is based on the definition of a particular orientation of (y, z) for each atom. In the case of the D (Fig 1, R2), the z axis is taken in the direction of the stretching mode, *i.e.*, the mode that mostly contributes to the kinetic energy, the y axis in the direction of the bending mode and the rotation mode around the x axis. Rotations around y and z will contribute to the kinetic energy in the x direction. By considering an additional translational contribution along each direction, one can define for the D atom

$$\langle \mathcal{E}_K \rangle_x = \tau \langle \mathcal{E} \rangle_\tau + 2\rho \langle \mathcal{E} \rangle_\rho; \;\; \langle \mathcal{E}_K \rangle_y = \tau \langle \mathcal{E} \rangle_\tau + \rho \langle \mathcal{E} \rangle_\rho + f_2 \langle \mathcal{E} \rangle_2; \;\; \langle \mathcal{E}_K \rangle_z = \tau \langle \mathcal{E} \rangle_\tau + f_1 \langle \mathcal{E} \rangle_1 + f_3 \langle \mathcal{E} \rangle_3. \tag{6.14}$$

In the case of O, the most relevant contribution to the kinetic energy arises along the direction of the bending and the symmetric stretching modes (see Fig 1). Consequently, we take the z axis along this direction, while the y axis remains orthogonal and along the asymmetric stretching and the rotation around the x axis. For O one can then define

$$\langle \mathcal{E}_K \rangle_x = \tau \langle \mathcal{E} \rangle_\tau + \rho \langle \mathcal{E} \rangle_\rho; \quad \langle \mathcal{E}_K \rangle_y = \tau \langle \mathcal{E} \rangle_\tau + f_3 \langle \mathcal{E} \rangle_3; \quad \langle \mathcal{E}_K \rangle_z = \tau \langle \mathcal{E} \rangle_\tau + f_1 \langle \mathcal{E} \rangle_1 + f_2 \langle \mathcal{E} \rangle_2. \tag{6.15}$$

		τ	ω_τ [meV]	ρ	ω_ρ [meV]	f_1	ω_1 [meV]	f_2	ω_2 [meV]	f_3	ω_3 [meV]
Ice	D	0.1	17.7	0.456	52.7	0.479	278	0.405	151	0.460	294
	O	0.8		0.088		0.042		0.190		0.079	
Water	D	0.1	15.1	0.457	46.9	0.499	296	0.410	150	0.458	310
	O	0.8		0.086		0.001		0.180		0.084	

Table 6.3: Optical frequencies and $\widehat{DOD}$ angles taken from Refs. [112–116], along with calculated values for τ, ρ, f_i using our model. The value for $\widehat{DOD}$ angle is $2\alpha = 108.4$ degrees for ice and $2\alpha = 106.0$ degrees for water.

These contributions are calculated using frequencies from optical spectroscopy [112–116] as shown in Table 1. The corresponding $\langle \mathcal{E}_K \rangle$ and $\langle \mathcal{E}_K \rangle_\alpha$ are reported in Table 2. The values for the energy fractions τ, ρ, f_i have also been evaluated within the present model. These results are in good agreement with those reported in the literature [52, 53].

6.6 Comparison of experimental and harmonic results

We compare calculated values for $\langle \mathcal{E}_K \rangle$ and $\langle \mathcal{E}_K \rangle_\alpha$ with the results of NCS measurements on D_2O at $T = 274$ K (ice) and $T = 280$ K (liquid) [117], performed using the VESUVIO spectrometer. The resulting values for $\langle E_K \rangle$ and $\langle E_K \rangle_\alpha$ are reported in Table 2.

As far as D is concerned, our results show good agreement between $\langle \mathcal{E}_K \rangle$ and $\langle E_K \rangle$. In a recent study of liquid and solid light water [118], a similar agreement was found between the NCS value for $\langle E_K \rangle$ and $\langle \mathcal{E}_K \rangle$ derived from vibrational INS frequencies. Our model also reproduces quantitatively changes in directional kinetic energies associated with the liquid-to-solid phase transition, as observed by NCS. In this case, the decrease of the $z-$component in this transition is caused by an increase in HB strength in the solid phase – *i.e.*, stronger HBs lead to a red-shifted stretching frequency. Thus, both NCS experiment and our model agree on a small decrease by 5-6 meV of the kinetic energy along the z direction

The situation is markedly different for the component $\langle E_K \rangle_z$ and $\langle \mathcal{E}_K \rangle_z$. In this case, we find that the discrepancy between our model and NCS measurements is of approximately 20 meV (see Table 2). More generally, the observed differences between $\langle \mathcal{E}_K \rangle_\alpha$ and $\langle E_K \rangle_\alpha$ may be traced back to the assumption built into our model of decoupled motions when z is along the direction of the covalent bond (stretching mode). Moreover, intermolecular forces (neglected in

	$\langle E_K \rangle_x$ [meV]	$\langle \mathcal{E}_K \rangle_x$ [meV]	$\langle E_K \rangle_y$ [meV]	$\langle \mathcal{E}_K \rangle_y$ [meV]	$\langle E_K \rangle_z$ [meV]	$\langle \mathcal{E}_K \rangle_z$ [meV]	$\langle E_K \rangle$ [meV]	$\langle \mathcal{E}_K \rangle$ [meV]
D								
Liquid	18.8±1.1	15.1	38.6±2.5	22.9	54.2±2.4	73.6	112±2	112
Solid	22.5±1.8	15.9	37.4±2	23.8	48.1±3.4	68.3	108±2	108
O								
Liquid	16.0±2.3	10.4	21.0±0.6	16.1	24.1±2.1	16.4	61.1±3.1	43.4
Solid	16.2±2.3	11.0	20.1±1.6	15.4	24.2±1.4	19.7	60.4±4	46.1

Table 6.4: Comparison between experimental $\langle E_K \rangle$ and $\langle E_K \rangle_\alpha$ from Ref. [117] and our model using the parameters in Table 1.

our model) can lead to a redefinition of normal-mode coordinates. Interestingly, we note that much closer agreement with NCS may be achieved via a tilt of the z axis so as to maximize the contributions of the symmetric stretching and bending modes to $\langle \mathcal{E}_K \rangle_z$, resulting in a value for this energy of ca. 50 meV. Similar considerations would also apply to the y direction, with an associated kinetic energy of 40 meV. In summary while calculated and NCS values of $\langle \mathcal{E}_K \rangle$ and $\langle E_K \rangle$ yield information on the overall magnitude of NQEs, the directional components $\langle \mathcal{E}_K \rangle_\alpha$ and $\langle E_K \rangle_\alpha$ highlight the role of intermolecular interactions on single-particle momentum distributions.

From Table 2, one observes that for O atom the $\langle \mathcal{E}_K \rangle$ is underestimated of about 15 meV relative to $\langle E_K \rangle$ [117]. This finding may be ascribed to the long-range order of the HB network and to its effect on translational motions. It is entirely plausible that the present model underestimates these effects: for example, in Table 1 one can see that the contribution from translational modes dominates $\langle \mathcal{E}_K \rangle$.

In conclusion, comparison between our model and NCS shows that $\langle E_K \rangle$ for D in D_2O may be determined by combining translational, rotational and vibrational frequencies from optical spectroscopy and INS, in agreement with previous work on light water [118]. These results suggest that a combined use of optical spectroscopy, INS and NCS measurements can give simultaneous access to the magnitude of underlying NQEs in water, as well as both local and intermediate-range-scale properties.

A conclusive note on these Section and Chapter regards the application of similar first-order quantum harmonic models to future NCS experiments. The generalization to biatomic

and linear triatomic molecules is trivial, while the generalization to more complicated molecule is still possible. The results from Density Functional Theory and PIMD are powerful tools and their agreement with experimental results is a test of their validity. Anyway, a (not-always-present) agreement of experimental results with simpler harmonic models highlights the importance of those cases where the deviations are larger, and a stronger effect of high-order quantum contributions is present.

Chapter 7

Phase transitions across pseudo-critical lines

In this Chapter, I present the changes in vibrational spectra occurring in the passage from liquid to supercritical water and from high-density to low-density amorphous ices. The first of these measurements was performed at SNS, on the SEQUOIA spectrometer, while the second was performed at ISIS, on the MARI spectrometer. I participated in the experiments, reduced and analysed the data and interpreted them through the conclusion that will be drawn at the end of this Chapter. The two experiments are here discussed together since they both can be related to the idea of pseudo-critical lines.

7.1 Supercritical water

The supercritical phase of water is an interesting regime of water both in Physics and technology. As anticipated in the Introduction, supercritical water (SCW) is a phase of water defined in the region of temperatures higher than $T_C = 647$ K and pressures higher than $P_C = 22.064$ MPa. Several recent developments have resulted in increased attention in supercritical water.

The use of SCW allows hazardous and toxic organics to be fully oxidized making them innocuous [119, 120] and organic waste to be partially transformed into light feed-stocks [121]. Moreover, the total thermal efficiency of coal-fired power plants is increased at supercritical pressures, where there is no liquid-vapour phase transition and there is no such phenomenon as critical heat flux. Finally, SCW-cooled reactors are considered to be promising candidates of advanced power reactors belonging to Generation IV reactor technology [122].

The critical point is the final point of the line separating the vapour and liquid region. The classical definition of the supercritical region is the region where no physical observable can be measured enabling the distinction of a liquid from a solid. The behaviour of several thermodynamic quantities such as the heat capacity brings to the idea that the supercritical region should be divided into two subregions, a liquid-like one and a vapour-like one. This difference can be explained by the fragmentation of the water molecule clusters existing in the liquid and liquid-like region (kept together by HBs into smaller groups or into individual molecules when they enter to the vapour-like region. The border line between the two subregions is defined as the locus of specific heat maxima starting at the critical point and it is referred to as the pseudo-critical line [123].

Hence, the problem of the presence of HB in SCW is of crucial importance and has been addressed in several ways, both experimental and computational. Recent diffraction studies [124] have suggested the disappearance of HB already at 673 K, due to the disappearance of a fingerprint peak at 1.9 Å generally due to HB in the OH pair distribution function. On the other hand, nuclear magnetic resonance measurements [125] have found that still a 29% of the HB present in liquid water at room temperature can be found at the temperature of 673 K. A huge effort on the subject has been spent through vibrational studies as Raman, infra-red and INS, since the position of vibrational frequencies can be sensitively shifted according to the strength and the extent of the HB network, for stretch, rotation and translation modes.

When HBs are broken, the tetrahedral structure of the condensed phases of water is lost, and it is generally suggested that only monomers and dimers can be found. This is also confirmed by the result that the stretching frequency in the supercritical phase approaches the value of the isolated monomer when the temperature increases. It is clear that it is not possible to access the solution to this mystery separately considering crystallographic or spectroscopic studies, and that a cooperation of all these techniques is necessary in order to cease a long and controversial debate.

7.1.1 Experiment and data analysis

The INS experiment was performed on SEQUOIA in the temperature range from 553 K to 823 K, at a fixed pressure of 25 MPa, that is from the sub-critical region ($T < T_C$) to the SC region, and across the pseudo-critical line. A bulk water sample in this thermodynamic region is very aggressive and a special Ti container was designed for the experiment: water was inserted in 38 cylindrical tubes with a diameter of 1mm. The dimensions of the container were (5 cm)×(5

cm)×(2.03 mm).

The correction of MS was treated considering a double scattering contribution with each scattering occurring at approximately 90 degrees. This approximation holds for angles lower than 25 degrees. For this reason, the collected data were firstly analysed as functions $S(\theta, \omega)$ instead of $S(\mathbf{q}, \omega)$. MANTID [126] routines were used to sum the collected data from detectors in different angular positions in groups centred at 6, 12, 18 and 24 degrees. During the same procedure the experimentally-measured contribution from the cell was removed as a background function. The MS approximation is defined by the Gaussian function

$$MS(\hbar\omega) = \frac{A}{\sqrt{2\pi}\sigma_{MS}} e^{-\frac{(\hbar\omega - E_{MS})^2}{2\sigma_{MS}^2}} \tag{7.1}$$

where $E_{MS} = 2E_i$. The MS Gaussian contribution was fitted on the experimental data in the region 600 meV $\leq \hbar\omega \leq$ 770 meV. The fit parameters were the amplitude of the signal, A_{MS} and its variance, σ_{MS}, while the centre of the Gaussian was fixed at $E_{MS} = 1580$ meV. As a check, the ratio of the MS contribution with respect to the area of the corrected $S(\theta, \omega)$ was compared with the theoretical calculation by Sears [127]

$$\delta = \frac{1}{2}\Sigma d \left(-\ln \Sigma d + 0.923 + \frac{1}{3}\Sigma d \right) \sim 22\% \ - \ 17\% \tag{7.2}$$

The corrected data at $T = 553$ K are presented in Fig. 7.1, and the correction process bringing to that result is graphically reported in Fig. 7.2. Since the data statistics for the last two temperature was poorer than the other cases, the data are presented in twice the usual binning.

The corrected data for the $S(\theta, \omega)$ were firstly transformed in the dynamic structure factor $S(\mathbf{q}, \omega)$ and then reduced to the hydrogen projected density of states $g(E)$ through the equation

$$g(E) = \lim_{q^2 \to 0} \frac{S(\mathbf{q}, E)}{q^2} 2ME \frac{e^{2W}}{n(E) + 1} \Bigg|_{E=\hbar\omega} \tag{7.3}$$

The approximation leading to the hydrogen projected density of states is that only H gives a significant contribution to the neutron scattering, that is true after the cell subtraction, that anyway would give no contribution in the stretching region, and considering that H has a cross section about 20 times larger than O, other than a double number of atoms. Moreover, the Bose factor, *i.e.*, the occupation function $n(E)$, was defined as

$$n(E) = \frac{1}{\exp\left(\frac{E}{k_B T}\right) + 1}, \qquad \frac{1}{n(E) + 1} = 1 - \exp\left(-\frac{E}{k_B T}\right) \tag{7.4}$$

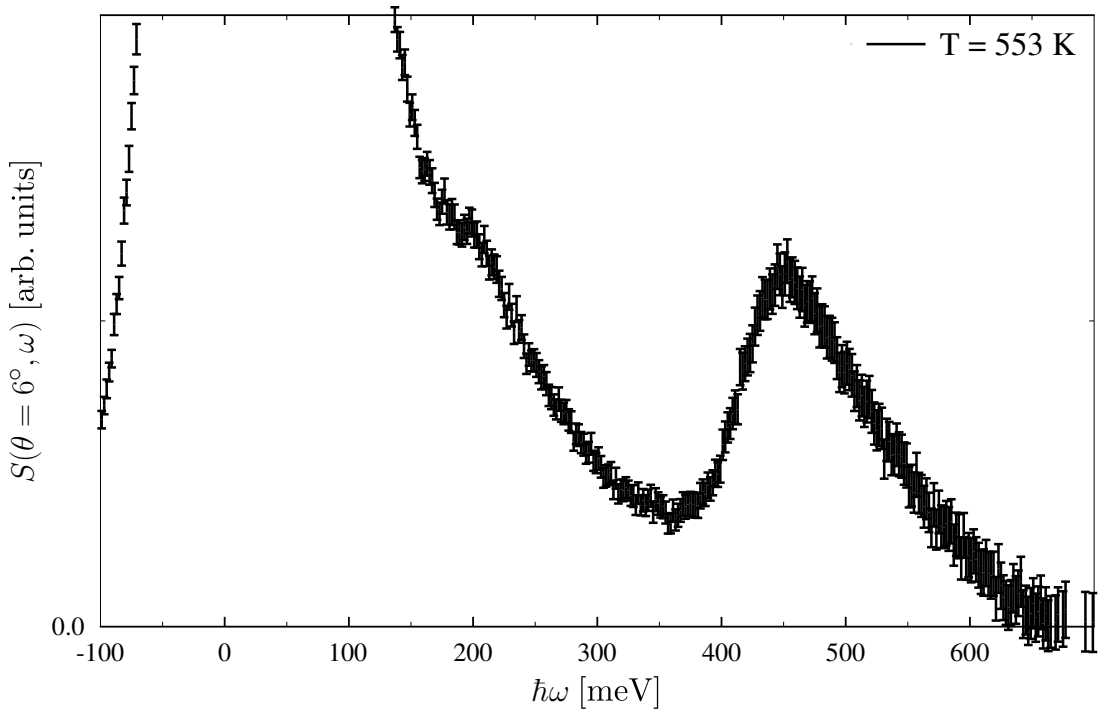

Figure 7.1: $S(\theta, \omega)$ at T = 553 K after the subtraction of the cell and the MS contribution for the detector banks around 6 degrees.

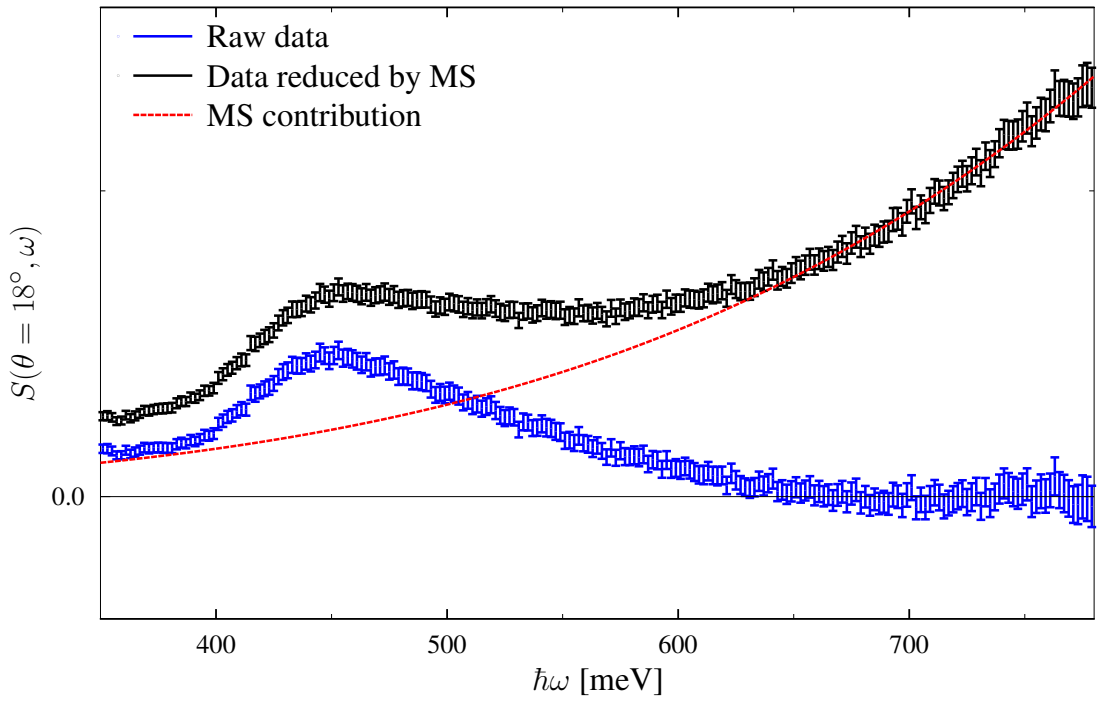

Figure 7.2: $S(\theta, \omega)$ at T = 553 K before (black) and after (blue) the correction by MS contribution (red).

depends on the temperature of the sample. The Debye-Waller factor is here considered for a isotropic sample in the approximation

$$2W = -q^2\langle u^2\rangle = \frac{\hbar^2\langle u^2\rangle}{2M\langle E_K\rangle} \tag{7.5}$$

with $\langle E_K\rangle$ the mean kinetic energy of the proton. This value can be defined through a NCS measure that is in this moment ongoing and will be presented in the next future, but is here taken from a published NCS value on SCW at a similar thermodynamic point, $\langle E_K\rangle = 178$ meV. This value provokes a mean square displacement of 3.4×10^{-2} Å^2.

7.1.2 Discussion

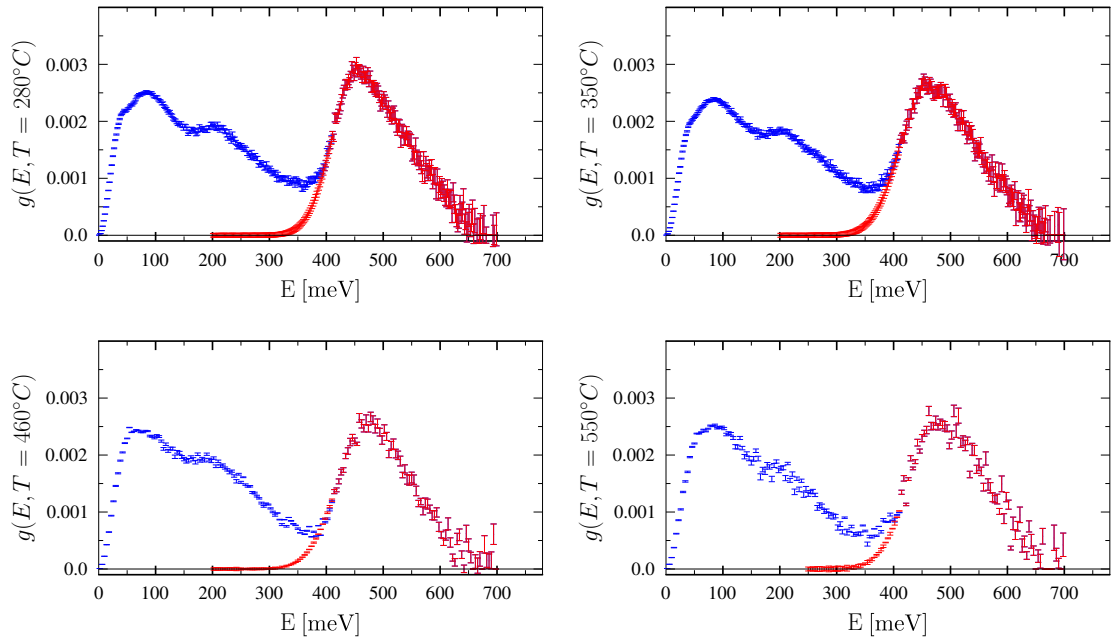

Figure 7.3: Density of states $g(E)$ (blue) and stretching contribution $g_{str}(E)$ (red) for T=280 C, 350 C, 460 C, 550 C. The main difference between the lower temperatures (top) and the higher temperatures (bottom) is the shift, in opposite directions, of stretching and libration contributions, while the bending is not effected.

In Figure 7.3 the densities of states for all the temperatures considered in this experiment are presented. Three main contributions can be appreciated: a librational peak below 100 meV, a bending peak around 200 meV and a broad stretching peak between 400 meV and 500 meV. As a matter of fact, a strong difference in the position of the rotation and stretching maxima is found when the pseudo-critical line is crossed. When this happens, the librational contribution

is red-shifted while the stretching contribution is blue-shifted. These are both suggestions that the HB interaction is decreasing in intensity when going to the SC region with both $T > T_C$ and $P > P_C$, *i.e.*, increasing the HB distance as the density largely decreases from 0.77 g/cm^3 to 0.10 g/cm^3. The stretching signal has been isolated from the complete $g(E)$ through a Gauss-Hermite fit on the rising shoulder of the stretching peak, in the energy region from 400 meV to the value for the maximum. This contribution is reported as a red line in the same figure.

From the complete density of states and the stretching contribution, it is possible to define the total energy due to all the vibrational modes E_{tot} and the energy due to the stretching mode only E_{str} by the relation

$$E_{tot} = \int \frac{E}{4} g(E) \coth\left(\frac{E}{2k_B T}\right) \qquad E_{str} = \int \frac{E}{4} g_{str}(E) \coth\left(\frac{E}{2k_B T}\right) \tag{7.6}$$

The corresponding values are reported in the Table 7.1.

T [K]	P[MPa]	ρ [kg/m^3]	E_{tot} [meV]	E_{str} [meV]	$E_{tot} - E_{str}$ [meV]
553	25.0	777	218	132	86
623	25.0	625	237	153	84
663	25.0	215	241	156	85
733	25.0	104	243	155	88

Table 7.1: Results from the present study. State variables defining the measured total energy E_{tot} and stretching energy E_{str} evaluated through Eq. 7.6. ω_{str}.

High values for the total energy and of the stretching energy are found as compared to typical values such as those reported in Chapter 5. This discrepancy suggests that some contributions such as multi-phonon or over-tones are still present in the broad stretching peak and have not been correctly subtracted. As a demonstration, in Table 7.1 we evaluate the *non-stretching* energy $E_{tot} - E_{str}$ as the contribution due to the translational, rotational and bending modes. These values are in line with the measured mean kinetic energy components presented in Chapter 5, *e.g.*, $\langle E_K \rangle_x + \langle E_K \rangle_y = 83$ meV for the $T = 673$ K. An estimate of the total energy due to all the vibrational modes can be obtained adding to the *non-stretching* contribution, the quantity

$$E(\omega_{str}) = \frac{\hbar\omega_{str}}{4} \coth\left(\frac{\hbar\omega_{str}}{2k_B T}\right). \tag{7.7}$$

Then, we take the raising line-shape for $\omega < \omega_{str}$ previously defined and symmetrize it with respect to ω_{str}. Then, being the stretching component a symmetric function of $\omega - \omega_{str}$, it can be substitute with a Dirac delta-function $\delta(\omega - \omega_{str})$ when the energy contribution is evaluated, leading then to Eq. 7.7.

Moreover, in Chapter 4 it has been pointed out that only about a 90 % of this energy is given to the H $\langle E_K \rangle$, being the rest adsorbed in the O motion. Hence, we define

$$\langle E_K \rangle = \frac{f_2 + 3\rho}{2}(E_{tot} - E_{str}) + \frac{f_1 + f_3}{1}E(\omega_{str}) + \frac{3}{2}\tau k_B T, \tag{7.8}$$

i.e., the vibrational energies weighted by the previously defined energy fractions, the values presented in Table 7.2 are obtained. In particular, the first term is the ratio of the sum of the fractions for 1 bending plus 3 rotations to the $4 \times \frac{1}{2}$ classical contributions per d.o.f. that one would have for a fixed O. The second term is the ratio of the sum of the fractions for the symmetric and anti-symmetric modes to the $2 \times \frac{1}{2}$ for 2 classical contributions. The third term is considered as classical at these high temperatures and ranges between 3 meV for T = 523 K and 6 meV for T = 823 K. In the Table 7.2, these estimates for the total $\langle E_K \rangle$ are compared with some NCS results from previous experiments.

T [K]	P[MPa]	ρ [kg/m^3]	ω_{str} [meV]	$E(\omega_{str})$ [meV]	$\langle E_K \rangle$ [meV]
553	25.0	777	450	112	181
573	12.0	700			172
623	25.0	625	454	113	181
663	25.0	215	466	116	186
673	106.0	701			178
733	25.0	104	472	118	191

Table 7.2: The total mean kinetic energy $\langle E_K \rangle$ as defined in Eq. 7.8, together with the thermodynamic variables T, P and density ρ and the stretching frequency ω_{str} and corresponding mode energy. Previous results are marked in red.

In Figure 7.6, the comparison of all the 5 temperatures of this experiment shows a clear shift of the stretching peak. Previously measured $g_{str}(E)$ for water at T = 276 K (blue solid line) is also reported as a comparison. It is possible to subdivide the five data in two sub-groups. The first two temperatures, for $\rho < \rho_C = 0.322$ g/cm^3 and $T < T_C$, are in the liquid-like region and have close values for the stretching frequency, changing of only 4 meV and within the experimental uncertainty. On the other hand, when the pseudo-critical line is crossed a large shift of 12 meV can be appreciated because of the passage to the gas-like phase. In the first panel, a complete agreement between the maxima of the present data and the previous data at T = 573 K is found. We note that the two measures have almost the same density as well. When one looks at the third panel, a sensible discrepancy between the maxima of the present

data and the previous data at T = 673 K can be appreciated. The reason is that even if the temperature is almost the same, the density largely changes since the previous experiment was performed at 106 MPa.

7.2 Amorphous ices

In everyday life, the cooling of liquid water at temperatures lower than the melting point T = 273 K at P = 0.1 MPa causes a phase transition to ice Ih. When bulk liquid water with a small percentage of impurities is considered, it is possible to cool it even below the melting temperature before spontaneous crystallization sets in [128]. Experimentally, the lowest temperature at ambient pressure where liquid water can be cooled is called the homogeneous nucleation temperature T_H(P = 0.1 MPa) = 231 K at ambient pressure [129]. It is not possible to have liquid water under the homogeneous nucleation temperature, but when the temperature is lower than T_A(P = 0.1 MPa) 150 K, it is possible to find solid phases that have no crystalline structure therefore defined amorphous. The existence of two different phases of amorphous ices [130], firstly suggested in computer simulations [131], was experimentally proven in 1980: Low Density Amorphous (LDA) and High Density Amorphous (HDA) ice [132, 133]. In addition, at the beginning of this millennium, a new and even denser similar phase was also discovered and named very High Density Amorphous (vHDA) ice [134]. There is no way to study liquid water in the region between the temperature of homogeneous nucleations T_H(P) and the higher-temperatures boundary of the amorphous ices phases T_A(P). Therefore, this region is named *no-Man's land*. Anyway, in [135] it is suggested that inside high-pressure cryo-cooled protein crystals in the temperature range between 80 K and 170 K, super-cooled liquid water studied through X-ray diffraction can be modelled as a linear combination of HDA and LDA ice structures. This finding, together with other computer simulations [136], suggested a second critical point in a region hardly accessed and a relative pseudo-critical line starting from that point and dividing two amorphous ices thought as liquid-like phases and differing one the other because of their density: low-density and high-density liquid.

Scientists are manifesting a spread interest in polyamorphism, *i.e.*, the occurrence of different amorphous forms of the same substance. In particular, while we have information on the distinct structures of vHDA, HDA and LDA, *i.e.*, their hydrogen-bonded O-O distances and the number of interstitial non-hydrogen bonded water molecules, resulting in significantly different bulk densities, their dynamical behaviour remains to be explained. For example, it is not entirely

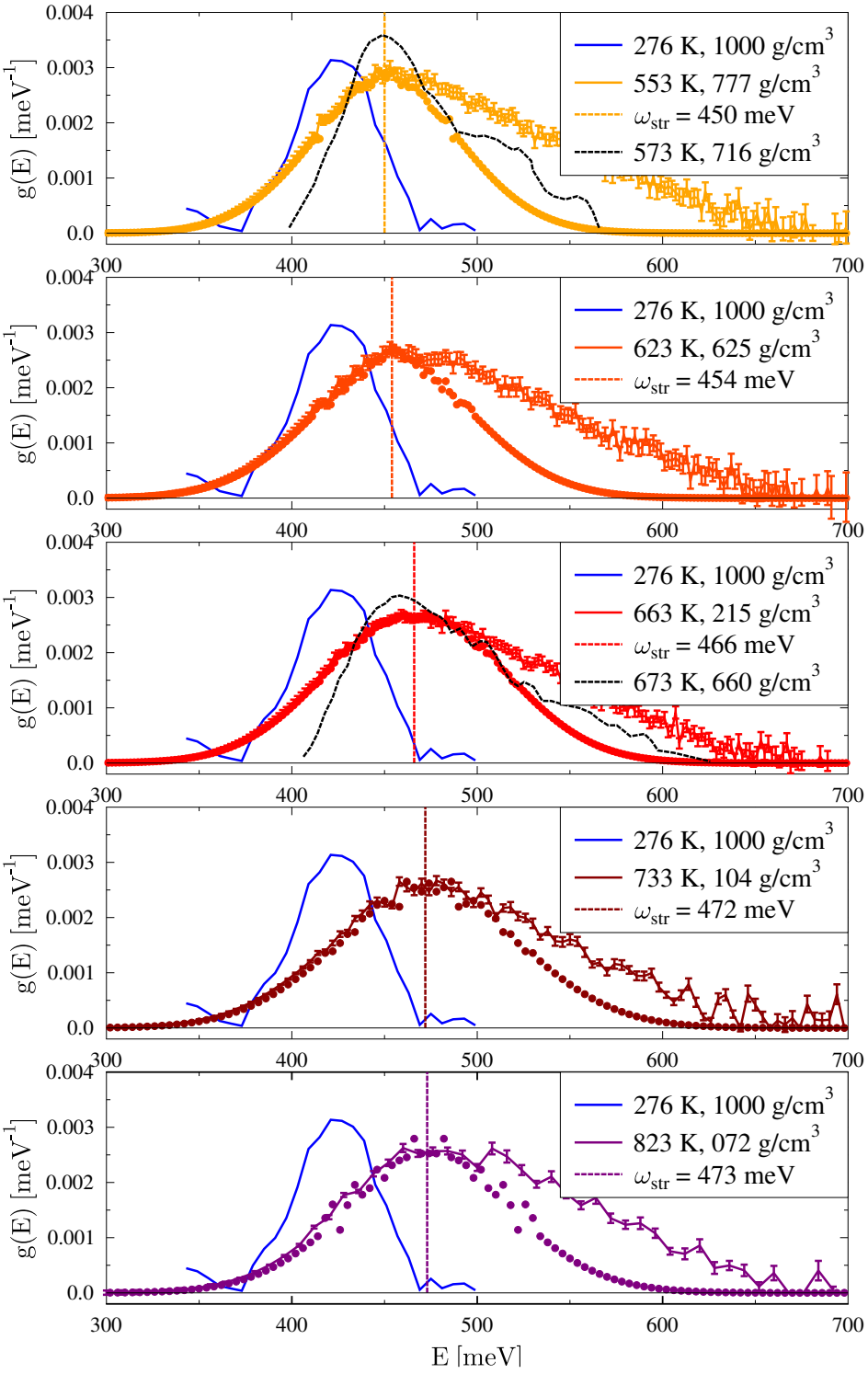

Figure 7.4: Stretching density $g_{str}(E)$ for the experimental data of the present experiment at T = 553 K , 623 K, 663 K, 733 K, 823 K. The data are presented together with the symmetrized line-shape (full circles) and its central frequency (dashed line). In all the panels, a comparison is taken with the room temperature water (blue line). In addition, data at 573 K and 673 K from Ref. [73] are reported as black lines in the first and third panels respectively.

clear if HDA and vHDA are indeed distinct states or perhaps members of the same energetic basin and phase.

7.2.1 Data analysis

The experiment was performed on the MARI spectrometer at ISIS. The vHDA, HDA and LDA were all the time at the temperature of 80 K, so that differences only due to the phase could be studied. The usually cylindrical container more suited for the MARI detector geometry was substituted with a flat-geometry container more suited for the small amount of sample of about 5 g. The initial energies were chosen as 600 meV in order to study internal vibrations and rotations, and 50 meV to allow the measurement of translational motions. An example of the experimental data is given in Figure 7.5 for LDA.

The measured cell contribution was subtracted on the measured $S(\mathbf{q},\omega)$ through the same MANTID routines used for the SEQUOIA data. In the top panel of Figure 7.6 no MS raising contribution can be seen as compared to the case of the SCW in Figure 7.2.

In the other panels of Figure 7.6, in order to maximize the signal-background ratio, an integration of $S(q,\omega)$ over the range of q where the stretching, bending, rotational or translational signal was higher, then defining the contributions

$$S(\omega)_{\text{stretching}} = \int_{9.0\mathring{A}^{-1}}^{15\mathring{A}^{-1}} S(q,\omega)\, dq, \tag{7.9}$$

$$S(\omega)_{\text{bending}} = \int_{6.0\mathring{A}^{-1}}^{13.2\mathring{A}^{-1}} S(q,\omega)\, dq, \tag{7.10}$$

$$S(\omega)_{\text{rotation}} = \int_{3.5\mathring{A}^{-1}}^{11\mathring{A}^{-1}} S(q,\omega)\, dq, \tag{7.11}$$

$$S(\omega)_{\text{translation}} = \int_{3.0\mathring{A}^{-1}}^{7.0\mathring{A}^{-1}} S(q,\omega)\, dq. \tag{7.12}$$

The centre of each of these contribution can be fitted through a Gaussian function and the corresponding values are listed in the Table 7.3.

7.2.2 Discussion

Looking at the Table 7.3, It is possible to see a redshift of the stretching frequency in the passage from vHDA to HDA and then to LDA. In particular, even if the difference of the stretching frequencies for vHDA and HDA is contained in the experimental error bars, a larger difference of 5 meV in the passage from HDA to LDA is established. As often happens in phase transitions, the bending frequency is not appreciably changing across the three phases and

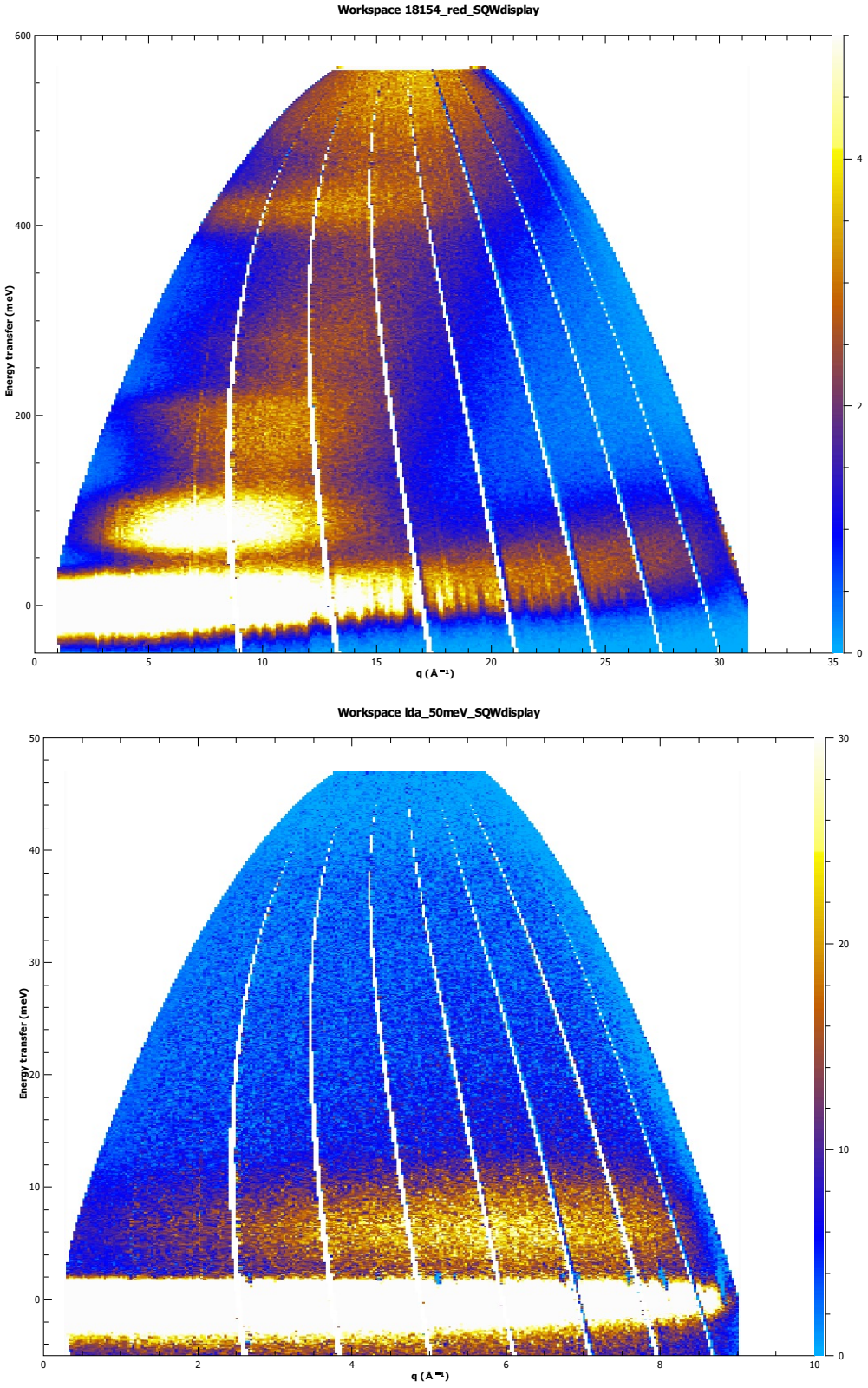

Figure 7.5: Experimental dynamic structure factor as a function of q and ω for LDA obtained with incident energies of 600 meV (top) and 50 meV (bottom).

Frequency	vHDA	HDA	LDA
Stretching [meV]	429 ± 2	427 ± 2	421 ± 2
Bending [meV]	207 ± 2	207 ± 2	206 ± 2
Libration [meV]	73.7 ± 1	74.5 ± 1	78.0 ± 1
Translation [meV]	9 ± 0.2	8 ± 0.2	6 ± 0.2
Kinetic energy	Vhda	Hda	Lda
$\langle \mathcal{E}_K \rangle_x$ [meV]	17.8 ± 0.5	17.9 ± 0.5	18.8 ± 0.5
$\langle \mathcal{E}_K \rangle_y$ [meV]	33.0 ± 0.5	33.1 ± 0.5	33.4 ± 0.5
$\langle \mathcal{E}_K \rangle_z$ [meV]	101 ± 1.0	100 ± 1.0	99.2 ± 1.0
$\langle \mathcal{E}_K \rangle$ [meV]	152 ± 2	152 ± 2	151 ± 2

Table 7.3: Harmonic model applied to INS frequencies in order to define contributions to and total kinetic energy

within the error bars. Also, a blue-shift of the rotational contribution can be appreciated from vHDA to HDA (even if in the error-bars range) and above all in the passage from HDA to LDA with a measured difference of 4 meV. Moreover, a difference in the translational frequencies, exceeding the experimental uncertainties in the two phase transitions can be seen as a red-shift of 1 meV when going from vHDA to HDA and of 2 meV when going from HDA to LDA.

The shifts in the stretching and rotational frequencies suggest the same phenomenon: the lower the density, the stronger the importance of HBs. An explanation can be found in the presence of interstitial Hs and Os in the high-density phases. An interstitial O atom in this condition increases the distance between two HB molecules, softening the action of the bond. One could expect that the translational frequency could be another measure of the hindered motions in a HB system: the stronger the HB, the larger the deviation from a free-nucleus energy of $k_B T/2 = 3.4$ meV at T = 80 K. The higher translational energies is now found for the high-density phases, meaning that the HB is not the main reason for the hindered translations.

The present study is a perfect testing bench for the harmonic model presented in Chapter 4 since all the vibrational frequencies have been measured in the same INS experiment and they can then be used to define the fractions and kinetic energy contributions $\langle \mathcal{E}_K \rangle_\alpha$ in the case of the amorphous ices. The exact value for the HOH angle was not known, but considering the weak dependence of the force constants upon the angle (discussed in the same Chapter), a standard value for the Ih ice phase of 108 degrees has been used. The evaluated energy contributions are presented in the lower part of Table 7.3. The total $\langle \mathcal{E}_K \rangle$ can be considered

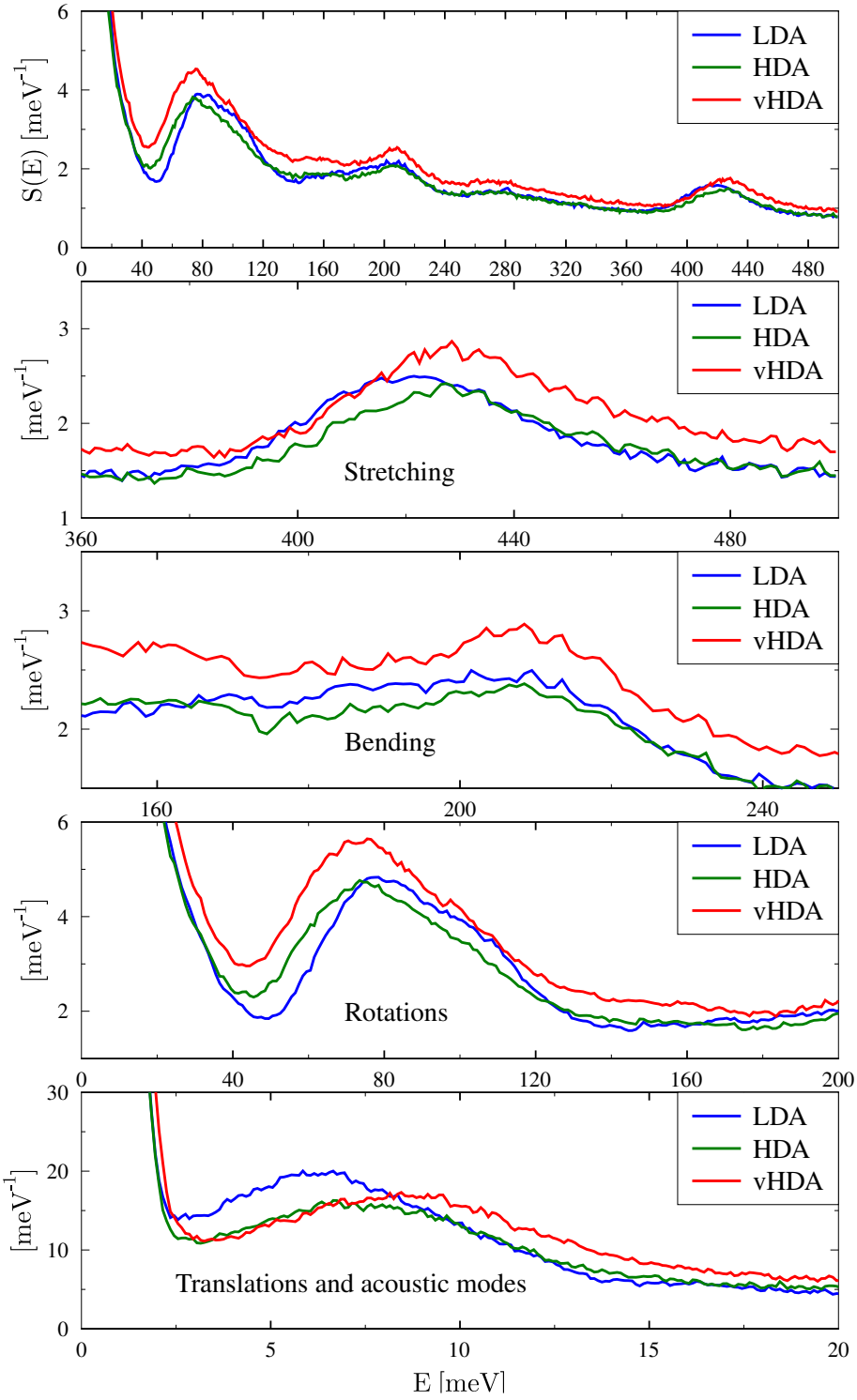

Figure 7.6: Dynamic structure factor integrated over q in the case of the three amorphous phases. In the top panel, the full q-range has been used for the integration, while in the lower panels, a q-range maximizing the signal to background ratio has been chosen in the case of stretching, bending, rotational and translational frequencies (see text).

all the same within the error bars. On the other hand, differences in the x and z components (as in the case of D in Chapter 6) can be found with opposite signs ($\Delta\langle\mathcal{E}_K\rangle_z = 1.7$ meV and $\Delta\langle\mathcal{E}_K\rangle_x = -1.0$ meV) leading to a quasi-complete cancellation. Anyway, this cancellation is not the same phenomenon that we discussed under the name of CQEs, since the reported value are not experimental quantities but the result of the first-order quantum harmonic model. The translational modes increase going from LDA to vHDA, as it is expected for acoustic modes.

A universal behaviour for glasses and amorphous solids is the existence of a boson peak [137]. This is the result of anharnmonic interactions amongst low-energy modes [138, 139]. Under critical conditions, unstable systems with separated acoustic modes collapse in stable system with one boson peak created from the rearrangement of the interacting modes. The presence of this peak manifest itself as a bump in the reduced vibrational density of states, $g(E)/E^2$. The increase in intensity for this function due to the boson peak could only be seen in comparison with a measure on a crystalline form. Unfortunately, this measure is not available.

A NCS experiment was performed, and will be presented and discussed in future publications, able to measure the actual value for the total mean kinetic energies and the CQE upon the two phase transitions here discussed.

Chapter 8

An Outlook to the Presented Work

The investigation of the phase diagram of water is a challenging activity in both experimental and theoretical research. In this work, I contributed to its investigation presenting new experimental data on the single-particle dynamics of the nuclei of this molecule.

The melting of light and heavy water discussed in Chapter 5 and 6 showed how the proton and deuteron dynamics are largely anisotropic. This feature was accessed analysing the hydrogen momentum distribution in its y-space through a multivariate Gaussian function. Moreover, the observed directional contributions derived from the anisotropic distribution were compared to the components derived from a first-order quantum harmonic model presented in Chapter 4. The model is based on the vibrations of decoupled and harmonic internal modes, rotations and translations. The comparison highlights some deviations enabling one to access the degree of anharmonicity of the studied system. Anharmonicity can manifest itself because of i) of a different definition of the symmetry modes due to a strong action of external forces, *i.e.*, the hydrogen bonds, or ii) anharmonic components in the single-particle potentials, such as cubic terms. From the discussion on the heavy water components it has been suggested that taking into account the effects of the first of these two possibilities allows a good agreement between experimental results and the predictions from the model. Joint inelastic neutron scattering and neutron Compton scattering experiments could then suggest the importance of the hydrogen-bond network on the structure of water as well as measure its effect on dynamic observables.

Moreover, the presented harmonic model can be an important tool in the study of competing quantum effects in the water phase transitions. Indeed, while the opposite red- and blue-shift of the stretching and rotational frequencies respectively is well known, experimental deviations measured through deep inelastic neutron scattering can be compared to the predictions of the first-order quantum model, shedding light on the presence and importance of higher-order

quantum contributions.

In Chapter 6, a new and innovative example of measure of kinetic energies and momentum distribution of intermediate-weight atoms such as oxygen is given. The work of analysis invested in the study of oxygen dynamics in heavy water has been repeated in the case of light water and will be soon presented in order to discuss the importance of isotopic substitution on the water-molecule dynamics. For the moment, an interesting result has been achieved measuring both the anisotropy of the oxygen momentum distribution and its strong deviation from the centre-of-mass dynamics, with an excess of about 50% of kinetic energy with respect to a classical picture of the molecule.

In the same Chapter 6, a deep joint study of the competing quantum effects in the melting of heavy water has been conducted with *ab-initio* molecular dynamics simulations. In particular, Deep inelastic neutron scattering and simulation results quantitatively agreed on the total mean kinetic energies of deuterium and qualitatively agreed on the oxygen total mean kinetic energy as well as the directional contributions in the case of both deuterium and oxygen. In particular, the simulation result for the oxygen mean kinetic energy is still a 10% lower than what the experiment observed.

In Chapter 7, inelastic neutron scattering experiments on supercritical water and amorphous ices have been discussed. In the case of supercritical water, the phase transition from liquid-like to gas-like phase across the pseudo-critical line has been discussed as temperature changed over about 400 K. The density of states for several temperatures has been obtained showing the opposite red and blue shifts for the stretching and rotational components. The phase transition manifested as a large change on the stretching frequency. Moreover, the total mean kinetic energy for hydrogen has been obtained through the harmonic model of Chapter 4 for all the measured temperatures. This is the first part of an investigation completed by a deep inelastic neutron scattering experiment conducted on supercritical water at the same pressure and temperatures, enabling a further discussion on the competing quantum effects across this phase transition.

In the same Chapter 7, the phase transitions from very high density amorphous ice to high density amorphous ice and then from high density amorphous ice to low density amorphous ice have been studied through inelastic neutron scattering accessing all the vibrational fundamentals. The red and blue shifts on the stretching and rotational components has been observed in the passage from the high-density phases to the low density phase. In addition, a non-expected red-shift for the translational frequency has been found. When all the vibrational frequencies

had been determined, the harmonic model was applied and the total mean kinetic energy and directional contributions were determined for the three phases. Within the error bars, the total kinetic energies are the same meaning that competing quantum effects occur at least as a first-order quantum cancellation. In this case, as in the case of the supercritical-water experiment, a *twin* deep inelastic neutron scattering experiment has been performed to measure the kinetic energies in the three phases and will show if and how the harmonic approximation is satisfied.

In Figure 8.1 the collection of the inelastic neutron scattering measurements on the stretching frequency presented in this work is reported as a function of temperature (upper panel) and density (lower panel). The experimental data are related to very different thermodynamic regions in the phase diagram of water: in red the values for supercritical water at different temperatures, in blue the values for the three amorphous ices and in green the values for the phase transition across melting for ice Ih at T = 271 K and liquid water at T = 285 K. As a function of density, the stretching mode reaches the *isolated molecule* value in the limit of $\rho \to 0$, *i.e.*, when the hydrogen bonds are all broken or related to large inter-molecular distances. When the density increases and up to ice, the inter-molecular distance decreases and the effect of hydrogen bonding on the stretching frequency is more and more important, causing a red-shift of the vibration. This behaviour holds till the liquid T = 285 K point. From this point, across the freezing phase transition, the reorientation of the hydrogen-bond network brings an additional red-shift of the stretching frequency even if the density is now decreased. Moreover, when the sample goes from low-density amorphous ice to the denser phases, the stretching frequencies increases. Indeed, in the denser phases the water molecules are so packed together that interstitial hydrogen atoms appear between two hydrogen-bonded molecules. The related increase in the distance of two bonded molecules is reflected in a blue-shift of the stretching vibration. Hence, while the dynamic features of the crossing of the pseudo-critical line are well observed, the changes in the passage from an amorphous ice to a denser one can be explained with changes in the structure of the sample.

In conclusion, we have used inelastic and deep inelastic neutron scattering in order study the single particle dynamics of hydrogen and oxygen in the water molecule in a variety of thermodynamic states. The work that has been presented can be thought as *self-standing* but is at present under continuous evolution and will be soon enriched with new data collected during the Ph.D period. Moreover, the intense academic training and research activity on inelastic neutron scattering gave me the possibility to work at the ISIS facility on the VESUVIO spectrometer and to develop neutron detection and-data analysis routines.

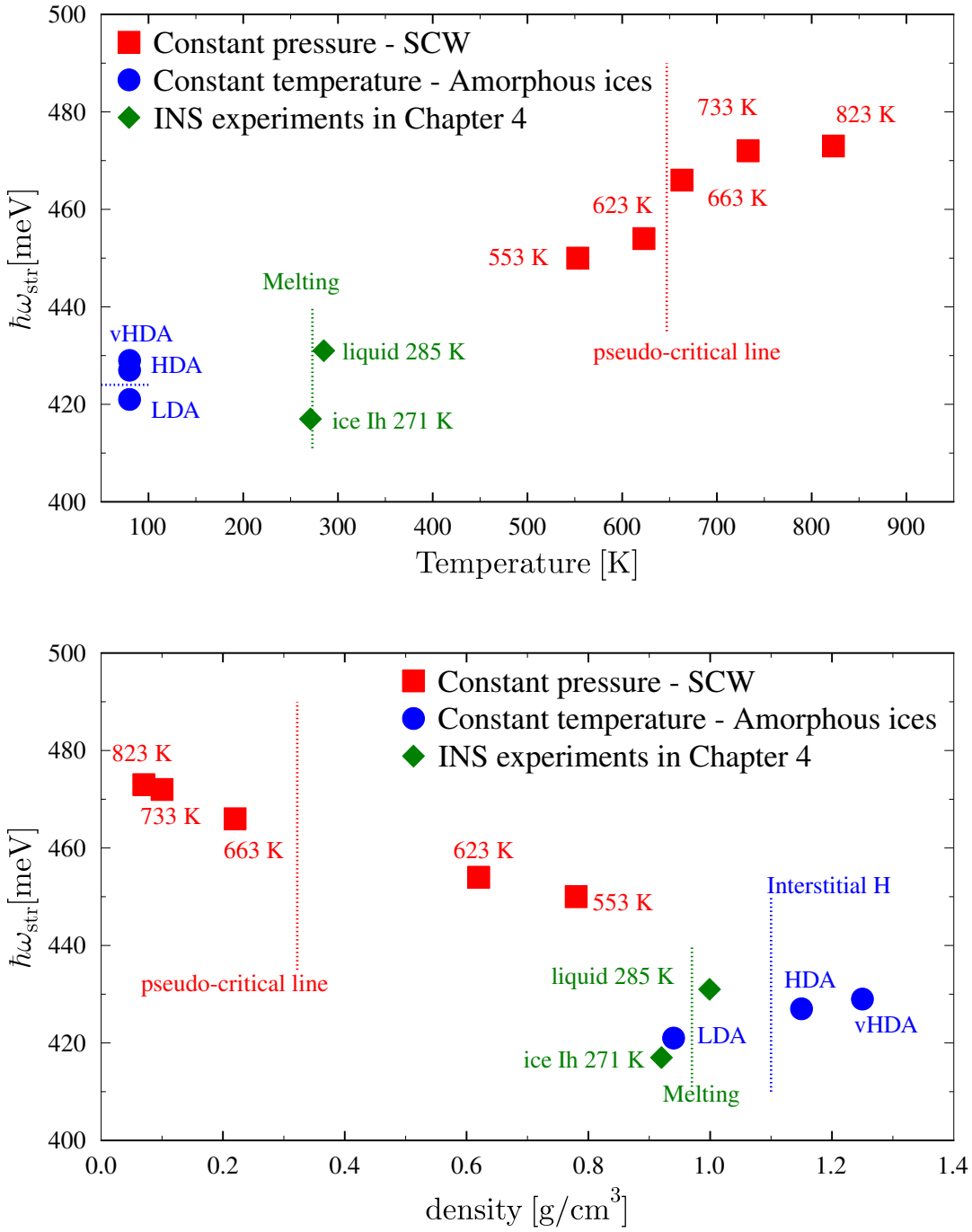

Figure 8.1: Dependence of the stretching frequency $\hbar\omega_{str}$ temperature (top) and density (bottom) as a result from the present work: SCW (red squares); LDA, HDA and vHDA ice (blue circles); liquid water at T = 285 K and ice Ih at T = 271 K (green diamonds). In addition, the pseudo-critical line is shown al a dashed red line, the melting line is shown as a green dashed line and the phase rearrangement from LDA to HDA is shown as a blue dashed line.

Omnes in philosopho continentur

The only way to reach the heart of the matter buried under the complexity of the structural and dynamical properties of the water molecule, then continuing a work started 24 centuries ago, is to build a stronger collaboration in experimental and theoretical activities. A great amount of information can be unearthed when the *right graph* is created. The first analytic Theories describing water disappeared with the advent of widespread calculation-power. Brute-force numerical simulations can suggest the path to follow but is not the final destination. There is more intuition in a slippery icosahedron than in more than a hundred computational models.

Appendix A

Constants and Acronyms

The list of the Acronyms appearing in this work

- CQE → Competing Quantum Effects
- D → Deuterium
- DD → Double Difference
- DINS → Deep Inelastic Neutron Scattering
- d.o.f. → degree of freedom
- FC → Foil cycling
- FSE → Final State Effects
- H → Hydrogen
- HB → Hydrogen Bond
- HDA → High-Density Amorphous
- IA → Impulse Approximation
- LDA → Low-Density Amorphous
- INS → Inelastic Neutron Scattering
- MS → Multiple Scattering
- MSD → Mean-square Displacement

- NCP → Neutron Compton Profile
- NCS → Neutron Compton Scattering
- NQE → Nuclear Quantum Effects
- O → Oxygen
- PIMD → Path Integral Molecular Dynamics
- SCW → Supercritical Water
- TAG → Transient Anisotropic Gaussian
- t.o.f. → time of flight
- vHDA → very-High-Density Amorphous
- ZPE → Zero Point Energy

The value of $\hbar$

The value of used in this work is $\hbar = 2.0445$ (meV-a.m.u.)$^{\frac{1}{2}}$/Å^{-1}.

Appendix B

Proof of Eq. 3.53

A multivariate Gaussian distribution function is the result of a harmonic single-particle spatial potential of the form

$$V(x,y,z) = \frac{1}{2}M\omega_x^2 x^2 + \frac{1}{2}M\omega_y^2 y^2 + \frac{1}{2}M\omega_z^2 z^2. \tag{B.1}$$

As specified in the main text, no coupling amongst the three harmonic oscillation is considered, and the multivariate distribution presents no crossed terms. When the Laplace operator on this potential is considered, the result is

$$\nabla^2 V(x,y,x) = \omega_x^2 + \omega_y^2 + \omega_z^2. \tag{B.2}$$

According to Equation 3.36, the first coefficient for the FSE correction can be expressed in this case as

$$A_3 = \frac{M}{36\hbar^2 q}\nabla^2 V(x,y,x) = \frac{M^2\left(\omega_x^2 + \omega_y^2 + \omega_z^2\right)}{36\hbar^2 q}. \tag{B.3}$$

Moreover, we can impose that the mean kinetic energy in each direction, $\langle E_K\rangle_\alpha$, can be expressed in the two forms

$$\frac{1}{4}\hbar\omega_\alpha = \langle E_K\rangle_\alpha = \frac{\hbar^2\sigma_\alpha^2}{2M} \tag{B.4}$$

leading to the relation between the fitted standard deviation σ_α and the curvature of the potential ω_α,

$$\omega_\alpha = \frac{2\hbar\sigma_\alpha^2}{M} \tag{B.5}$$

that will bring to the final result for the coefficient

$$A_3 = \frac{M^2}{36\hbar^2 q}\frac{4\hbar^2\left(\sigma_x^4 + \sigma_y^4 + \sigma_z^4\right)}{M^2} = \frac{\sigma_x^4 + \sigma_y^4 + \sigma_z^4}{9q} \tag{B.6}$$

The remaining part of the FSE correction term concerns the derivative

$$-\frac{d^3}{dy^3}J(y) = -\frac{1}{\sqrt{2\pi}\sigma_x\sigma_y\sigma_z}\int d\Omega \frac{d^3}{dy^3}S^2 \exp\left(-\frac{y^2}{2S^2}\right) \tag{B.7}$$

where we are shortening the notation $S^2(\theta\phi) = S^2$. We have

$$\frac{d}{dy}S^2 \exp\left(-\frac{y^2}{2S^2}\right) = -y \exp\left(-\frac{y^2}{2S^2}\right) \tag{B.8}$$

then

$$\frac{d^2}{dy^2}S^2 \exp\left(-\frac{y^2}{2S^2}\right) = \frac{d}{dy}\left[-y \exp\left(-\frac{y^2}{2S^2}\right)\right] = \left(\frac{y^2}{S^2} - 1\right)\exp\left(-\frac{y^2}{2S^2}\right) \tag{B.9}$$

and finally

$$\frac{d^3}{dy^3}S^2 \exp\left(-\frac{y^2}{2S^2}\right) = \frac{d}{dy}\left(\frac{y^2}{S^2} - 1\right)\exp\left(-\frac{y^2}{2S^2}\right) = \left(-\frac{y^3}{S^4} + 3\frac{y}{S^2}\right)\exp\left(-\frac{y^2}{2S^2}\right). \tag{B.10}$$

Combining these two results, Equation 3.53 is obtained

$$-A_3(q)\frac{d^3}{dy^3}J(y) = \frac{\sigma_x^4 + \sigma_y^4 + \sigma_z^4}{9\sqrt{2\pi}\sigma_x\sigma_y\sigma_z q}\int_\Omega d\Omega \left[\frac{y^3}{S^2(\theta,\phi)^4} - 3\frac{y}{S^2(\theta,\phi)^2}\right]\exp\left(-\frac{y^2}{2S^2(\theta,\phi)}\right) \tag{B.11}$$

Appendix C

Proof of the link equations in Chapter 3

The conspicuous number of analytical passages that led, at the end of Chapter 3, to the link equations defining the parameters of a Gauss - Hermite expansion for the anharmonic NCP as functions of the three variances of a multivariate Gaussian NCP are here described in more detail.

In principle it is possible to define a relationship between a number n of the first even moments of each of the two line-shapes (being the odd moments zero because of the parity of the NCP). Here, we evaluate the relationships up to $n = 3$.

C.1 Moments of the anharmonic NCP

The general expression for the n even moment of a anharmonic and isotropic NCP is

$$M_{2n}[J(y)] = \int_{-\infty}^{\infty} y^{2n} \frac{\exp\left(-\frac{y^2}{2\sigma^2}\right)}{\sqrt{2\pi}\sigma} \sum_l \frac{c_{2l}}{l!2^{2l}} H_l\left(\frac{y}{\sqrt{2}\sigma}\right) dy \tag{C.1}$$

with H_l the l-th Hermite polynomial. It is useful to transform the West variable y into the expansion variable $x = y/\sqrt{2}\sigma$. The relationship between the moments for the y and x variables is

$$M_{2n}[J(y)] = \left(\sqrt{2}\sigma\right)^{2n} \int_{-\infty}^{\infty} x^{2n} \frac{\exp(-x^2)}{\sqrt{\pi}} \sum_l \frac{c_{2l}}{l!2^{2l}} H_l(x) dx = \left(\sqrt{2}\sigma\right)^{2n} M_{2n}[J(x)]. \tag{C.2}$$

The evaluation of the n-th moment goes through the sum of an (in principle infinite) number of terms, one per Hermite polynomial, and proportional to the quantity

$$a_{2n,2l} = 2^n \int_{-\infty}^{\infty} x^{2n} \frac{\exp(-x^2)}{\sqrt{\pi}} \frac{c_{2l}}{l!2^{2l}} H_l(x) dx \tag{C.3}$$

so that, when all the terms for the same n-th moment are summed up, the quantity

$$2^n M_{2n}[J(x)] = \sum_l c_{2l} a_{2n,2l} \tag{C.4}$$

is obtained. First, we note that the property

$$a_{2n,2l} = 0 \qquad \text{for } l > n \tag{C.5}$$

allows to take into account only the Hermite polynomials of degree lower or equal to the order of the considered moment, in practice avoiding a sum of an infinite number of terms. Also, the useful relation

$$a_{2n,2n} = a_{2n,0} = (2n-1)!! \tag{C.6}$$

guarantees some hope when some large and strange coefficients appear at the end of long calculations. Indeed, for a NCP defined up to the degree $2l = 10$ in the Hermite polynomials, the values of the coefficients $a_{2n,2l}$ in matrix form are

$$a_{2n,2l} = \begin{pmatrix} 1 & 0 & 0 & 0 & 0 & 0 \\ 3 & 0 & 3 & 0 & 0 & 0 \\ 15 & 0 & 45 & 15 & 0 & 0 \\ 105 & 0 & 630 & 420 & 105 & 0 \\ 945 & 0 & 9450 & 9450 & 4725 & 945 \end{pmatrix}. \tag{C.7}$$

In the matrix notation each column corresponds to an Hermite polynomial starting from $2l = 0$ up to $2l = 10$.

The n-th moment of the anharmonic NCP is expressed as

$$M_{2n}[J(y)] = \left(\sqrt{2}\sigma\right)^{2n} M_{2n}[J(x)] = \sigma^{2n} \sum_{l=0}^{n} c_{2l} a_{2n,2l} \tag{C.8}$$

and some values are

$$M_2[J(y)] = \sigma^2 \tag{C.9}$$

$$M_4[J(y)] = 3\,(1 + c_4)\,\sigma^4 \tag{C.10}$$

$$M_6[J(y)] = 5!!\,(1 + 3c_4 + c_6)\,\sigma^6 \tag{C.11}$$

$$M_8[J(y)] = 7!!\,(1 + 6c_4 + 4c_6 + c_8)\,\sigma^8 \tag{C.12}$$

$$M_{10}[J(y)] = 9!!\,(1 + 10c_4 + 10c_6 + 5c_8 + c_{10})\,\sigma^{10}. \tag{C.13}$$

C.2 Moments of the multivariate $J(y)$

We now want to evaluate the corresponding moments for the multivariate Gaussian NCP, namely

$$M_{2n}[J(y)] = \aleph \int_0^{\frac{\pi}{2}} d\phi \int_0^1 dt \int_{-\infty}^{\infty} dy\, y^{2n} \exp\left(-\frac{y^2}{2S^2(t,\phi)}\right) S^2(t,\phi) \tag{C.14}$$

with the normalization constant $\aleph = 2/(\sqrt{(2\pi)}\pi\sigma_x\sigma_y\sigma_z)$ and the generalized standard deviation

$$\frac{1}{S^2(t,\phi)} = (1-t^2)\left(\frac{\cos\phi^2}{\sigma_x^2} + \frac{\sin\phi^2}{\sigma_y^2}\right) + \frac{t^2}{\sigma_z^2} \tag{C.15}$$

with $t = \cos\theta$. Of the three integration, it is useful to start with that in y. This integration has the general result

$$\int_{-\infty}^{\infty} dy\, y^{2n} \exp\left(-\frac{y^2}{2S^2(t,\phi)}\right) S^2(t,\phi) = (2n-1)!!S^2(t,\phi)^{\frac{2n+3}{2}}. \tag{C.16}$$

The apparently complicated integration in t can be simplified writing

$$\frac{1}{S^2(t,\phi)} = (1-t^2)\left(\frac{\cos\phi^2}{\sigma_x^2} + \frac{\sin\phi^2}{\sigma_y^2}\right) + \frac{t^2}{\sigma_z^2} = \Phi + \left(\frac{1}{\sigma_z^2} - \Phi\right) t^2 = a + bt^2 \tag{C.17}$$

through the definitions $\Phi = \cos\phi^2/\sigma_x^2 + \sin\phi^2/\sigma_y^2$, $a = \Phi$ and $b = 1/\sigma_z^2 - \Phi$ We now proceed considering the three moments one-at-the-time. For the first one, of order $n = 1$, one has

$$\int_0^1 dt\,(a+bt^2)^{-\frac{5}{2}} = \frac{3a+2b}{3a^2(a+b)^{\frac{3}{2}}} = \frac{a+2(a+b)}{3a^2\sigma_z^{-\frac{3}{2}}} \tag{C.18}$$

$$= \frac{\sigma_z}{3}\frac{\Phi + \frac{2}{\sigma_z^2}}{\Phi^2} = \frac{\sigma_z}{3}\frac{\sigma_z^2\Phi + 2}{\Phi^2} \tag{C.19}$$

after the integration in t, and subsequently integrated in ϕ giving

$$\frac{\sigma_z}{3}\int_0^{\frac{\pi}{2}} \frac{\sigma_z^2\Phi + 2}{\Phi^2} d\phi = \frac{\pi}{2}\sigma_x\sigma_y\sigma_z\frac{\left(\sigma_x^2+\sigma_y^2+\sigma_z^2\right)}{3} \tag{C.20}$$

We note that the integration in ϕ can be solved through the transformation $\tan\phi \to z$. Where the first factors cancel the normalization factors and the result for the second moment, $n = 1$, is

$$M_2\left[J(y)\right] = \frac{\left(\sigma_x^2+\sigma_y^2+\sigma_z^2\right)}{3} = \bar{\sigma}^2 \tag{C.21}$$

with $\bar{\sigma}^2$ the mean square standard deviation.

For the moment of order $n = 2$ one has

$$3\int_0^1 dt\,(a+bt^2)^{-\frac{7}{2}} = 3\frac{15a^2+20ab+8b^2}{15a^3(a+b)^{\frac{5}{2}}} = \frac{\sigma_z^5}{5}\frac{15a(a+b)+5b(a+b)+3b^2}{a^3} = \tag{C.22}$$

$$= \frac{\sigma_z}{5}\frac{15\Phi\sigma_z^2+5(1-\sigma_z^2\Phi)+3(1-\sigma_z\Phi)^2}{\Phi^3} = \frac{\sigma_z}{5}\frac{3\sigma_z^4\Phi^2+4\sigma_z^2\Phi+8}{\Phi^3} \tag{C.23}$$

that can be integrated in ϕ

$$\frac{\sigma_z}{5}\int_0^{\frac{\pi}{2}} \frac{3\sigma_z^4\Phi^2+4\sigma_z^2\Phi+8}{\Phi^3}d\phi = \frac{\pi}{2}\sigma_x\sigma_y\sigma_z\frac{\left(3\sigma_x^2+3\sigma_y^2+3\sigma_z^2+2\sigma_x\sigma_y+2\sigma_x\sigma_z+2\sigma_y\sigma_z\right)}{5} \tag{C.24}$$

$$= \frac{\pi}{2}\sigma_x\sigma_y\sigma_z\frac{\left(2(\sigma_x^2+\sigma_y^2+\sigma_z^2)+(\sigma_x+\sigma_y+\sigma_z)^2\right)}{5} = \frac{\pi}{2}\sigma_x\sigma_y\sigma_z\frac{2\bar{\sigma}^4}{5}\left(\frac{\sigma_x^4+\sigma_y^4+\sigma_z 4}{\bar{\sigma}^4}+\frac{9}{2}\right) \tag{C.25}$$

giving as a final result

$$M_4\left[J(y)\right] = \frac{2\bar{\sigma}^4}{5}\left(\frac{\sigma_x^2+\sigma_y^2+\sigma_z^2}{\bar{\sigma}^4}+\frac{9}{2}\right) \tag{C.26}$$

Finally, the last of the three moments we are concerned with, with $n = 3$, is expressed as

$$15\int_0^1 dt\,(a+bt^2)^{-\frac{9}{2}} = 15\frac{35a^3+70a^2b+56ab^2+16b^3}{35a^4(a+b)^{\frac{7}{2}}} \tag{C.27}$$

$$= \frac{3\sigma_z^7}{7}\frac{35a(a+b)^2+16b^2(a+b)+5ab^2}{a^4} = \frac{3\sigma_z}{7}\frac{5\Phi^3\sigma_z^6+6\Phi^2\sigma_z^4+8\Phi\sigma_z^2+16}{\Phi^4} \tag{C.28}$$

and integrated in ϕ

$$\frac{3\sigma_z}{7}\int_0^{\frac{\pi}{2}} \frac{5\Phi^3\sigma_z^6+6\Phi^2\sigma_z^4+8\Phi\sigma_z^2+16}{\Phi^4}d\phi = \tag{C.29}$$

$$\frac{\pi}{2}\sigma_x\sigma_y\sigma_z\frac{3\left(5(\sigma_x^3+\sigma_y^3+\sigma_z^3)+3(\sigma_x^2\sigma_y+\sigma_x^2\sigma_z+\sigma_x\sigma_y^2+\sigma_x\sigma_z^2+\sigma_y^2\sigma_z+\sigma_y\sigma_z^2)+2\sigma_x^2\sigma_y^2\sigma_z^2\right)}{7} = \tag{C.30}$$

$$= \frac{\pi}{2}\sigma_x\sigma_y\sigma_z\frac{12\bar{\sigma}^6}{7}\left(\frac{\sigma_x^6+\sigma_y^6+\sigma_z^6-\sigma_x^2\sigma_y^2\sigma_z^2}{\bar{\sigma}^6}+\frac{27}{4}\right) \tag{C.31}$$

gives as a final result

$$M_6\left[J(y)\right] = \frac{12\bar{\sigma}^6}{7}\left(\frac{\sigma_x^6+\sigma_y^6+\sigma_z^6-\sigma_x^2\sigma_y^2\sigma_z^2}{\bar{\sigma}^6}+\frac{27}{4}\right) \tag{C.32}$$

C.3 Link

The link definitions are then obtained imposing the equality of the moments of the two line-shapes for $n = 1, 2, 3$.

The first one has the simple interpretation discussed in the main text,

$$\sigma^2 = \frac{\left(\sigma_x^2 + \sigma_y^2 + \sigma_z^2\right)}{3} = \bar{\sigma}^2. \tag{C.33}$$

The second one

$$3\left(1 + c_4\right)\sigma^4 = \frac{2\bar{\sigma}^4}{5}\left(\frac{\sigma_x^2 + \sigma_y^2 + \sigma_z^2}{\bar{\sigma}^4} + \frac{9}{2}\right) \tag{C.34}$$

defines the parameter c_4 as proportional to the kurtosis of the multivariate Gaussian

$$c_4 = \frac{2}{15}\left(\frac{\sigma_x^2 + \sigma_y^2 + \sigma_z^2}{\bar{\sigma}^4} + \frac{9}{2}\right) - 1 = \frac{2}{15}\left(\frac{\sigma_x^2 + \sigma_y^2 + \sigma_z^2}{\bar{\sigma}^4} - 3\right) \tag{C.35}$$

and finally the third Hermite coefficient can be defined from

$$5!!\left(1 + 3c_4 + c_6\right)\sigma^6 = \frac{12\bar{\sigma}^6}{7}\left(\frac{\sigma_x^6 + \sigma_y^6 + \sigma_z^6 - \sigma_x^2\sigma_y^2\sigma_z^2}{\bar{\sigma}^6} + \frac{27}{4}\right) \tag{C.36}$$

giving as a result

$$\begin{aligned} c_6 = \frac{4}{35}\left(\frac{\sigma_x^6 + \sigma_y^6 + \sigma_z^6 - \sigma_x^2\sigma_y^2\sigma_z^2}{\bar{\sigma}^6} + \frac{27}{4}\right) - 1 - 3c_4 \\ = \frac{4}{35}\left(\frac{\sigma_x^6 + \sigma_y^6 + \sigma_z^6 - \sigma_x^2\sigma_y^2\sigma_z^2}{\bar{\sigma}^6} - 2\right) - 3c_4 \end{aligned} \tag{C.37}$$

Bibliography

[1] P. Ball, "Water: Water - an enduring mystery," Nature, vol. 452, no. 7185, pp. 291–292, 2008.

[2] B. Widom, "Intermolecular forces and the nature of the liquid state: Liquids reflect in their bulk properties the attractions and repulsions of their constituent molecules," Science, vol. 157, no. 3787, pp. 375–382, 1967.

[3] H. Yu and W. F. van Gunsteren, "Charge-on-spring polarizable water models revisited: From water clusters to liquid water to ice," The Journal of Chemical Physics, vol. 121, no. 19, pp. 9549–9564, 2004.

[4] J. K. Gregory, D. C. Clary, K. Liu, M. G. Brown, and R. J. Saykally, "The water dipole moment in water clusters," Science, vol. 275, no. 5301, pp. 814–817, 1997.

[5] J. Lennard-Jones and J. A. Pople, "Molecular association in liquids. i. molecular association due to lone-pair electrons," Proceedings of the Royal Society of London A: Mathematical, Physical and Engineering Sciences, vol. 205, no. 1081, pp. 155–162, 1951.

[6] L. C. Allen, "Water. a comprehensive treatise. felix franks, ed. plenum, new york, 1973," Science, vol. 184, no. 4133, p. 152, 1974.

[7] B. Chen, I. Ivanov, M. L. Klein, and M. Parrinello, "Hydrogen bonding in water," Phys. Rev. Lett., vol. 91, p. 215503, Nov 2003.

[8] X.-Z. Li, B. Walker, and A. Michaelides, "Quantum nature of the hydrogen bond," Proceedings of the National Academy of Sciences, 2011.

[9] Y. Marechal, The Hydrogen Bond and the Water Molecule: The Physics and Chemistry of Water, Aqueous and Bio-Media. Elsevier Science, 2006.

[10] M. Chaplin, "Water structure and science," http://www1.lsbu.ac.uk/water/, 2014.

[11] J. A. Morrone, L. Lin, and R. Car, "Tunneling and delocalization effects in hydrogen bonded systems: A study in position and momentum space," jcp, vol. 130, p. 204511, May 2009.

[12] S. E. Pagnotta, F. Bruni, R. Senesi, and A. Pietropaolo, "Quantum Behavior of Water Protons in Protein Hydration Shell," Biophys J, vol. 96, pp. 1939–1943, Mar. 2009.

[13] G. F. Reiter, J. Mayers, and P. Platzman, "Direct Observation of Tunneling in KDP using Neutron Compton Scattering," Physical Review Letters, vol. 89, p. 135505, Sept. 2002.

[14] L. Lin, J. A. Morrone, R. Car, and M. Parrinello, "Displaced path integral formulation for the momentum distribution of quantum particles," Phys Rev Lett, vol. 105, p. 110602, Sep 2010.

[15] T. E. Markland and B. Berne, "Unraveling quantum mechanical effects in water using isotopic fractionation," Proceedings of the National Academy of Sciences, vol. 109, no. 21, pp. 7988–7991, 2012.

[16] B. Pamuk, J. M. Soler, R. Ramirez, C. P. Herrero, P. W. Stephens, P. B. Allen, and M.-V. Fernandez-Serra, "Anomalous nuclear quantum effects in ice," Physical Review Letters, vol. 108, p. 193003, May 2012.

[17] R. Senesi, D. Flammini, A. I. Kolesnikov, Éamonn D. Murray, G. Galli, and C. Andreani, "The quantum nature of the oh stretching mode in ice and water probed by neutron scattering experiments," The Journal of Chemical Physics, vol. 139, no. 7, p. 074504, 2013.

[18] G. Reiter, C. Burnham, D. Homouz, P. M. Platzman, J. Mayers, T. Abdul-Redah, A. P. Moravsky, J. C. Li, C.-K. Loong, and A. I. Kolesnikov, "Anomalous Behavior of Proton Zero Point Motion in Water Confined in Carbon Nanotubes," Phys Rev Lett, vol. 97, pp. 247801–+, Dec. 2006.

[19] J. Kohanoff, W. Andreoni, and M. Parrinello, "Zero-point-motion effects on the structure of C60," Phys. Rev. B, vol. 46, pp. 4371–4373, Aug. 1992.

[20] R. Senesi, G. Romanelli, M. Adams, and C. Andreani, "Temperature dependence of the zero point kinetic energy in ice and water above room temperature," Chemical Physics, vol. 427, pp. 111–116, 2013.

[21] P. Larkin, Infrared and Raman Spectroscopy. Elsevier, 2011.

[22] G. Herzberg, Molecular spectra and molecular structure. Vol.2: Infrared and Raman spectra of polyaton 1945.

[23] G. P. Johari, A. Hallbrucker, and E. Mayer, "Isotope effect on the glass transition and crystallization of hyperquenched glassy water," The Journal of Chemical Physics, vol. 92, no. 11, pp. 6742–6746, 1990.

[24] C. Gainaru, A. L. Agapov, V. Fuentes-Landete, K. Amann-Winkel, H. Nelson, K. W. Kster, A. I. Kolesnikov, V. N. Novikov, R. Richert, R. Bhmer, T. Loerting, and A. P. Sokolov, "Anomalously large isotope effect in the glass transition of water," Proceedings of the National Academy of Sciences, vol. 111, no. 49, pp. 17402–17407, 2014.

[25] A. Botti, F. Bruni, A. Isopo, M. A. Ricci, and A. K. Soper, "Experimental determination of the site-site radial distribution functions of supercooled ultrapure bulk water," The Journal of Chemical Physics, vol. 117, pp. 6196–6199, Oct. 2002.

[26] A. Soper, "Structural transformations in amorphous ice and supercooled water and their relevance to the phase diagram of water," Mol Phys, vol. 106, no. 16-18, pp. 2053–2076, 2008.

[27] A. Pietropaolo, R. Senesi, C. Andreani, and J. Mayers, "Quantum Effects in Water: Proton Kinetic Energy Maxima in Stable and Supercooled Liquid," Brazilian Journal of Physics, vol. 39, pp. 318–321, June 2009.

[28] B. Mason, "The supercooling and nucleation of water," Advances in Physics, vol. 7, no. 26, pp. 221–234, 1958.

[29] J. A. Sellberg, C. Huang, T. A. McQueen, N. D. Loh, H. Laksmono, D. Schlesinger, R. G. Sierra, D. Nordlund, C. Y. Hampton, D. Starodub, D. P. Deponte, M. Beye, C. Chen, A. V. Martin, A. Barty, K. T. Wikfeldt, T. M. Weiss, C. Caronna, J. Feldkamp, L. B. Skinner, M. M. Seibert, M. Messerschmidt, G. J. Williams, S. Boutet, L. G. M. Pettersson, M. J. Bogan, and A. Nilsson, "Ultrafast X-ray probing of water structure below the homogeneous ice nucleation temperature," Nature, vol. 510, pp. 381–384, June 2014.

[30] R. M. Brugger, A. D. Taylor, C. E. Olsen, J. A. Goldstone, and A. K. Soper, "A spectrometer for inelastic scattering using neutrons from 1 ev to 186 ev," Nuclear Instruments and Methods in Physics Research, vol. 221, no. 2, pp. 393 – 407, 1984.

[31] G. E. Granroth, A. I. Kolesnikov, T. E. Sherline, J. P. Clancy, K. A. Ross, J. P. C. Ruff, B. D. Gaulin, and S. E. Nagler, "SEQUOIA: A Newly Operating Chopper Spectrometer at the SNS," Journal of Physics Conference Series, vol. 251, p. 012058, Nov. 2010.

[32] H. Compton, "A quantum theory of the scattering of X-rays by light elements," Physical Review, vol. 21, pp. 483–502, May 1932.

[33] B. G. Williams, "Compton scattering : the investigation of electron momentum distributions. New York : McGraw-Hill International, 1977.

[34] V. I. Gol'danskii Soviet Phys. JETP, vol. 4, p. 604, 1957.

[35] G. K. Ivanov and Y. S. Sayasov, "Reviews of Topical Problems: Interaction of Neutrons with Molecules," Soviet Physics Uspekhi, vol. 9, pp. 670–691, May 1967.

[36] G. K. Ivanov and Y. S. Sayasov, "Theory of the Vibrational Excitation of a Molecule in the Impulse Approximation," Soviet Physics Doklady, vol. 9, pp. 171–+, Aug. 1964.

[37] P. C. Hohenberg and P. M. Platzman, "High-Energy Neutron Scattering from Liquid He^4," Physical Review, vol. 152, pp. 198–200, Dec. 1966.

[38] R. N. Silver, "Theory of neutron scattering experiments on momentum distributions in quantum fluids," Continuum Mechanics and Thermodynamics, 1987.

[39] R. Senesi, C. Andreani, D. Colognesi, A. Cunsolo, and M. Nardone, "Deep-Inelastic Neutron Scattering Determination of the Single-Particle Kinetic Energy in Solid and Liquid ^{3}He," Phys Rev Lett, vol. 86, pp. 4584–4587, May 2001.

[40] C. Andreani, D. Colognesi, J. Mayers, G. F. Reiter, and R. Senesi, "Measurement of momentum distribution of lightatoms and molecules in condensed matter systems using inelastic neutron scattering," Advances in Physics, vol. 54, no. 5, pp. 377–469, 2005.

[41] R. Senesi, A. Pietropaolo, A. Bocedi, S. E. Pagnotta, and F. Bruni, "Proton Momentum Distribution in a Protein Hydration Shell," Phys Rev Lett, vol. 98, pp. 138102–+, Mar. 2007.

[42] R. N. Silver and P. E. Sokol, Momentum Distributions. Springer, 2013.

[43] G. Reiter and R. Silver, "Measurement of interionic potentials in solids using deep-inelastic neutron scattering," Phys Rev Lett, vol. 54, pp. 1047–1050, Mar 1985.

[44] V. F. Sears, "Scaling and final-state interactions in deep-inelastic neutron scattering," Phys. Rev. B, vol. 30, pp. 44–51, July 1984.

[45] G. F. Reiter, J. C. Li, J. Mayers, T. Abdul-Redah, and P. Platzman, "The Proton Momentum Distribution in Water and Ice," Brazilian Journal of Physics, vol. 34, pp. 142–147, Mar. 2004.

[46] R. Senesi, C. Andreani, Z. Bowden, D. Colognesi, E. Degiorgi, A. L. Fielding, J. Mayers, M. Nardone, J. Norris, M. Praitano, N. J. Rhodes, W. G. Stirling, J. Tomkinson, and C. Uden, "VESUVIO: a novel instrument for performing spectroscopic studies in condensed matter with eV neutrons at the ISIS facility," Physica B Condensed Matter, vol. 276, pp. 200–201, Mar. 2000.

[47] J. Mayers and G. Reiter, "The vesuvio electron volt neutron spectrometer," Meas Sci Technol, vol. 23, p. 045902, 2012.

[48] M. Tardocchi, G. Gorini, A. Pietropaolo, C. Andreani, R. Senesi, N. Rhodes, and E. M. Schooneveld, "YAP scintillators for resonant detection of epithermal neutrons at pulsed neutron sources," Rev Sci Instrum, vol. 75, pp. 4880–4890, Nov. 2004.

[49] A. Pietropaolo, C. Andreani, A. Filabozzi, E. Pace, and R. Senesi, "Resolution function in deep inelastic neutron scattering using the Foil Cycling Technique," Nucl. Instrum. Methods Phys. Res. A, vol. 570, pp. 498–510, Jan. 2007.

[50] E. M. Schooneveld, J. Mayers, N. J. Rhodes, A. Pietropaolo, C. Andreani, R. Senesi, G. Gorini, E. Perelli-Cippo, and M. Tardocchi, "Foil cycling technique for the VESUVIO spectrometer operating in the resonance detector configuration," Rev. Sci. Inst., vol. 77, pp. 5103–+, Sept. 2006.

[51] C. Andreani, D. Colognesi, E. Degiorgi, A. Filabozzi, M. Nardone, E. Pace, A. Pietropaolo, and R. Senesi, "Double difference method in deep inelastic neutron scattering on the VESUVIO spectrometer," Nucl. Instrum. Methods Phys. Res. A, vol. 497, pp. 535–549, Feb. 2003.

[52] R. Moreh and D. Nemirovsky, "On the proton kinetic energy in H_2O and in nanotube water," Journal of Chemical Physics, vol. 133, p. 084506, Aug. 2010.

[53] Y. Finkelstein and R. Moreh, "Temperature dependence of the proton kinetic energy in water between 5 and 673 K," Chemical Physics, vol. 431, pp. 58–63, Mar. 2014.

[54] J. Mayers and G. Reiter, "The vesuvio electron volt neutron spectrometer," Meas Sci Technol, vol. 23, p. 045902, 2012.

[55] J. A. Morrone and R. Car, "Nuclear quantum effects in water," Phys Rev Lett, vol. 101, p. 017801, Jul 2008.

[56] J. A. Morrone, L. Lin, and R. Car, "Tunneling and delocalization effects in hydrogen bonded systems: A study in position and momentum space," The Journal of Chemical Physics, vol. 130, pp. 204511–+, May 2009.

[57] C. Andreani, D. Colognesi, E. Degiorgi, and M. A. Ricci, "Proton dynamics in supercritical water," J Chem Phys, vol. 115, pp. 11243–11248, Dec. 2001.

[58] A. Pietropaolo, R. Senesi, C. Andreani, A. Botti, M. A. Ricci, and F. Bruni, "Excess of Proton Mean Kinetic Energy in Supercooled Water," Phys Rev Lett, vol. 100, pp. 127802–+, Mar. 2008.

[59] A. Pietropaolo, R. Senesi, C. Andreani, A. Botti, M. A. Ricci, and F. Bruni, "Pietropaolo et al Reply:," Phys Rev Lett, vol. 103, pp. 069802–+, Aug. 2009.

[60] C. Andreani, D. Colognesi, A. Pietropaolo, and R. Senesi, "Ground state proton dynamics in stable phases of water," Chem Phys Lett, vol. 518, no. 0, pp. 1 – 6, 2011.

[61] D. Colognesi, C. Andreani, and E. Degiorgi, "Phonon density of states from a crystal-analyzer inverse-geometry spectrometer: A study on ordered solid hydrogen sulfide and hydrogen chloride," Journal of Neutron Research, vol. 11, no. 3, pp. 123–143, 2003.

[62] M. Ceriotti, G. Bussi, and M. Parrinello, "Nuclear quantum effects in solids using a colored-noise thermostat," Phys Rev Lett, vol. 103, p. 030603, Jul 2009.

[63] D. Flammini, A. Pietropaolo, R. Senesi, C. Andreani, F. McBride, A. Hodgson, M. A. Adams, L. Lin, and R. Car, "Spherical momentum distribution of the protons in hexagonal ice from modeling of inelastic neutron scattering data ," J Chem Phys, vol. 136, pp. 024504–+, 2012.

[64] L. Lin, J. A. Morrone, R. Car, and M. Parrinello, "Momentum distribution, vibrational dynamics, and the potential of mean force in ice," Phys. Rev. B, vol. 83, p. 220302, Jun 2011.

[65] C. Pantalei, A. Pietropaolo, R. Senesi, S. Imberti, C. Andreani, J. Mayers, C. Burnham, and G. Reiter, "Proton Momentum Distribution of Liquid Water from Room Temperature to the Supercritical Phase," Phys Rev Lett, vol. 100, pp. 177801–+, May 2008.

[66] M. Ceriotti and D. E. Manolopoulos, "Efficient first-principles calculation of the quantum kinetic energy and momentum distribution of nuclei," Phys Rev Lett, vol. 109, p. 100604, Sep 2012.

[67] M. Ceriotti, G. Miceli, A. Pietropaolo, D. Colognesi, A. Nale, M. Catti, M. Bernasconi, and M. Parrinello, "Nuclear quantum effects in ab initio dynamics: Theory and experiments for lithium imide," Phys. Rev. B, vol. 82, p. 174306, Nov 2010.

[68] C. Andreani, P. Bosi, F. Sacchetti, and C. K. Loong, "Absolute measurements of the stretching mode density of states in polycrystalline ice Ih," J Chem Phys, vol. 83, pp. 750–753, July 1985.

[69] C. Andreani, V. Merlo, and M. A. Ricci, "A procedure for multiple scattering corrections in a neutron incoherent inelastic scattering experiment," Nuclear Instruments and Methods in Physics Research B, vol. 36, pp. 216–221, Feb. 1989.

[70] C. Andreani, V. Merlo, M. A. Ricci, and B. C. Boland, "Vibrational density of states in polycrystalline sulphuric acid," Mol Phys, vol. 66, pp. 747–755, 1989.

[71] C. Andreani, E. Degiorgi, R. Senesi, F. Cilloco, D. Colognesi, J. Mayers, M. Nardone, and E. Pace, "Single particle dynamics in fluid and solid hydrogen sulphide: An inelastic neutron scattering study," J Chem Phys, vol. 114, pp. 387–398, Jan. 2001.

[72] R. Moreh and D. Nemirovsky, "On the proton kinetic energy in H_2O and in nanotube water," J Chem Phys, vol. 133, pp. 084506–+, Aug. 2010.

[73] M. A. Ricci, M. Nardone, A. Fontana, C. Andreani, and W. Hahn, "Light and neutron scattering studies of the OH stretching band in liquid and supercritical water," The Journal of Chemical Physics, vol. 108, pp. 450–454, Jan. 1998.

[74] C. Vega, M. M. Conde, C. McBride, J. L. F. Abascal, E. G. Noya, R. Ramirez, and L. M. Ses, "Heat capacity of water: A signature of nuclear quantum effects," The Journal of Chemical Physics, vol. 132, no. 4, pp. –, 2010.

[75] S. Habershon, T. E. Markland, and D. E. Manolopoulos, "Competing quantum effects in the dynamics of a flexible water model.," J. Chem. Phys., vol. 131, no. 2, p. 24501, 2009.

[76] X. Z. Li, B. Walker, and A. Michaelides, "Quantum nature of the hydrogen bond," Proc. Natl. Acad. Sci. USA, vol. 108, no. 16, p. 6369, 2011.

[77] T. E. Markland and B. J. Berne, "Unraveling quantum mechanical effects in water using isotopic fractionation," Proc. Natl. Acad. Sci. USA, vol. 109, no. 21, pp. 7988–7991, 2012.

[78] J. Liu, R. S. Andino, C. M. Miller, X. Chen, D. M. Wilkins, M. Ceriotti, and D. E. Manolopoulos, "A Surface-Specific Isotope Effect in Mixtures of Light and Heavy Water," J. Phys. Chem. C, vol. 117, pp. 2944–2951, Feb. 2013.

[79] R. H. McKenzie, "A diabatic state model for donor-hydrogen vibrational frequency shifts in hydrogen bonded complexes," Chem. Phys. Lett., vol. 535, pp. 196–200, May 2012.

[80] R. Ramirez and C. P. Herrero, "Kinetic energy of protons in ice ih and water: A path integral study," Phys. Rev. B, vol. 84, p. 064130, Aug 2011.

[81] J. Vaníček and W. H. Miller, "Efficient estimators for quantum instanton evaluation of the kinetic isotope effects: Application to the intramolecular hydrogen transfer in pentadiene," The Journal of Chemical Physics, vol. 127, p. 114309, Sept. 2007.

[82] F. Paesani and G. A. Voth, "The properties of water: Insights from quantum simulations," The Journal of Physical Chemistry B, vol. 113, no. 17, pp. 5702–5719, 2009. PMID: 19385690.

[83] R. Ramírez and C. P. Herrero, "Quantum path integral simulation of isotope effects in the melting temperature of ice Ih.," J. Chem. Phys., vol. 133, p. 144511, Oct. 2010.

[84] M. Ceriotti and T. E. Markland, "Efficient methods and practical guidelines for simulating isotope effects.," J. Chem. Phys., vol. 138, p. 014112, Jan. 2013.

[85] M. Ceriotti, G. Bussi, and M. Parrinello, "Nuclear quantum effects in solids using a colored-noise thermostat," Phys. Rev. Lett., vol. 103, no. 3, p. 30603, 2009.

[86] L. Lin, J. A. Morrone, R. Car, and M. Parrinello, "Displaced Path Integral Formulation for the Momentum Distribution of Quantum Particles," Phys. Rev. Lett., vol. 105, no. 11, p. 110602, 2010.

[87] M. Ceriotti, D. E. Manolopoulos, and M. Parrinello, "Accelerating the convergence of path integral dynamics with a generalized Langevin equation.," J. Chem. Phys., vol. 134, no. 8, p. 84104, 2011.

[88] M. Ceriotti and D. E. Manolopoulos, "Efficient First-Principles Calculation of the Quantum Kinetic Energy and Momentum Distribution of Nuclei," Phys. Rev. Lett., vol. 109, p. 100604, 2012.

[89] J. A. Morrone and R. Car, "Nuclear Quantum Effects in Water," Phys. Rev. Lett., vol. 101, no. 1, p. 17801, 2008.

[90] M. Ceriotti, G. Miceli, A. Pietropaolo, D. Colognesi, A. Nale, M. Catti, M. Bernasconi, and M. Parrinello, "Nuclear quantum effects in ab initio dynamics: Theory and experiments for lithium imide," Phys. Rev. B, vol. 82, no. 17, p. 174306, 2010.

[91] G. Reiter, J. C. Li, J. Mayers, T. Abdul-Redah, and P. Platzman, "The proton momentum distribution in water and ice," Braz. J. Phys., vol. 34, pp. 142–147, 2004.

[92] A. Pietropaolo, R. Senesi, C. Andreani, A. Botti, M. A. Ricci, and F. Bruni, "Excess of Proton Mean Kinetic Energy in Supercooled Water," Physical Review Letters, vol. 100, p. 127802, Mar. 2008.

[93] R. Senesi, C. Andreani, D. Colognesi, A. Cunsolo, and M. Nardone, "Deep-inelastic neutron scattering determination of the single-particle kinetic energy in solid and liquid," Phys Rev Lett, vol. 86, pp. 4584–4587, May 2001.

[94] G. F. Reiter, R. Senesi, and J. Mayers, "Changes in the Zero-Point Energy of the Protons as the Source of the Binding Energy of Water to A-Phase DNA," Phys Rev Lett, vol. 105, pp. 148101–+, Oct. 2010.

[95] M. Krzystyniak and F. Fernandez-Alonso, "Ab initio nuclear momentum distributions in lithium hydride: Assessing nonadiabatic effects," Phys. Rev. B, vol. 83, no. 13, p. 134305, 2011.

[96] A. G. Seel, M. Ceriotti, P. P. Edwards, and J. Mayers, "Simultaneous measurement of lithium and fluorine momentum in 7LiF.," J. Phys. Cond. Matt., vol. 24, p. 365401, Sept. 2012.

[97] L. Lin, J. A. Morrone, R. Car, and M. Parrinello, "Momentum distribution, vibrational dynamics, and the potential of mean force in ice," Phys. Rev. B, vol. 83, no. 22, p. 220302, 2011.

[98] C. P. Herrero and R. Ramirez, "Isotope effects in ice Ih: A path-integral simulation," The Journal of Chemical Physics, vol. 134, p. 094510, Mar. 2011.

[99] A. G. Seel, A. Sartbaeva, J. Mayers, A. J. Ramirez-Cuesta, and P. P. Edwards, "Neutron compton scattering investigation of sodium hydride: From bulk material to encapsulated nanoparticulates in amorphous silica gel," The Journal of Chemical Physics, vol. 134, no. 11, pp. –, 2011.

[100] A. K. Soper and C. J. Benmore, "Quantum differences between heavy and light water," Phys. Rev. Lett., vol. 101, p. 065502, Aug 2008.

[101] J. Mayers, "Calculation of background effects on the VESUVIO eV neutron spectrometer," Meas Sci Technol, vol. 22, pp. 015903–+, Jan. 2011.

[102] C. Lee, W. Yang, and R. G. Parr, "Development of the Colle-Salvetti correlation-energy formula into a functional of the electron density," Phys. Rev. B, vol. 37, no. 2, p. 785, 1988.

[103] A. D. Becke, "Density-functional exchange-energy approximation with correct asymptotic behavior," Phys. Rev. A, vol. 38, no. 6, p. 3098, 1988.

[104] S. Goedecker, M. Teter, and J. Hutter, "Separable dual-space Gaussian pseudopotentials," Phys. Rev. B, vol. 54, no. 3, pp. 1703–1710, 1996.

[105] J. VandeVondele, M. Krack, F. Mohamed, M. Parrinello, T. Chassaing, and J. Hutter, "Quickstep: Fast and accurate density functional calculations using a mixed Gaussian and plane waves approach," Comp. Phys. Comm., vol. 167, pp. 103–128, Apr. 2005.

[106] R. P. Feynman and A. R. Hibbs, Quantum Mechanics and Path Integrals. New York: McGraw-Hill, 1964.

[107] D. M. Ceperley, "Path integrals in the theory of condensed helium," Rev. Mod. Phys., vol. 67, no. 2, pp. 279–355, 1995.

[108] S. Grimme, J. Antony, S. Ehrlich, and H. Krieg, "A consistent and accurate ab initio parametrization of density functional dispersion correction (DFT-D) for the 94 elements H-Pu.," J. Chem. Phys., vol. 132, p. 154104, Apr. 2010.

[109] "GLE4MD." http://gle4md.berlios.de.

[110] A. Giuliani, F. Bruni, M. A. Ricci, and M. A. Adams, "Isotope quantum effects on the water proton mean kinetic energy," Phys. Rev. Lett., vol. 106, p. 255502, Jun 2011.

[111] D. Eisenberg and W. Kauzmann, The Structure and Properties of Water. Oxford (UK): Oxford University Press, 1968.

[112] J.-J. Max and C. Chapados, "Isotope effects in liquid water by infrared spectroscopy," The Journal of Chemical Physics, vol. 116, no. 11, pp. 4626–4642, 2002.

[113] J. E. Bertie and E. Whalley, "Infrared spectra of ices ih and ic in the range 4000 to 350 cm1," The Journal of Chemical Physics, vol. 40, no. 6, pp. 1637–1645, 1964.

[114] M. J. Taylor and E. Whalley, "Raman spectra of ices ih, ic, ii, iii, and v," The Journal of Chemical Physics, vol. 40, no. 6, pp. 1660–1664, 1964.

[115] G. S. Fanourgakis and S. S. Xantheas, "The bend angle of water in ice ih and liquid water: The significance of implementing the nonlinear monomer dipole moment surface in classical interaction potentials," The Journal of Chemical Physics, vol. 124, no. 17, pp. –, 2006.

[116] R. E. Shawyer and P. Dean, "Atomic vibrations in orientationally disordered systems. ii. hexagonal ice," Journal of Physics C: Solid State Physics, vol. 5, no. 10, p. 1028, 1972.

[117] G. Romanelli, M. Ceriotti, D. E. Manolopoulos, C. Pantalei, R. Senesi, and C. Andreani, "Direct measurement of competing quantum effects on the kinetic energy of heavy water upon melting," The Journal of Physical Chemistry Letters, vol. 4, no. 19, pp. 3251–3256, 2013.

[118] C. Andreani, G. Romanelli, and R. Senesi, "A combined INS and DINS study of proton quantum dynamics of ice and water across the triple point and in the supercritical phase," Chemical Physics, vol. 427, pp. 106–110, Dec. 2013.

[119] C. A. Eckert, "Supercritical fluids as solvents for chemical and materials processing," Nature, vol. 383, pp. 313–318, Sept. 1996.

[120] M. J. Cocero, E. Alonso, R. Toro, D. Vallelado, T. Sanz, and F. Fdz-Polanco, "Supercritical water oxidation (scwo) for poly(ethylene terephthalate) (pet) industry effluents," Industrial & Engineering Chemistry Research, vol. 39, no. 12, pp. 4652–4657, 2000.

[121] Y. Calzavara, C. Joussot-Dubien, G. Boissonnet, and S. Sarrade, "Evaluation of biomass gasification in supercritical water process for hydrogen production," Energy Conversion and Management, vol. 46, no. 4, pp. 615 – 631, 2005.

[122] I. L. Pioro, M. Khan, V. Hopps, C. Jacobs, R. Patkunam, S. Gopaul, and K. Bakan, "SCW Pressure-Channel Nuclear Reactor Some Design Features," Journal of Power and Energy Systems, vol. 2, pp. 874–888, 2008.

[123] P. Gallo, D. Corradini, and M. Rovere, "Widom line and dynamical crossovers as routes to understand supercritical water," Nature Communications, vol. 5, p. 5806, Dec. 2014.

[124] Y. E. Gorbaty and A. G. Kalinichev, "Hydrogen bonding in supercritical water. 1. experimental results," The Journal of Physical Chemistry, vol. 99, no. 15, pp. 5336–5340, 1995.

[125] N. Matubayasi, C. Wakai, and M. Nakahara, "Nmr study of water structure in super- and subcritical conditions," Phys. Rev. Lett., vol. 78, pp. 2573–2576, Mar 1997.

[126] O. Arnold, J. Bilheux, J. Borreguero, A. Buts, S. Campbell, L. Chapon, M. Doucet, N. Draper, R. F. Leal, M. Gigg, V. Lynch, A. Markvardsen, D. Mikkelson, R. Mikkelson, R. Miller, K. Palmen, P. Parker, G. Passos, T. Perring, P. Peterson, S. Ren, M. Reuter, A. Savici, J. Taylor, R. Taylor, R. Tolchenov, W. Zhou, and J. Zikovsky, "Mantid data analysis and visualization package for neutron scattering and μ sr experiments," Nuclear Instruments and Methods in Physics Research Section A: Accelerators, Spectrometers, Detectors and Associated Equipment, vol. 764, no. 0, pp. 156 – 166, 2014.

[127] V. Sears, "Slow-neutron multiple scattering," Advances in Physics, vol. 24, no. 1, pp. 1–45, 1975.

[128] E. K. Bigg, "The supercooling of water," Proceedings of the National Physical Society B, vol. 66, no. 688, 1953.

[129] R. C. Miller, R. J. Anderson, J. L. Kassner, and D. E. Hagen, "Homogeneous nucleation rate measurements for water over a wide range of temperature and nucleation rate," The Journal of Chemical Physics, vol. 78, no. 6, pp. 3204–3211, 1983.

[130] C. A. Tulk, C. J. Benmore, J. Urquidi, D. D. Klug, J. Neuefeind, B. Tomberli, and P. A. Egelstaff, "Structural studies of several distinct metastable forms of amorphous ice," Science, vol. 297, no. 5585, pp. 1320–1323, 2002.

[131] P. G. Debenedetti, "TOPICAL REVIEW: Supercooled and glassy water," Journal of Physics Condensed Matter, vol. 15, p. 1669, Nov. 2003.

[132] O. Mishima, L. D. Calvert, and E. Whalley, "'Melting ice' I at 77 K and 10 kbar: a new method of making amorphous solids," Nature, vol. 310, pp. 393–395, Aug. 1984.

[133] O. Mishima, L. D. Calvert, and E. Whalley, "An apparently first-order transition between two amorphous phases of ice induced by pressure," Nature, vol. 314, pp. 76–78, Mar. 1985.

[134] O. Mishima and Y. Suzuki, "Propagation of the polyamorphic transition of ice and the liquid-liquid critical point," Nature, vol. 419, pp. 599–603, Oct. 2002.

[135] C. U. Kim, B. Barstow, M. W. Tate, and S. M. Gruner, "Evidence for liquid water during the high-density to low-density amorphous ice transition," Proceedings of the National Academy of Sciences, vol. 106, no. 12, pp. 4596–4600, 2009.

[136] P. H. Poole, F. Sciortino, U. Essmann, and H. E. Stanley, "Phase behaviour of metastable water," Nature, vol. 360, no. 6402, pp. 324–328, 1992.

[137] H. Shintani and H. Tanaka, "Universal link between the boson peak and transverse phonons in glass," Nature Materials, vol. 7, pp. 870–877, Nov. 2008.

[138] H. Cang, J. Li, H. C. Andersen, and M. D. Fayer, "Boson peak in supercooled liquids: Time domain observations and mode coupling theory," The Journal of Chemical Physics, vol. 123, p. 064508, Aug. 2005.

[139] N. Xu, M. Wyart, A. J. Liu, and S. R. Nagel, "Excess vibrational modes and the boson peak in model glasses," Phys. Rev. Lett., vol. 98, p. 175502, Apr 2007.